DISSERTATION

THE ROLE OF PLASMA-SURFACE INTERACTIONS IN PROCESS CHEMISTRY: MECHANISTIC STUDIES OF a-CN_x DEPOSITION AND SF_6/O_2 ETCHING OF SILICON

Submitted by

Joshua M. Stillahn

Department of Chemistry

In partial fulfillment of the requirements

For the Degree of Doctor of Philosophy

Colorado State University

Fort Collins, Colorado

Fall 2010

Doctoral Committee:

Department Chair: Ellen R. Fisher

Advisor: Ellen R. Fisher

Elliot R. Bernstein
David S. Dandy
Nancy E. Levinger
Amy L. Prieto

ABSTRACT OF DISSERTATION

THE ROLE OF PLASMA-SURFACE INTERACTIONS IN PROCESS CHEMISTRY: MECHANISTIC STUDIES OF a-CN_x DEPOSITION AND SF_6/O_2 ETCHING OF SILICON

The molecular level chemistry of a-CN_x deposition in plasma discharges was studied with emphasis on the use of CH_3CN and BrCN as single source precursors for these films. Characterization of the global deposition behavior in these systems indicates that the resulting films are relatively smooth and contain significant levels of N-content, with N/C > 0.3. Notably, films obtained from BrCN plasmas are observed to delaminate upon their exposure to atmosphere, and preliminary investigation of this behavior is presented.

Detailed chemical investigation of the deposition process focuses primarily on the contributions of CN radicals, which were characterized from their origin in the gas phase to their reaction at the a-CN_x film surface. Laser-induced fluorescence studies suggest that CN is formed through electron impact dissociation of the precursor species and that this breakdown process produces CN with high internal energies, having rotational and vibrational temperatures on the order of 1000 K and 5000 K, respectively. Measurement of CN surface reactivity coefficients in CH_3CN plasmas show that CN reacts with a

probability of ~94%, irrespective of the deposition conditions; this information, combined with gas phase and film characterization data, leads to the conclusion that CN internal energies exert a strong influence on their surface reactivity and that these surface reactions favor their incorporation into the a-CN_x film. Moreover, this correlation is shown to hold for several other plasma radicals studied in our lab, suggesting the potential for developing a general model for predicting surface interactions of activated gas phase species.

This dissertation also presents results from studies of SF_6/O_2 etching of Si. Addition of O_2 to the feed gas leads to the generation of SO_2, among other species, and gas phase characterization data suggest that SO_2 may act as a sink for atomic S, preventing the reformation of SO_xF_y ($y > 0$) and thus promoting generation of atomic F. The surface scatter coefficient of SO_2 was also measured in an effort to understand its role in the formation of gas phase species. These measurements suggest that SO_2 does not undergo surface reaction during etching and therefore does not contribute to the generation of gaseous SO_xF_y species.

Joshua Michael Stillahn
Department of Chemistry
Colorado State University
Fort Collins, CO 80523
Fall 2010

TABLE OF CONTENTS

ABSTRACT OF DISSERTATION ii

TABLE OF CONTENTS iv

LIST OF FIGURES vii

LIST OF TABLES ix

CHAPTER 1. Introduction 1

1.1 Plasma Chemistry 2

1.2 Plasma-Enhanced CVD 4

1.3 Plasma Etching 6

1.4 Overview of Research 9

1.5 References 12

CHAPTER 2. Experimental Methods 14

2.1 Substrate Processing and Characterization 15

2.2 Gas Phase Diagnostics 20

2.3 Surface Reactivity 29

2.4 References 32

CHAPTER 3. Plasma Diagnostics for Unraveling Process Chemistry 33

3.1 Introduction 34

3.2 Diagnostic Techniques 36

3.3 Chemistry of Specific Systems 46

3.4 Global Remarks on Plasma-Surface Interactions 63

3.5 References 66

CHAPTER 4. CN Surface Interactions and Temperature-Dependent Film Growth During Plasma Deposition of a-CN_x:H Films 71

4.1 Introduction 72

4.2 Results 74

4.3 Discussion 89

4.4 Summary 97

4.5 References 98

CHAPTER 5. Ion Bombardment Energies in CH_3CN Plasmas: Influence on a-CN_x:H Film Deposition 100

5.1 Introduction 101

5.2 Results 102

5.3 Discussion 114

5.4 Summary 119

5.5 References 120

CHAPTER 6. Gas Phase Energetics of CN Radicals in RF Discharges: Influence on Surface Reaction Probability During Deposition of Carbon Nitride Films 122

6.1 Introduction 123

6.2 Results 125

6.3 Discussion 136

6.4 Summary 145

6.5 References 147

CHAPTER 7. Deposition of a-CN_x Materials in Plasmas Containing BrCN: Exploring Adhesion Behavior as an Indicator of Film Properties 149

7.1 Introduction 150

7.2 Results and Discussion 151

7.4 Summary and Future Work 165

7.5 References 169

CHAPTER 8. Surface Interactions of SO_2 and Passivation Chemistry During Etching of Si and SiO_2 in SF_6/O_2 Plasmas 171

8.1 Introduction 172

8.2 Results 174

8.3 Discussion 190

8.4 Summary 197

8.5 References 198

CHAPTER 9. Research Summary and Perspectives 200

9.1 Research Summary 201

9.2 Future Work 204

9.3 References 206

APPENDIX A. Modeling and Analysis of Spectroscopic Ellipsometry Data 207

APPENDIX B. Correction of IRIS Data for Rotational Temperature Effects 209

LIST OF FIGURES

FIGURE	PAGE
2.1 Inductively coupled reactor schematic	16
2.2 Capacitively coupled reactor schematic	18
2.3 Mass spectrometer schematic	22
2.4 IRIS apparatus schematic	24
2.5 Long-range CN LIF excitation spectrum	26
2.6 Assembly of apparatus for heated substrate IRIS measurements	31
3.1 Schematic of neutral- and ion-surface interactions	51
4.1 OES spectrum from 100% CH_3CN plasma	75
4.2 CN band head ($\nu = 0$) LIF excitation spectrum for Θ_R measurement	76
4.3 Power, pressure, and %Ar dependence of Θ_R(CN) in CH_3CN plasma	78
4.4 Power and pressure dependence of CN LIF intensity in CH_3CN plasma	80
4.5 CN LIF images for measurement of surface reactivity	81
4.6 Experimental and simulated CN LIF cross-sections	83
4.7 Power, pressure, and %Ar dependence of *R*(CN)	84
4.8 Effect of substrate heating on film growth rate	86
4.9 AFM images of films deposited at T_S = 23°C and 100°C	88
4.10 FTIR absorption spectrum for film deposited in 100% CH_3CN plasma	90
5.1 Mass spectrum collected in 100% CH_3CN plasma	103
5.2 Power-dependent breakdown of selected ions	105
5.3 Power and pressure dependence of average ion energies	107
5.4 Pressure-dependent changes in IEDs (m/z = 15, 42)	109
5.5 Power-dependent changes in IEDs (m/z = 15, 42)	111
5.6 AFM images of films deposited with substrate bias of 0 V and +200 V DC	112

LIST OF FIGURES (cont'd)

FIGURE **PAGE**

6.1 Dependence of Θ_R(CN) on pressure, power, and gas composition....127

6.2 %Ar dependence of Θ_R(CN) in BrCN/Ar plasma....128

6.3 Comparison of fits to experimental CN LIF spectra (ν = 0, 1, 2)....130

6.4 Experimental and simulated CN LIF excitation spectra for measurement of Θ_V, Θ_R....133

6.5 Experimental and simulated CN OES spectra for measurement of Θ_V, Θ_R....135

7.1 SEM images of delaminated films deposited in 100% BrCN plasma....152

7.2 Phase contrast images of films deposited in 100% CH_3CN and 100% BrCN plasma....154

7.3 FTIR absorption spectra for films deposited in CH_3CN and BrCN plasmas....156

7.4 Phase contrast image of delamination "island" on film deposited in 100% BrCN plasma....158

7.5 Phase contrast images of films deposited in CH_3CN/BrCN/CH_4 plasma mixtures....160

7.6 Cross-sectional SEM image of a-CN_x film after treatment in 100% N_2 plasma....167

8.1 O_2 flow rate and power dependence of etch rates and selectivity....175

8.2 SEM images of grid-masked Si and SiO_2 after etching....177

8.3 SEM images of surface morphology on etched Si and SiO_2....178

8.4 XPS analysis of surface composition as a function of O_2 flow rate....181

8.5 O_2 flow rate and power dependence of O* and F* actinometric OES signals....182

8.6 Mass spectra in SF_6 plasma with and without addition of O_2....184

8.7 SO_2 LIF excitation spectrum....185

8.8 O_2 flow rate and power dependence of SO_2 LIF intensity....187

LIST OF TABLES

TABLE **PAGE**

3.1 OES emission lines for selected plasma species 37

3.2 Spectroscopic properties and surface behavior of selected plasma species 40

6.1 Fit parameters for simulation of CN LIF data 132

6.2 Correlation of energetics and surface interactions for selected plasma radicals 144

7.1 Effects of Br-content on film properties and delamination behavior 162

7.2 Effect of N_2 plasma treatment on film thickness and composition 165

8.1 Etch rate and selectivity of fluoride etchants 179

8.2 SO_2 scatter coefficients 189

CHAPTER 1

INTRODUCTION

This chapter provides an overview of selected concepts in plasma discharge chemistry along with a discussion of two applications of plasma technology: chemical vapor deposition and dry chemical etching. The utility of plasma-surface interaction studies for advancing these technologies is discussed, with special emphasis on (1) systems that deposit amorphous carbon nitride films and (2) SF_6/O_2 discharges as a means of selectively etching Si materials. The chapter is concluded with a summary of the research discussed in subsequent chapters.

1.1 Plasma Chemistry

Plasma discharges create a uniquely energetic collection of gas phase species, including ions, electrons, and reactive neutrals. Plasmas occur naturally - lightning and auroras are two examples - but they can also be created under laboratory conditions, where they become useful for a variety of commercial applications. The research in this dissertation aims to facilitate the advancement of some of these technologies by understanding the chemistry occurring in rf plasma discharges. In the types of discharges used in this research, local thermodynamic equilibrium (LTE) is not achieved; thus, the electron temperature, T_e, is up to two orders of magnitude greater than the ion temperature, T_i, and neutral gas temperature, T_g, in the plasma bulk.[1] This is favorable in many applications of plasma technology because the relatively "cold" ions and neutral species can be used to controllably promote specific types of chemical reactions.

The ignition of a plasma discharge takes place when a free electron is accelerated across an applied electric potential and collides with another species, often a molecule, such as AB. When this collision occurs inelastically, nearly all of the electron's energy is transferred to the collision partner,[1] allowing a variety of reactions to take place:

$$AB + e^- \rightarrow AB^+ + 2e^- \quad (1.1)$$

$$AB + e^- \rightarrow AB^* + e^- \quad (1.2)$$

$$AB + e^- \rightarrow A + B + e^- \quad (1.3)$$

Reactions 1.1-1.3 describe the processes of electron impact ionization, excitation, and dissociation, respectively. These processes can also take place in concert with one another, as in dissociative excitation, where one of the dissociation products is promoted to an excited state, Process 1.4:

$$AB + e^- \rightarrow A^* + B + e^- \quad (1.4)$$

Practical discharge systems involve many different reactions such as the ones shown here; thus, it can readily be seen that, even for relatively simple molecules, the breakdown chemistry that takes place in the discharge becomes very complex. Moreover, in many applications, this situation is further complicated by the use of feed gas mixtures containing larger molecules that produce an increasing number of breakdown products. Notably, Reactions 1.1-1.4 describe only gas phase plasma processes, whereas the controlled use of plasma discharges in materials science necessarily demands an understanding of their interaction with surfaces. This introduces additional variables and adds yet another level of complexity to the experimental system. A variety of diagnostic techniques become useful as we seek to understand the dynamic processes that characterize plasma discharges, and it is the directed and purposeful application of these diagnostic techniques that lead to meaningful insight into the overall plasma chemistry.

This dissertation seeks to contribute to the current mechanistic understanding of plasma-surface chemistry in two different types of discharge systems. The first set of systems generates CN radicals and promotes chemical vapor deposition (CVD) of carbon nitride materials. The second set of systems produces reactive fluorine species and promotes etching of inorganic semiconductor materials. More details on these discharge systems are given below, and descriptions of the corresponding reactor systems can be found in Chapter 2.

1.2 Plasma-Enhanced Chemical Vapor Deposition

Several approaches exist for the deposition of thin films, all of them focused on creating active or energetic species at the surface that can contribute to deposition.[2] Thus, the different approaches to CVD are distinguished primarily by the respective mechanisms for precursor activation. Two common methods are thermal CVD (TCVD) and hot filament CVD (HFCVD).[2,3] TCVD is perhaps the most basic variant of CVD in that precursors are thermally activated by simply heating the substrate. However, this method requires deposition temperatures > 500° C, which can damage some substrate materials or cause detrimental interdiffusion of layers. In addition, TCVD is often carried out at temperatures where growth is mass-transport limited; any non-uniformities in flow dynamics can therefore lead to poor film quality. Lower substrate temperatures can be used in HFCVD,[4] where precursors are activated in the gas phase by a heated filament ($T > 2000°$ C) positioned upstream from the substrate. HFCVD has found somewhat widespread use in coating applications,[5-8] but the filament itself can introduce film contaminants or become coated with materials that affect its ability to generate active species.

Plasma enhanced CVD (PECVD) offers some advantages over TCVD and HFCVD as it avoids some of the limitations of these techniques. Foremost is that PECVD allows film deposition over large areas while maintaining relatively low substrate temperatures,[2,3] making it possible to deposit on fragile materials, such as polymers. PECVD has been used to deposit a variety of materials, but, as with many CVD methods, the complex deluge of precursors and energetic species at the surface

make it ill-suited for the deposition of highly ordered materials. It is more appropriate for the deposition of amorphous materials, and silicon- and carbon-based materials have become relatively ubiquitous due to their many applications as well as the availability of gaseous precursors (e.g., SiH_4 and CH_4).

Information about plasma-surface interactions can provide valuable clues for improving control over the evolution of film properties during deposition. For example, in silicon nitride deposition systems, it has been found that the particular mixture of feed gases can dictate where important chemical bonds are formed.[9,10] In SiH_4/N_2 discharges, SiH_x and NH_x species are deposited, and Si-N bonds are formed through reactions on the surface. Conversely, in SiH_4/NH_3 systems, Si-N bonds are created in the gas phase, forming aminosilane ($SiH_x(NH_2)_y$) species that act as the primary film precursors. Studies such as this not only provide a foothold for further refinement of deposition mechanisms but may also provide valuable insight for optimizing the material's performance in practical applications.[11]

Much of this dissertation focuses on the deposition of amorphous carbon nitride (a-CN_x) materials, which have garnered substantial interest due to their mechanical,[12,13] optical,[14] and electronic properties.[15] As with many CVD materials, the microstructure and composition of a-CN_x:H films is heavily dependent on the conditions that exist during deposition. In our systems, we are able to influence the gas phase chemistry through adjustment of the applied rf power and the working pressure and composition of the feed gas. In addition, some control over surface processes is achieved through regulation of the substrate temperature and ion bombardment, both of which can influence surface reactions and changes in film microstructure.

One of the critical factors in the deposition of carbon nitride is the controlled, stoichiometric incorporation of nitrogen, and although nitrogen incorporation has been shown to alter the films' optical properties,[16] reduce mechanical stress,[17] and improve film adhesion,[18-20] most reported values of the nitrogen to carbon ratios, N/C, are < 1.[21] The majority of these values come from studies of mixed precursor PECVD systems, such as CH_4/N_2, which allow independent variation of the nitrogen content in the feed gas. These mixed precursor systems can obscure some of the important chemical mechanisms, however, as a larger variety of species are generated in the gas phase and physical processes like N_2^+ bombardment can alter the film properties.[22,23]

An alternative approach to exploring a-CN_x deposition has been adopted in this dissertation. Here, single source precursors have been employed to simplify the gas phase chemistry and facilitate more detailed investigation of the molecular level chemistry, with an emphasis on CN radicals as a possible source of the nitrogen content in a-CN_x materials.[23-25] The directed use of several diagnostic techniques in these studies allows us to augment standard film characterization data with information about CN behavior in the gas phase and at the surface of a growing a-CN_x film.

1.3 Dry Etching in Plasma Discharges

Plasma discharges can also be used in etching processes. Most notably, this is done in the microelectronics industry,[26] but the same methods apply to the fabrication of other semiconductor devices, such as micro- and nanoelectromechanical systems (MEMS and NEMS)[27,28] and microfluidic systems.[29] In each case, the intention is to remove material in a specific way to etch a two dimensional pattern down to a prescribed depth.

The desired two-dimensional geometry is created by patterning the pristine substrate with an etch-resistant polymer material. The plasma etch process is then carried out using discharge feed gases that undergo reactions to volatilize the substrate material; these volatile etch products can then be pumped out of the system.[1]

In general, the most important requirement for a successful etch process is that it be anisotropic. That is, the etch process should only proceed in the direction of the surface normal, preserving the two dimensional image of the patterned photoresist as the etch front progresses into the material. Anisotropy can be improved by using a substrate bias to promote energetic ion bombardment at the trench bottom (termed reactive ion etching[1]), but a degree of chemical anisotropy can also be achieved through the formation of an etch-resistant passivation layer on the feature sidewalls. Thus, for process optimization, the etch chemistry must satisfy multiple roles. First, the etch gases must readily react with and volatilize the material at the bottom of the etch trench. At the same time, the process must provide a means for maintaining the sidewall passivation layer to prevent etching in the lateral direction. Finally, the etch gases must leave intact the resist material to preserve the original two dimensional pattern and prevent the exposure of new substrate material. Optimization of an etch process therefore requires some knowledge of the discharge's interaction with each surface – the trench bottom, the sidewall passivation layers, and the etch resist.

Typical etch systems in the microelectronics industry utilize halogenated gases such as halocarbons (CF_4, CCl_4, CF_3Cl), inorganic halides (SF_6, NF_3), or pure etchants (F_2, Cl_2, Br_2) to promote volatilization and etching for a variety of materials. Additionally, the presence of oxidants (O_2, SO_2) or reductants (H_2) can be used to alter

the chemistry in favor of either etching or passivation.[30] Although processes are now being developed to etch a variety of alternative semiconductor materials,[31,32] Si remains an important material in the industry, and advances in plasma etching have led to methods for high-precision etching of Si-based materials. In all etch systems, some degree of non-ideality exists in process anisotropy and sidewall passivation. As industry roadmaps dictate the continued reduction of critical etch dimensions, a fundamental understanding of etch and passivation chemistry is crucial to the ongoing advancement of the technology.

Chapter 8 describes efforts to explore Si passivation chemistry during etching in SF_6/O_2 plasma discharges. These discharges have potential as an alternative to etch systems in which a short, isotropic etch step is alternated with the deposition of a passivating (often fluorocarbon) film.[33] Although these multiplexed systems yield etch structures that are essentially anisotropic, the lateral component of the isotropic etch step leads to undesirable undulations, or scalloping, in the feature sidewalls. SF_6/O_2 plasmas, on the other hand, have been found to simultaneously promote etching, through the volatilization of Si,

$$\mathrm{Si}(s) + 4\mathrm{F}(g) \rightarrow \mathrm{SiF_4}\,(g) \qquad (1.5)$$

As well as passivation of Si through the formation of an etch-resistant SiO_xF_y layer.[34] Ion bombardment and reduced substrate temperatures have been shown to play critical roles as well; more energetic bombardment at the trench bottom exposes fresh Si for etching, and cryogenic substrate temperatures improve the etch resistance of the SiO_xF_y layer, leading to enhancement of the etch anisotropy.[27,35]

Although the potential of SF_6/O_2 etch systems is fairly well-established, the chemistry responsible for the formation of the SiO_xF_y passivation layer remains unclear. Oxygen is expected to play a prominent role in sidewall oxidation to form SiO_xF_y;[34] however, as shown in Chapter 8, a number of other oxygen-containing species, such as SO_2, are also present in the gas phase. The continued development of SF_6/O_2 chemistries for Si etching requires a detailed understanding of how oxidants contribute to sidewall passivation, and we employ a number of diagnostic techniques to explore the formation and surface interactions of SO_2 in these systems.

1.4 Overview of Research

Research efforts in this dissertation focus on the study of (1) CN behavior during a-CN_x deposition and (2) SO_2 behavior during Si etching. Both represent components of a larger effort to understand the surface interactions of gas phase plasma species and their implications for commercial technologies. Such an understanding is important to the continued development and application of plasma technologies, and we approach the characterization of these systems from several different angles. Chapter 2 provides a detailed description of the techniques and methods used to extract information about the experimental systems.

Chapter 3 provides a literature review of diagnostic techniques used to characterize gas phase densities and energetics as well as plasma-surface interactions. In this context, studies from the literature are discussed for five specific cases (CF_x, SiF_x, SiH_x, CH_x, and NH_x) to illustrate the value of applying multiple diagnostic techniques to to the problem of understanding complex discharge systems.

Chapter 4 presents a study of CN radicals in CH_3CN discharges as well as its contributions to film growth. CN is found to exhibit high surface reaction probabilities under all experimental conditions, and film characterization data indicate that CN is a likely source of N-content in the deposited a-CN_x:H material.

In Chapter 5, these studies are extended to the use of mass spectrometry for additional characterization of CH_3CN plasmas. Although identification of specific gas phase ionic species is somewhat inconclusive, characterization of ion energy distributions in these systems reveals information about ion bombardment energies during deposition. Subsequent deposition studies suggest that ambient ion bombardment does not have a substantial effect on the film morphology or composition.

A detailed characterization of the internal energies of CN plasma radicals is presented in Chapter 6. Internal energies are measured quantitatively and semi-quantitatively using laser-induced fluorescence and optical emission spectroscopy. The data indicate that relatively energetic CN radicals are generated in plasma discharges containing CH_4/N_2, CH_3CN, or BrCN. Considered in the context of reactivity measurements from different discharge systems, these data support the idea that internal and kinetic energies play an important and overarching role in promoting surface reactions.

In Chapter 7, preliminary data are presented that explore the delamination of films obtained from BrCN-containing discharges. This delamination behavior is somewhat anomalous among CN-containing discharges we have studied. Consistent with data from the literature, this delamination behavior appears to scale with humidity and film thickness, but the root cause of these materials' poor adhesion properties is unclear.

Deposition studies using mixed precursor discharges highlight the possible role of Br as an electronegative component of these systems.

Although Chapter 8 is somewhat of a departure from the theme of other chapters, it extends our studies of plasma-surface interactions to another plasma system with complex gas-phase and surface chemistry. Chapter 8 focuses on the contribution of SO_2 to plasma chemistry during Si etching in SF_6/O_2 discharges. Results of gas phase diagnostics suggest that SO_2 acts as a sink for atomic S in these systems and promotes the liberation of free F. As in Chapter 7, the electronegativity of species in SF_6/O_2 plasmas is implicated as an important factor of the process chemistry. Finally, Chapter 9 presents a brief summary and conveys the potential for further extension of this research in certain areas.

1.5 References

[1]A. Grill, *Cold Plasma in Materials Fabrication: From Fundamentals to Applications* (IEEE Press, New York, 1994).

[2]D. W. Hess and D. B. Graves, in *Chemical Vapor Deposition:Principles and Applications*, edited by M. L. Hitchman and K. F. Jensen (Academic Press, San Diego, CA, 1993), p. 385.

[3]K. L. Choy, Progress in Materials Science **48,** 57 (2003).

[4]R. E. I. Schropp, ECS Transaction **25,** 3 (2009).

[5]R. E. I. Schropp, C. H. M. van der Werg, V. Verlaan, J. K. Rath, and H. Li, Thin Solid Films **517,** 3039 (2009).

[6]J.-M. Bonard, Thin Solid Films **501,** 8 (2006).

[7]R. Haubner and B. Lux, Diamond Relat. Mater. **2,** 1277 (1993).

[8]K. K. S. Lau, S. K. Murthy, H. G. Pryce Lewis, J. A. Caulfield, and K. K. Gleason, J. Fluorine Chem. **122,** 93 (2003).

[9]W. M. M. Kessels, F. J. H. Van Assche, J. Hong, D. C. Schram, and M. C. M. Van de Sanden, J. Vac. Sci. Technol., A **22,** 96 (2004).

[10]D. L. Smith, A. S. Alimonda, C.-C. Chen, S. E. Ready, and B. Wacker, J. Electrochem. Soc. **137,** 614 (1990).

[11]M. J. Williams, S. S. He, S. M. Cho, and G. Lucovsky, J. Vac. Sci. Technol., A **12,** 1072 (1994).

[12]E. Broitman, W. Macdonald, N. Hellgren, G. Radnoczi, Z. Czigany, A. Wennerberg, M. Jacobsson, and L. Hultman, Diamond Relat. Mater. **9,** 1984 (2000).

[13]E. C. Cutiongco, D. Li, and Y.-W. Chung, J. Tribol. **118,** 543 (1996).

[14]S. Metin, J. H. Kaufman, D. D. Saperstein, J. C. Scott, J. Heyman, and E. E. Haller, J. Mater. Res. **9,** 396 (1994).

[15]P. Tamiasso-Martinhon, H. Cachet, C. Debiemme-Chouvy, and C. Deslouis, Electrochim. Acta **53,** 5752 (2008).

[16]X. W. Liu, J. H. Lin, C. H. Tseng, and H. C. Shih, Mater. Chem. Phys. **72,** 258 (2001).

[17]J. Freire, F.L., Japanese Journal of Applied Physics **36,** 4886 (1997).

[18]J. Freire, F.L. and D. F. Franceschini, Thin Solid Films **293,** 236 (1997).

[19]C. Spaeth, M. Kuhn, T. Chudoba, and F. Richter, Surf. Coat. Technol. **112,** 140 (1999).

[20]M. Jelinek, W. Kulisch, M. P. Delplancke-Ogletree, J. Lancok, L. Jastrabik, D. Chvostova, C. Popov, and J. Bulir, Applied Physics A **73,** 167 (2001).

[21]S. Muhl and J. M. Mendez, Diamond and Related Materials **8,** 1809 (1999).

[22]J. Hao, W. Liu, and Q. Xue, J. Non-Cryst. Solids **353,** 136 (2007).

[23]M. Zhang, Y. Nakayama, T. Miyazaki, and M. Kume, J. Appl. Phys. **85,** 2904 (1999).

[24]S. Veprek, J. Weidmann, and F. Glatz, J. Vac. Sci. Technol., A **13,** 2914 (1995).

[25]A. A. Voevodin, J. G. Jones, J. S. Zabinski, Z. Czigany, and L. Hultman, J. Appl. Phys. **92,** 4980 (2002).

[26]R. J. Shul and S. J. Pearton, *Handbook of advanced plasma processing techniques* (Springer, Berlin ;, 2000).

[27]M. J. de Boer, G. E. Gardeniers, H. V. Jansen, E. Smulders, M.-J. Gilde, G. Roelofs, J. N. Sasserath, and M. Elwenspoek, J. MEMS **11,** 385 (2002).

[28]S. E. Lyshevski, *MEMS and NEMS: Systems, Devices, and Structures* (CRC Press, Boca Raton, Fla., 2002).

[29]W. B. J. Zimmerman, *Microfluidics: History, Theory and Applications* (Springer, Wien ;, 2006).
[30]S. M. Rossnagel, J. J. Cuomo, and W. D. Westwood, *Handbook of Plasma Processing Technology Fundamentals: Etching, Deposition, and Surface Interactions* (Noyes Publications, Park Ridge, N.J., 1990).
[31]S. Guha and V. Narayanan, Annu. Rev. Mater. Res. **39,** 181 (2009).
[32]M. Heyns and W. Tsai, MRS Bull. **34,** 485 (2009).
[33]H. Rhee, H. M. Lee, Y. M. Namkoung, C.-K. Kim, H. Chae, and Y. W. Kim, J. Vac. Sci. Technol., B **27,** 33 (2009).
[34]R. Dussart, X. Mellhaoui, T. Tillocher, P. Lefaucheux, M. Boufnichel, and P. Ranson, Microelectron. Eng. **84,** 1128 (2007).
[35]S. Tachi, K. Tsujimoto, and S. Okudaira, Appl. Phys. Lett. **52,** 616 (1988).

CHAPTER 2

EXPERIMENTAL METHODS

This chapter provides a detailed description of the instruments, experimental apparatus, reagents, and methods used to conduct research discussed elsewhere in this dissertation. Section 2.1 gives a description of the apparatus used for plasma treatment of substrate samples as well as an overview of techniques used for sample characterization. Sections 2.2 and 2.3 discuss techniques used to obtain information about gas phase species and gas-surface interactions, respectively.

2.1 Substrate Processing and Characterization

Deposition Reactor. The experimental apparatus used for film deposition is schematically illustrated in Figure 2.1 and has been described in detail previously.[1] The reactor consists of two glass tubes (50 mm i.d.) joined by an o-ring (58 mm i.d., 3.5 mm cross-section) to allow access to the interior of the reactor. The main barrel of the reactor is ~48 cm long. Feed gases enter the reactor through a 6 mm i.d. inlet stem and unreacted gases are pumped away by a two-stage rotary vane mechanical pump (2 L/s). A substrate stage consisting of coiled Nichrome wire held between two ceramic plates by thermally stable ceramic adhesive (Cotronics, 904 zirconia) was coupled through the rear of the reactor to two contacts, so that application of an electric potential leads to substrate heating. Substrate temperature was monitored with a K-type thermocouple, which contacts the bottom of the substrate stage and is also coupled through the rear of the reactor. Glass sleeves (43 mm i.d.) were inserted in the main barrel of the reactor to allow exchange of heavily deposited surfaces, and the reactor and sample stage were cleaned by an oxygen plasma prior to each deposition. Substrates (20 × 20 mm p-type Si (100) with native oxide) were placed on the heated ceramic substrate stage during deposition. The pressure in the chamber was monitored with an MKS Baratron capacitance manometer and was allowed to stabilize before initiating the discharge. For all depositions, the pressure was maintained at 100 ± 2 mTorr and the applied rf power was maintained at 50 ± 2 W. Deposition times ranged from 10 min to 40 min. Following deposition, the plasma discharge was stopped, and the flow of precursor was continued for 20 min to minimize the effect of oxidation upon exposure to atmosphere.[2]

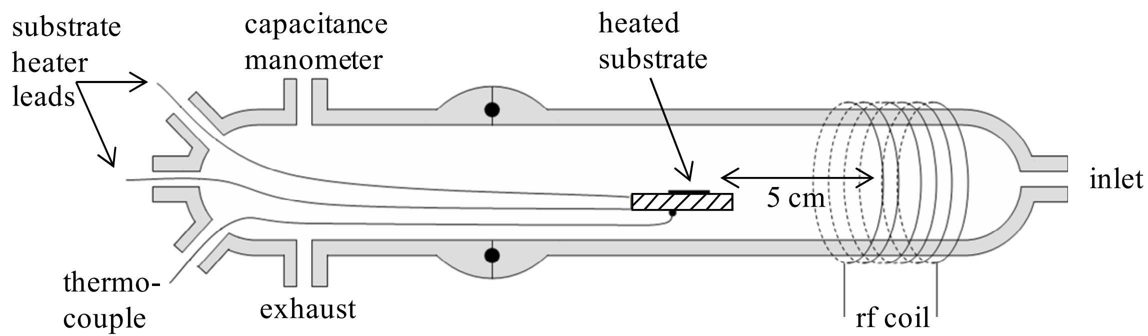

Figure 2.1 Cross-sectional schematic of the experimental apparatus used for deposition studies.

Etch Reactor. Etch rate experiments were performed in a home-built capacitively coupled plasma reactor, shown schematically in Figure 2.2 and consisting of a stainless steel 6-way cross (three intersecting tubes with i.d. = 4.5 in., 4.5 in., and 6 in.). Premixed gases enter the reactor through an inlet in the top flange, and unreacted gases are pumped away through the bottom flange with a 2-stage rotary vane mechanical pump (2 L/s). Radio frequency (13.56 MHz) rf power was applied to the lower of two aluminum electrodes (7.5 cm diameter) separated from each other by a distance of 12 mm. The pressure in the reactor was about 50 to 150 mTorr and was monitored with an MKS Baratron capacitance manometer, which is insensitive to differing gas compositions. The applied rf power, *P*, ranged from 20 to 100 W and the etch time was 3-10 min. Si and SiO_2 substrates (~15 × 15 mm) that were contact-masked with a copper TEM grid (PELCO) were placed onto the lower plate at the same time. Si substrates were scribed from p-type Si (100) wafers with a native oxide thickness of ~25 Å. SiO_2 substrates were scribed from Si wafers with >1 μm thick thermal oxide layer. All substrates were cleaned using standard RCA procedures,[3] with the Si substrates additionally dipped in concentrated HF solution for 15 sec to remove the native oxide layer.

Precursors for all studies were either obtained as high-purity gases and used as purchased or were extracted as vapors from solid or liquid precursors loaded into a Pyrex bulb. These non-gaseous precursors were purified by several freeze-pump-thaw cycles to remove dissolved atmospheric gases. All gases were introduced into the reactor through Nupro bellows-sealed metering valves, and in the case of gas mixtures, gases were

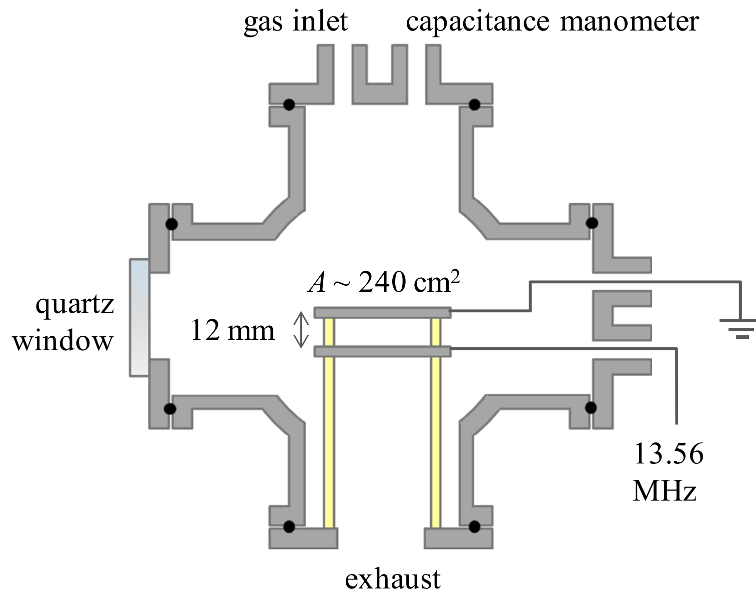

Figure 2.2 Cross-sectional schematic of the experimental apparatus used for etching studies.

premixed before entering the reactor. The total source pressure was varied from 40-150 mTorr.

Surface Characterization. Film thicknesses for films deposited in CH_3CN plasmas were measured using profilometry (Sloan Dektak IID) by masking a small section of the substrate prior to deposition and measuring the step height at an exposed edge. The thicknesses of films deposited in plasmas containing mixtures containing BrCN were measured by variable angle spectroscopic ellipsometry (VASE). VASE measurements were collected using a Woollam M-2000 model DI ellipsometer over a spectral window of 300-1100 nm with incident angles of 55°, 65°, and 75°. The resulting spectroscopic data were modeled using WVASE software provided by the instrument manufacturer to extract information about the film thickness and optical properties. For additional details on VASE analysis, see Appendix A.

Film topography was characterized using atomic force microscopy (AFM, Nanosurf Easyscan 2) in tapping mode using silicon tips (nanosensors, PPP-NCLR) with a tip radius <10 nm and tip height of 10-15 μm. Surface root-mean-square (rms) and peak-to-peak roughness values were derived from the AFM images. Topography was also characterized by scanning electron microscopy (SEM) using a JEOL JSM 6500F field emission microscope as well as by phase contrast microscopy using a Nikon phase contrast microscope.

The chemical composition of the processed surfaces was analyzed ex situ by XPS on a Physical Electronics PE 5800 ESCA/ASE system with a 2 mm monochromatic Al K_α X-ray source, hemispherical analyzer, and multichannel detector. A photoelectron take-off angle of 45° was used for all spectra. Other compositional data were obtained

from infrared spectra using a Nicolet Magna 760 Fourier-transform infrared (FTIR) spectrometer (resolution of 8 cm^{-1} and averaging over 65 scans).

2.2 Gas Phase Diagnostics

Optical Emission Spectroscopy. The inductively coupled plasma reactor used to collect optical emission spectroscopy (OES) data in PECVD studies has been described previously[1] and is very similar to the reactor used to deposition films. The reactor (50 mm diameter) was fitted with a replaceable fused quartz window at the downstream end, allowing for coaxial collection of plasma emission for maximum signal intensities. Plasma emission was imaged onto the 10 μm entrance slit of an Avantes multichannel spectrometer fitted with four optical fibers fused into one cable. The spectrometer houses four gratings yielding a ~0.15 nm resolution, four 3648-pixel charged coupled device (CCD) array detectors, and a wavelength detection range from 187 to 1016 nm. Each spectrum was collected by averaging 10 scans, each with an integration time of 10-35 ms.

In the etching studies, an Ocean Optics S2000 spectrometer fitted with optical sampling fibers was used to collect OES data over the spectral region of 248-900 nm using. Emitted light was collected through a quartz viewing window such that the sampling fibers were on axis with the discharge region between the two electrodes. Spectra were collected by averaging 10 scans, each with a 500 ms integration time. Emission signals from atomic fluorine and atomic oxygen were monitored at 703.8 and 777.3 nm, respectively. Although the atomic oxygen emission line at 844.8 has been shown to be less affected by dissociative excitation of O_2,[4] our data show that the intensities of both the 777.3 and 844.8 nm lines exhibit very similar parameter

dependence. Thus, the 777.3 nm line was used for the O density as it provided greater signal intensity. The measured O* and F* emission intensities were normalized to the 751 nm emission from Ar (General Air, 99.9%), which was deliberately added in small amounts (~2-5%) as an actinometer.

Mass Spectrometry. The apparatus used for mass spectrometry measurements is depicted in Figure 2.3 and has been described in detail elsewhere.[5] Briefly, gases enter the top of a glass reactor tube, 13.56 MHz rf power is applied to an eight-loop inductor coil, and a plasma is produced. Expansion of the plasma into a differentially pumped main chamber takes place sequentially through a ~10 mm diameter hole in the bottom of the glass reactor and through a metal grid (0.0014 in. wire diameter and 74.9 μm hole size, yielding 46% open area) attached to the inner wall of the main chamber. This creates a working pressure of ~10^{-5} Torr in the main chamber. The main chamber and metal grid were electrically grounded to confine the plasma to the reactor. Species were then sampled from the main chamber by a mass spectrometer probe (PSM3000, Hiden Analytical, Ltd.) through a 5 mm hole in an aluminum sampling cone that is 5 cm from the exit orifice on the plasma reactor. This distance is much less than the mean free path at pressures that exist in the main chamber, ensuring that ions and neutrals generated in the plasma do not undergo collisions before being sampled by the mass spectrometer. The mass spectrometer is backed by a turbomolecular pump and consists of an ion extractor, electron impact ionization source, Bessel box energy analyzer, triple-sector quadrupole mass analyzer, and secondary electron multiplier. This system is capable of scanning ion energies with 0.05 eV steps over a range of ±100 eV that is superimposed on a reference potential of up to 1000 V. The system is thus capable of measuring ion energies as high

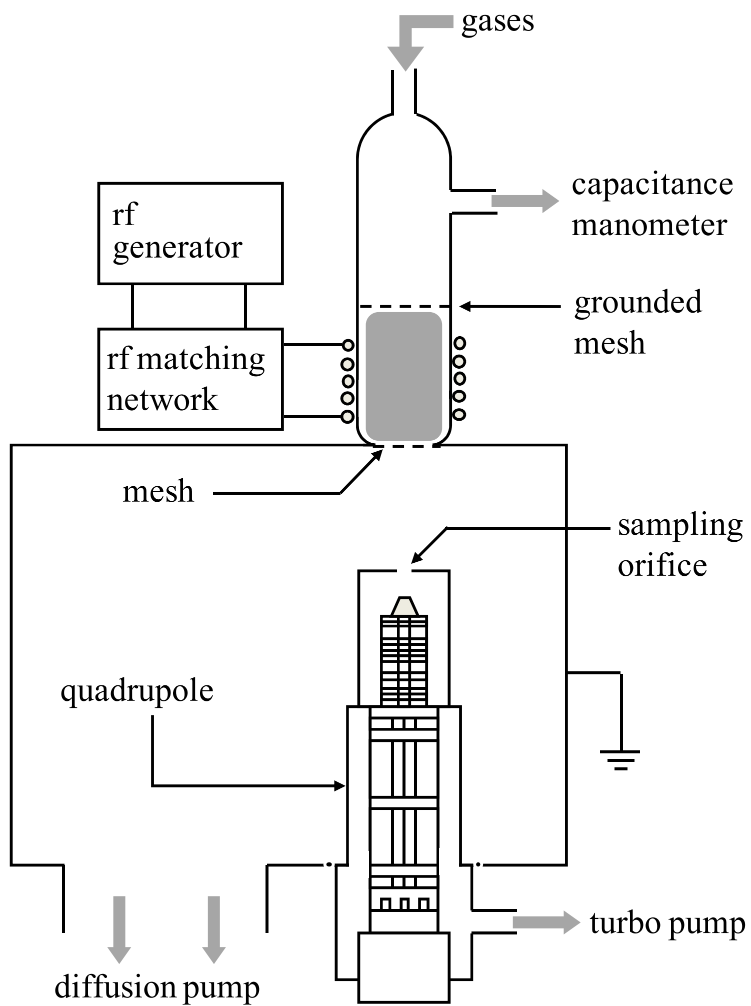

Figure 2.3 Cross-sectional schematic of the experimental apparatus used for mass spectrometry.

as 1100 eV, but in these studies, a detection window of 0-190 eV was found to be sufficient to encompass the ion energy distributions under all conditions.

LIF Spectroscopy. The apparatus used for LIF studies has been described in detail previously and is depicted in Figure 2.4. In a typical experiment, the feed gases enter the rear of a glass reactor tube, 13.56 MHz rf power is applied to an eight-loop inductor coil, and a plasma is produced. Expansion of the plasma through a series of collimating slits into a differentially pumped high-vacuum chamber generates an effusive molecular beam consisting of virtually all species present in the plasma, including the species of interest. The pressure in the main chamber of the apparatus, where measurements are made, is $\sim 1\times10^{-5}$ Torr during experiments.

Laser radiation generated by a tunable excimer-pumped (Lambda Physik LPX210i, XeCl, 180 mJ/pulse, 25-35 Hz) dye laser system serves as the laser source in the LIF experiments and intersects the plasma molecular beam at a 45° angle downstream from the plasma source, exciting a specific transition in the species of interest. A quartz lens is used to focus the laser at the position of the molecular beam, yielding a well-defined laser beam <1 mm wide at the point of its intersection with the molecular beam. All LIF experiments were performed at laser energies in the optical saturation regime; thus, the measurements are not affected by small fluctuations in laser power. The LIF signal is collected for up to several thousand laser shots per step, with the exact number dictated by the amount of signal present in each experiment. Fluorescence signal from the species of interest is collected by a set of two lenses, with focal lengths of 300 and 75 mm, imaging a 2630 mm^2 area onto the 512 × 512 pixel array of an intensified charge-coupled device (ICCD) located perpendicular to both the molecular and laser beams,

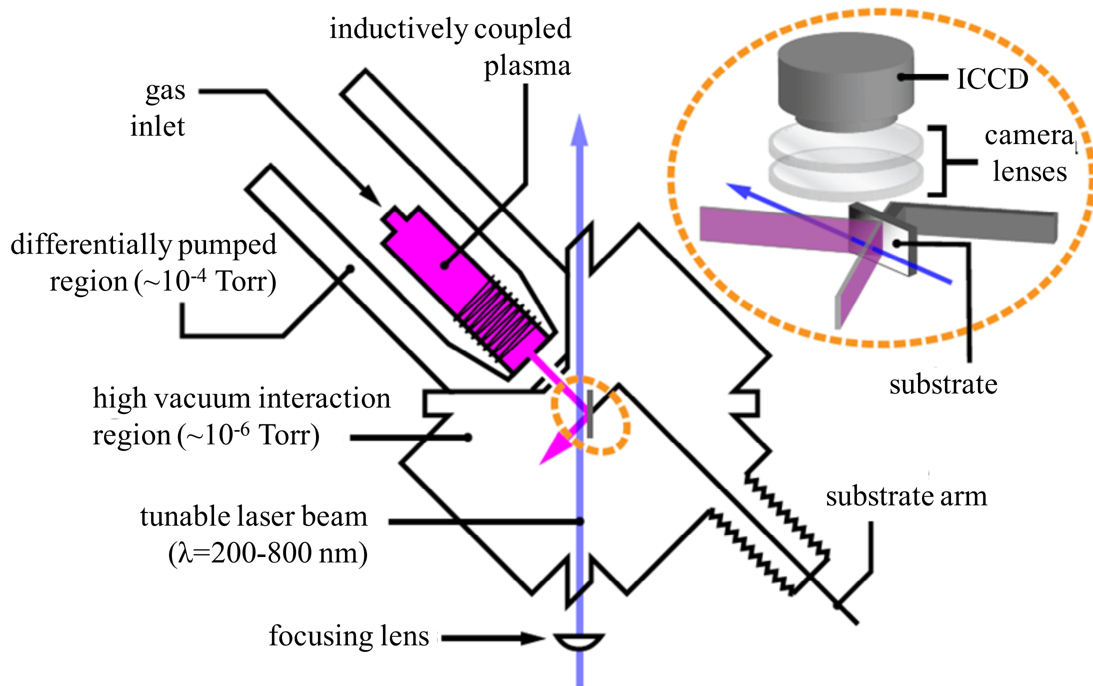

Figure 2.4 Schematic of imaging of radical interacting with surfaces (IRIS) apparatus. Detail of the interaction region shows the spatial orientation of the optics and detector relative to the molecular and laser beam.

directly above the interaction region, yielding a spatially resolved image of the LIF spot. The ICCD pixels were 4 × 4 binned, and the ICCD gate width and delay with respect to the excitation pulse were adjusted to optimize signal for the particular molecule being probed.

CN LIF Studies. In LIF studies of CN radicals (Chapters 4 and 6), the molecular beam was collimated by two slits, 1.6 and 1.7 mm wide, with the second slit 12 mm downstream from the first. Exalite 389 dye (Exciton) dissolved in 1,4 dioxane (0.07 g/L in main amplifier cell) was used in the dye laser system for excitation of the CN $B^2\Sigma^+ \leftarrow X^2\Sigma^+$ transition. For measurements of both intensity and reactivity (see below), the laser was tuned to 387.964 ± 0.003 nm (5-10 mJ/pulse), corresponding to the $P_1(N = 9)$ rotational line of the CN $B^2\Sigma^+ \leftarrow X^2\Sigma^+$ transition, Figure 2.5. The gate delay of the ICCD camera was 1550-1650 ns and the gate width was 250 ns, facilitating collection of fluorescence signal over the entire radiative lifetime of CN $B^2\Sigma^+$ state (~70 ns[6]). A 250 nm bandwidth (centered at 495 nm) interference filter was placed between the ICCD camera and the vacuum chamber to reduce spurious signals from scattered laser light and plasma emission.

Excitation spectra were collected for CN over a wide range of wavelengths (385.59-385.75 and 386.35-388.34 nm) and the vibrational and rotational temperatures (Θ_V and Θ_R, respectively) were measured using multiple lines from each region. Spectral lines were scanned in an LIF excitation spectrum, and the final temperature was determined from simulation of the corresponding CN rotational lines using the LIFBASE program,[7] optimizing Θ_R and Θ_V values to the experimental data. The collection of data over a larger spectral window (as in Figure 2.5) provides more data for comparison to

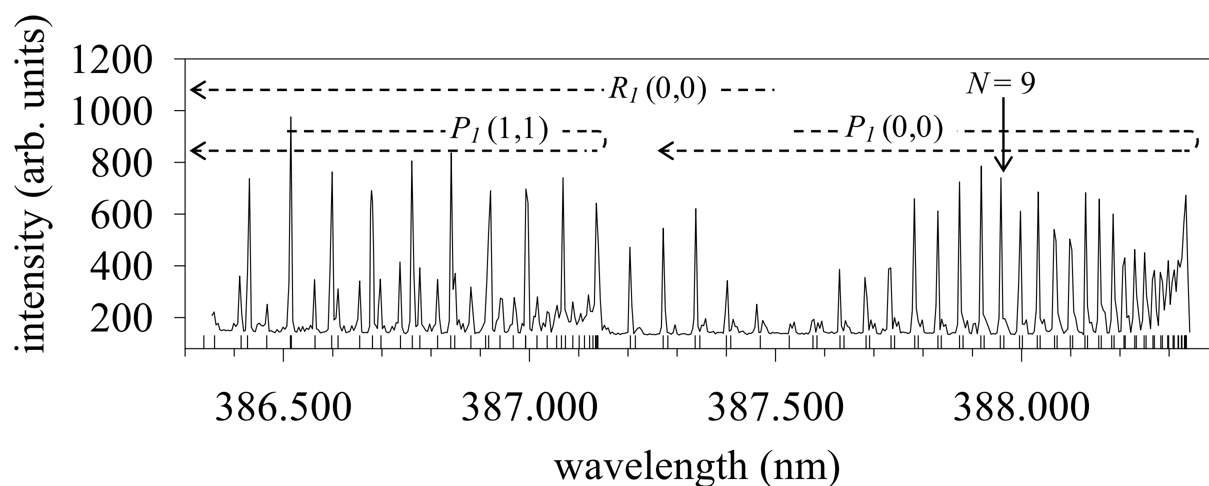

Figure 2.5 LIF excitation spectrum for the CN $X^2\Sigma^+ \rightarrow B^2\Sigma^+$ transition collected in a 100% CH_3CN plasma (50 mTorr, 150 W, 0.004 nm steps) along with calculated rotational line positions. This spectrum represents a compilation of six scans collected over different wavelength ranges. The $P_1(v'',v' = 0,0)$, $N = 9$ peak was used for gas-phase density and IRIS reactivity measurements.

simulated data but yields Θ_R values with fairly high errors because the necessarily larger step size makes fitting of the spectra more difficult. Thus, for the purposes of determining Θ_R and Θ_V, we have chosen to scan discrete portions of the CN rovibrational spectrum using smaller wavelength step sizes.

The measurement of Θ_R is most easily accomplished by measuring the intensity of spectral lines that represent significantly different rotational quantum states, and it is this relatively large difference in rotational quantum number that makes these measurements sensitive to Θ_R. Here, we use the relative intensity of rotational lines in the *P*-branch of the $\nu = 0$ vibrational band, scanned with step sizes of 0.001 nm, to determine Θ_R as a function of experimental parameters.

The resolution of the laser system used in these experiments precludes the collection of spectral scans that encompass all of the CN vibrational bands, but we have scanned individual rotational lines from the $\nu = 0$, 1, and 2 vibrational bands where they occupy the same spectral region and compared our experimental data to spectra simulated in LIFBASE to obtain an estimate of Θ_V (CN) in these systems. In simulating these spectral data, it was assumed that Θ_R for vibrational bands with $\nu > 0$ is equal to Θ_R for the $\nu = 0$ band. This is primarily because characterization of the rotational population distribution in the vibrational bands with $\nu > 0$ is complicated by the presence of overlapping bands. Although this assumption limits the accuracy of the measurement, we believe the data remain useful as a semi-quantitative measure of Θ_V.

SO_2 LIF Studies. In LIF studies of SO_2 (Chapter 8), the source of the molecular beam is a plasma consisting of SF_6 and O_2 gases, which were mixed before entering the plasma reactor. The molecular beam was collimated by two slits, 1.9 and 1.5 mm wide,

with the second slit 12 mm downstream from the first. The first slit was mounted on a liquid N_2 cooled shield (cooled to about -160 °C) to minimize desorption of SO_2 molecules from the slit surface, signal from which can interfere with the LIF signal from molecules in the molecular beam.[8,9] Rhodamine 6G dye (Lambda Physik) dissolved in CH_3OH (0.40 g/L in main amplifier cell) was used in the dye laser system, and the resulting laser light was frequency-doubled (0.5-1.4 mJ/pulse) and optimized for excitation of SO_2 radicals. Fluorescence excitation spectra were collected by scanning the laser wavelength from 287–303 nm in 0.01 nm increments and plotting the SO_2 LIF intensity as a function of laser wavelength. For measurement of both surface scatter coefficient and relative number density of ground state SO_2, the laser was tuned to 296.256 ± 0.003 nm, which was found to give the highest LIF signal. In these experiments, background images with the laser tuned to a non-resonant wavelength were taken and subtracted from each data image. Each LIF image represents 3,000-10,000 laser pulses. The ICCD camera was operated with a 5000 ns gate width, allowing collection of sufficient fluorescence signal over the radiative lifetime of the SO_2 $\tilde{A}$ state ($\tau_{rad} > 10$ μs).[10-12] The flow rates of SF_6 and O_2 were varied from 5-20 sccm, and the applied rf power was varied over the range 20-200 W.

Note that the LIFBASE program allows for spectra to be fit assuming linear, full, or partial saturation behavior. Although we operate in the optical saturation regime, the best fits to the experimental excitation spectra were found assuming a linear saturation in the simulation. This type of behavior has been seen previously and results when a laser beam interacts with a volume of gas that exceeds the focal volume of the laser.[13]

2.3 Surface Reactivity

The IRIS apparatus has been described in detail previously.[14] Briefly, IRIS combines molecular beam techniques and LIF to investigate the steady-state surface reactivity of gas phase species during plasma processing of a substrate as a function of different plasma parameters, such as applied rf power, reactor source pressure, gas composition, and substrate temperature (T_S). The apparatus used for IRIS studies is identical to that used for LIF measurements. For IRIS studies, the spatially resolved LIF intensity of a freely expanding molecular beam is compared with the LIF intensity of a molecular beam impingent on a substrate. The difference in LIF intensity is directly proportional to the density of radicals scattered or created at the substrate's surface, allowing study of the interaction of radicals in the molecular beam with surfaces. Background images were acquired with the laser tuned to an off-resonance wavelength (386.946 ± 0.003 nm) and subtracted from each image. The substrates used in these studies were roughly 30×40 mm Si and SiO_2, and the distance between the laser and substrate was 3-4 mm.

One-dimensional cross sections were generated from spatially resolved LIF data by averaging 20-pixel columns along the laser axis and plotting signal intensity as a function of distance along the laser path. Spatially resolved LIF data are interpreted using a quantitative model of the experiment that yields the surface reactivity of the species of interest. The simulation procedure has been described in detail previously.[15] The model is based on the known geometry of the experiment and calculates, assuming an adsorption-desorption scattering mechanism, the spatial distribution of the radical number density in the molecular beam at the interaction region, as well as the radical

number density along the laser beam for molecules scattering from the substrate surface. The scattering coefficient, S, defined as the ratio of the flux of scattered molecules to that of the incident beam, is adjusted to best fit the experimental data. The surface reactivity, R, is defined as $1 - S$. In these studies, R(CN) values are corrected for the effects of rotational temperature (see Appendix B for details) and are reported as a weighted average of at least three separate measurements.

For studies of the dependence of CN reactivity, R(CN), on T_S, the apparatus was modified to incorporate a heated ceramic substrate stage to which substrates were mounted using thermally stable ceramic adhesive, and a K-type thermocouple was used to monitor substrate temperature. The heated substrate stage was mated to the existing substrate arm with a U-shaped aluminum bracket, Figure 2.6. Four spring-loaded pins on this bracket were positioned to clamp onto ceramic tubes glued to the substrate stage with ceramic adhesive. The spring-loaded pins (adapted from contact probes purchased from Interconnect Specialties, Inc.) have faceted points and help minimize heat transfer from the substrate stage to the substrate arm.

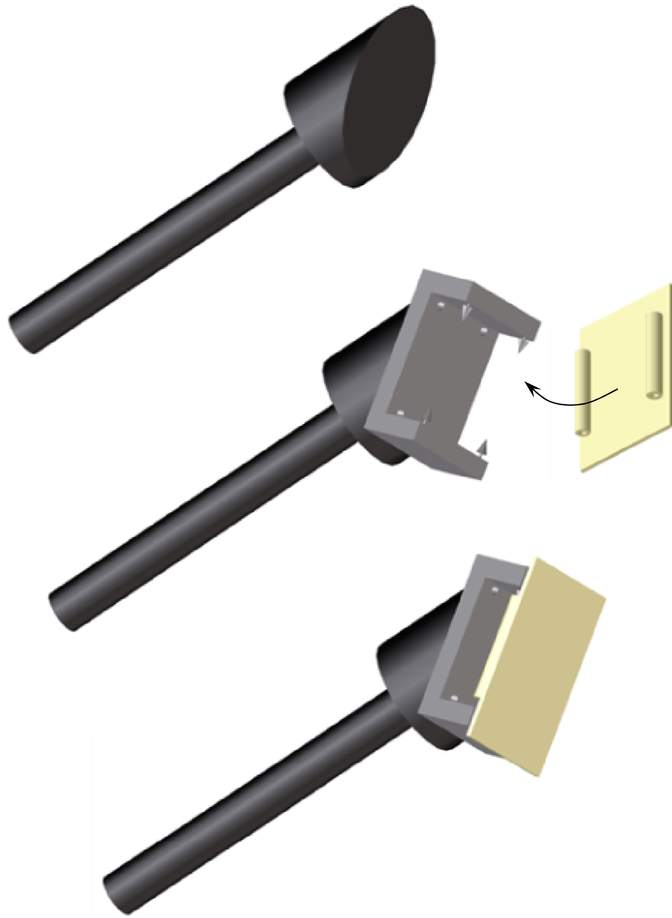

Figure 2.6 Sequential images showing assembly of heated substrate holder for measurement of *R*(CN) as a function of substrate temperature.

2.4 References

[1]K. H. A. Bogart, N. F. Dalleska, G. R. Bogart, and E. R. Fisher, J. Vac. Sci. Technol., A **13,** 476 (1995).
[2]F. Truica-Marasescu, P. Jedrzejowski, and M. R. Wertheimer, Plasma Process. Polym. **1,** 153 (2004).
[3]W. Kern and D. A. Puotinen, RCA Rev. **31,** 187 (1970).
[4]R. E. Walkup, K. L. Saenger, and G. S. Selwyn, J. Chem. Phys. **84,** 2668 (1986).
[5]J. Zhou, I. T. Martin, R. Ayers, E. Adams, D. Liu, and E. R. Fisher, Plasma Sources Sci. Technol. **15,** 714 (2006).
[6]E. D. Poliakoff, S. H. Southworth, M. G. White, G. Thornton, R. A. Rosenberg, and D. A. Shirley, J. Chem. Phys. **72,** 1786 (1980).
[7]J. Luque and D. R. Crosley, SRI International Report MP 99-009 (1999).
[8]K. H. A. Bogart, J. P. Cushing, and E. R. Fisher, J. Phys. Chem. B **101,** 10016 (1997).
[9]E. R. Fisher, P. Ho, W. G. Breiland, and R. J. Buss, J. Phys. Chem. **96,** 9855 (1992).
[10]R. Kullmer and W. Demtroder, J. Chem. Phys. **84,** 3672 (1986).
[11]H. Watanabe, Y. Hyodo, S. Tsuchiya, and S. Koda, J. Phys. Chem. **86,** 685 (1982).
[12]H. D. Metee, J. Chem. Phys. **49,** 1784 (1968).
[13]P. Ho, W. G. Breiland, and R. J. Buss, J. Chem. Phys. **91,** 2627 (1989).
[14]P. R. McCurdy, K. H. Bogart, N. F. Dalleska, and E. R. Fisher, Rev. Sci. Instrum. **68,** 1684 (1997).
[15]K. H. A. Bogart, J. P. Cushing, and E. R. Fisher, J. Phys. Chem. B **101,** 10016 (1997).

CHAPTER 3

PLASMA DIAGNOSTICS FOR UNRAVELING PROCESS CHEMISTRY

Presented in this chapter are the contents of a review article published in the *Annual Review of Analytical Chemistry* and written by Joshua M. Stillahn, Kristina J. Trevino, and Ellen R. Fisher. The article also draws on the contributions of several past coworkers, including Dr. Dongping Liu, Dr. Ina T. Martin, Dr. Patrick McCurdy, Michelle Morgan, Dr. Keri L. Williams, Dr. Jianming Zhang, and Dr. Jie Zhou.

The review focuses on the use of diagnostic tools to examine plasma processing chemistry. Several useful diagnostic tools are described along with their utility in measuring species densities, rotational and kinetic energies, and plasma-surface reactions. Molecule-surface interactions for MX_n species (M=C, Si, N and X = H, F, and Cl) are also presented and interpreted with respect to the molecule's electronic configuration and dipole moments.

3.1 Introduction

Plasmas, or partially ionized gases, are complex systems containing a range of reactive species including radicals, metastables, ions, electrons, and photons. Although plasmas can be generated in several ways, they are most commonly created in the laboratory using radio frequency (rf), microwave, or direct current (DC) applied electrical power. Because of the reactive nature of plasma species, a multitude of reactions can occur in the gas phase or at gas-surface interfaces. The result of the interactions of gas-phase plasma species with surfaces (either reactor walls or substrates) generally fall into three categories: (1) etching, or removal of material, often in a selective manner; (2) deposition, wherein a distinctly different chemical material is formed on a substrate; and (3) surface modification, which refers to implantation of chemical functional groups in the outermost surface layer. These processes all rely on a complex set of intertwined chemical reactions that are difficult to understand on a molecular level.

An additional factor contributing to plasma chemistry complexity is the number of system variables used for process optimization, including equipment variables (reactor size and configuration, materials of construction, method and amount of power applied); gas variables (pressure, flow, and gas ratios); and substrate variables (substrate temperature (T_S), material, and location in reactor). Often, small changes in a single parameter can result in large changes in the overall process chemistry. In some systems, the balance between etching and deposition is so sensitive to these parameters that controlling the outcome is challenging and can result in significant waste. Thus, it is imperative to develop analytical diagnostic tools capable of providing straightforward and reliable process chemistry data.

Understanding fundamental plasma chemistry has been an elusive goal for plasma scientists, primarily because of system complexity. Consequently, relatively little is known about mechanisms for plasma processing. Studies concentrated on correlating surface properties with plasma parameters can provide relationships between gas-phase species and processed surface composition. Although these simplistic relationships often offer support for assumptions about deposition and etching mechanisms, they do not directly address gas-surface interface chemistry and thus provide an incomplete picture. A more global representation of molecular-level chemistry is critical, but requires diagnostic tools that: allow for identification and quantification of all plasma species (charged and neutral); offer temporal and spatial resolution; can be performed in a non-intrusive manner; provide data on the gas-phase, surface, and gas-surface interface; and characterize internal and kinetic energies of plasma species to estimate rate constants and provide energy partitioning information. Clearly, no one diagnostic tool can fulfill all of these needs. Consequently, many studies focused on unraveling process chemistry rely on a combination of techniques, affording broader descriptions of plasma processes. As a result of the need for diagnostic tools in both industrial processes and fundamental studies, plasma diagnostics have been the subject of numerous review articles and books.[1-4] Here, we focus on a few complex plasma systems that have benefited from the application of highly sophisticated diagnostic tools to unravel the underlying molecular level chemistry.

3.2 Diagnostic Techniques

An array of techniques can be applied to examine plasma chemistry. Here, we focus primarily on non-intrusive, in situ optical gas-phase diagnostics, although some non-optical and surface techniques are included. This is by no means an exhaustive list, and detailed descriptions of the instruments can be found elsewhere.[1,5-7]

Optical Emission Spectroscopy (OES). OES analyzes light emitted from any medium in the absence of external excitation via collection, dispersion, and detection of the light.[1] In a plasma, gas-phase species are promoted to excited electronic states by collisions with energetic electrons and relaxation is accompanied by emission of a photon. In OES, emitted radiation is spectrally dispersed and detected. Thus, in its simplest configuration, OES requires only a means of collecting the light emitted (e.g., an optical fiber), a dispersing element (a grating) and a detector (a photomultiplier tube (PMT) or charge-coupled device (CCD)). Thus, OES is an inexpensive, real time monitoring system that can identify emitting plasma species.

OES can be employed quantitatively or qualitatively for plasma species identification and determination of absolute or relative species densities. Identification requires knowledge of emission lines of a given plasma species, Table 3.1. OES has proven useful in understanding gas-phase kinetics and reaction mechanisms, etching endpoint detection, and spatial and temporal measurements of species densities.[3,8,9] Although quantitative OES is possible, it must be used cautiously because signal intensity is not always directly related to concentration. This is often addressed with actinometry, wherein emission intensities are compared to the relatively constant emission of an actinometer, generally an inert gas (e.g., Ar) or a combination of actinometers added in

Table 3.1 Emission lines observed in OES studies of selected plasma species.

Species	Wavelength (nm)	Transition	References
Ar	696.5	$1s_5$-$2p_2$	10
	706.7	$1s_5$-$2p_3$	
	738.4	$1s_4$-$2p_3$	
	750.4	$1s_2$-$2p_1$	
	751.5	$1s_4$-$2p_5$	
	763.5	$1s_5$-$2p_3$	
	772.4	$1s_5$-$2p_7$	
	794.8	$1s_3$-$2p_4$	
	800.6	$1s_4$-$2p_6$	
	801.5	$1s_5$-$2p_8$	
	810.4	$1s_4$-$2p_7$	
	811.5	$1s_5$-$2p_9$	
	826.5	$1s_2$-$2p_2$	
	840.8	$1s_2$-$2p_3$	
	842.5	$1s_4$-$2p_8$	
	852.1	$1s_2$-$2p_3$	
C_2	469.8, 471.6, 473.7	$^3\Pi \rightarrow ^3\Pi$	11
	512.9, 516.5, 558.6	$^3\Pi \rightarrow ^3\Pi$	
	563.6	$^3\Pi \rightarrow ^3\Pi$	
C_3	405.1	$A^1\Pi_u \rightarrow X^1\Sigma^+_g$	12
CF_2	251.9	$A^1B_1 \rightarrow X^1A_1$	13,14
CH	389	$B^2\Sigma \rightarrow X^2\Pi$	15
	430, 431.4	$A^2\Delta \rightarrow X^2\Pi$	16,17
CN	387.5	$B^2\Sigma^+ \rightarrow X^2\Sigma^+$	15,18
CO	283, 292.2, 297	$b^3\Sigma \rightarrow a^3\Pi$	11
	302.8, 313.8, 325.3	$b^3\Sigma \rightarrow a^3\Pi$	
	451.1, 483.5, 518.6, 561	$B^1\Sigma^+ \rightarrow A^1\Pi$	
F	685.4	$3p^4D_{7/2} \rightarrow 3s^4P_{5/2}$	19
	703.7, 712.8	$2p^43p \rightarrow 2p^43s$	20
H	434, 486.1, 656.5	$^2P^0 \rightarrow ^2D$	11
N	674	$4d^4P \rightarrow 3p^4P^0$	15
O	777.2, 844.7	$^3S^0 \rightarrow ^3P$	11
NO	247.9, 288.5, 289.3, 303.5, 304.3	$A^2\Sigma^+ \rightarrow ^2\Pi$	11
	319.8, 320.7, 337.7, 338.6	$A^2\Sigma^+ \rightarrow ^2\Pi$	
N_2	315.9, 337.1	$C^3\Pi \rightarrow B^3\Pi$	11
OH	281.1, 306.4, 307.8, 308.9	$^2\Sigma \rightarrow ^2\Pi$	11

small quantities. Time-resolved OES (TR-OES) has also been employed.[21] OES is limited to excited state species that radiatively decay and the detectable wavelength range is hindered by the collection window, generally precluding vacuum ultraviolet (VUV) emitters. Instrument resolution (often only ~0.5-1 nm) and signal-to-noise ratios also limit the utility of OES.

Optical Absorption Spectroscopy (OAS). OAS is an alternate probe for excited state species and measures the light absorbed by a sample at a particular wavelength. OAS is used to probe highly excited molecules because these states are long-lived, yet do not decay via emission of a visible photon. Thus, they are not easily probed by OES.[1] OAS spectrometers consist of a light source, typically a tungsten-filament or gas-discharge lamp, which is directed into a sample chamber, and a detector placed on the opposite side of the sample to analyze transmitted light.[22] Thus, OAS is comparable to OES in equipment simplicity.

For gas-phase OAS analyses, the light source can be tuned to a specific optical transition and time-dependent information about a particular species can be obtained. Alternatively, gas phase absorption can be measured using self absorption, which is discussed in detail elsewhere.[23] This allows for quantitative analysis of absorbing species, provided line shapes and spatial distributions are known.

Laser-Induced Fluorescence (LIF). A common optical plasma diagnostic is LIF, which probes ground state species with sensitivities on the order of 10^8 cm^{-3}. An LIF apparatus generally consists of a tunable laser (e.g., excimer or Nd:YAG-pumped dye laser) and a detector situated orthogonal to the source beam to collect fluorescence. LIF occurs when molecules in the sample volume undergo resonant absorption upon

interaction with laser light of the correct wavelength.[1,24] Relaxation via spontaneous emission generates photons that are collected by the detector. The relationship between LIF intensity and number density of a species depends on intensity of the laser, the transition's quantum efficiency, and the detector's spectral response.[7,24] Table 3.2 lists spectral details for specific LIF-probable transitions of plasma species.

LIF plasma experiments can provide relative and absolute number densities,[7,24-26] gas temperature (T_g), and surface reactivities. LIF techniques that make use of optical evanescent waves, which allows characterization of plasma processes in the near surface region, can provide relative densities and surface reactivities.[27] Other LIF techniques provide data on kinetics[28] and electric fields in plasmas.[29] Spatial resolution of LIF signals allows measurement of velocity distributions,[30-32] yielding convection and diffusion data[29] and mechanisms for energy partitioning.[30,31] LIF only probes ground state species, and only those that possess a fluorescing excited state. LIF is not well-suited to process control, primarily because of the required laser-system maintenance, and is also hindered by non-radiative relaxation processes.

Imaging of Radicals Interacting with Surfaces (IRIS). One special adaptation of LIF as a plasma diagnostic is the IRIS technique that combines molecular beams with spatially-resolved LIF to explore radical-surface interactions during plasma processing.[33] Gas-phase density and surface reactivity measurements are made as a function of parameters such as applied power (P), substrate material, and T_S. Effects of ion bombardment can be explored using a grounded mesh in the molecular beam path to remove charged species,[34] biasing the substrate,[30,35,36] or employing an alternate, ion-free molecular beam source (e.g., hot-filament CVD (HFCVD)).[37] IRIS can determine

Table 3.2 Spectroscopic properties, dipole moments relative surface reactivites, and selected LIF studies of plasma species.

Species	Plasma Source(s)	Excited Transition	λ(nm)[a]	Radiative Lifetime (ns)	Dipole Moment (D)	Relative Surface Reactivity[b]	References
C_2	C_xH_y	$A^1\Pi \leftarrow X^1\Sigma^+$	691	1.85×10^4	---	---	1
C_3	C_xH_y	$A^1\Pi \leftarrow X^1\Sigma^+$	410	200	0.44	low/moderate	2,3
CH	C_xH_y, CH_3OH	$A^2\Delta \leftarrow X^2\Pi$	430	537	0.55	high	2,4
CHF	CH_xF_{4-x}	$A^1A'' \leftarrow X^1A'$	571	2.45×10^3	1.30	low/moderate	5
CF	C_xF_y	$A^2\Sigma^+ \leftarrow X^2\Pi$	224	26.7	0.64	low/moderate	6
CF_2	C_xF_y	$A^1B_1 \leftarrow X^1A_1$	226	61	0.44	low	6,7
CCl	CCl_4, CH_4/Cl_2	$A^2\Delta \leftarrow X^2\Pi$	279	105	---	---	8
CN	CH_3CN, CH_4/N_2	$B^2\Sigma^+ \leftarrow X^2\Sigma^+$	387	65	1.47	high	9,10
NH	NH_3, N_2/H_2	$A^3\Pi \leftarrow X^3\Sigma^-$	336	440	1.39	low/moderate	11
NH_2	NH_3, N_2/H_2	$A^2A_1 \leftarrow X^2B_1$	598	10×10^3	1.82	moderate	11
NO	NO, N_2/O_2	$A^2\Delta \leftarrow X^2\Pi$	226	205	0.16	---	12,13
OH	H_2O, H_2/O_2	$A^2\Delta \leftarrow X^2\Pi$	308	686	1.80	moderate	14,15
SiCl	$SiCl_4$, Cl_2[c]	$B^2\Sigma^+ \leftarrow X^2\Pi$	297	10	---	---	16
$SiCl_2$	$SiCl_4$, Cl_2[c]	$A^1B_1 \leftarrow X^1A_1$	320	4.5×10^3	1.46	low	17
SiF	SiF_4, CF_4[c], SF_6[c]	$A^2\Sigma \leftarrow X^2\Pi$	437	230	1.07	moderate	18,19
SiF_2	SiF_4, CF_4[c], SF_6[c]	$A^1B_1 \leftarrow X^1A_1$	225	6.2	1.23	low	19,20
SiH	SiH_4, Si_2H_6	$A^2\Delta \leftarrow X^2\Pi$	413	534	0.14	high	21,22
SiH_2	SiH_4, Si_2H_6	$A^1B_1 \leftarrow X^1A_1$	580	111	0.16	moderate	23
SO	SO_2, SF_6/O_2	$B^3\Sigma \leftarrow X^3\Sigma$	235	16.2	1.55	---	24
SO_2	SO_2, SF_6/O_2	$A^1B_1 \leftarrow X^1A_1$	300	10×10^3	1.63	---	24

[a]Excitation wavelength for listed transition.
[b]Relative reactivity scale: low = < 0.1; low/moderate = ~0.1–0.3; moderate = ~0.3–0.7; high = ~0.7–1.0.
[c]Species of interest is produced during Si processing.

References for Table 3.2

[1]C. Suzuki, K. Sasaki, and K. Kadota, Jpn. J. Appl. Phys., Part 1 **38,** 6896 (1999).
[2]J. Luque, W. Juchmann, and J. B. Jeffries, J. Appl. Phys. **82,** 2072 (1997).
[3]D. Liu and E. R. Fisher, J. Vac. Sci. Technol. A **25,** in press (2007).
[4]J. Zhou and E. R. Fisher, J. Phys. Chem. B **110,** 21911 (2006).
[5]D. Liu, I. T. Martin, and E. R. Fisher, J. Appl. Phys.**,** manuscript in preparation (2008).
[6]J. P. Booth, H. Abada, P. Chabert, and D. B. Graves, Plasma Sources Sci. Technol. **14,** 273 (2005).
[7]I. T. Martin and E. R. Fisher, J. Vac. Sci. Technol. A **22,** 2168 (2004).
[8]R. A. Gottscho, R. H. Burton, and G. P. Davis, J. Chem. Phys. **77,** 5298 (1982).
[9]H. Ito, S. Y. Ichimura, K. C. Namiki, and H. Saitoh, Jpn. J. Appl. Phys., Part 1 **42,** 7116 (2003).
[10]D. Liu and E.R. Fisher, J. Vac. Si. Technol. A **25,** 1519 (2007).
[11]M. L. Steen, K. R. Kull, and E. R. Fisher, J. Appl. Phys. **92,** 55 (2002).
[12]X. Hu, G.-B. Zhao, S. V. B. Janardhan Garikipati, K. Nicholas, S. F. Legowski, and S. Radosz, Plasma Chem. Plasma Process. **25,** 351 (2005).
[13]F. Fresnet, G. Baravian, S. Pasquiers, C. Postel, V. Puech, A. Rousseau, and M. Rozoy, J. Phys. D: Appl. Phys. **33,** 1315 (2000).
[14]K. H. A. Bogart, J. P. Cushing, and E. R. Fisher, J. Phys. Chem. B **101,** 10016 (1997).
[15]E. R. Fisher, P. Ho, W. G. Breiland, and R. J. Buss, J. Phys. Chem. **97,** 10287 (1993).
[16]V. M. Donnelly, I. P. Herman, C. C. Cheng, and K. V. Guinn, Pure Appl. Chem. **68,** 1071 (1996).
[17]D. Liu, I. T. Martin, J. Zhou, and E. R. Fisher, Pure Appl. Chem. **78,** 1187 (2006).
[18]K. L. Williams and E. R. Fisher, J. Vac. Sci. Technol. A **21,** 1024 (2003).
[19]K. L. Williams and E. R. Fisher, J. Vac. Sci. Technol. A **21,** 1688 (2003).
[20]G. Cunge, P. Chabert, and J. P. Booth, Plasma Sources Sci. Technol. **6,** 349 (1997).
[21]J. Zhou, J. Zhang, and E. R. Fisher, J. Phys. Chem. A **109,** 10521 (2005).
[22]W. M. M. Kessels, P. R. McCurdy, K. L. Williams, G. R. Barker, V. A. Venturo, and E. R. Fisher, J. Phys. Chem. B **106,** 2680 (2002).
[23]M. Hertl and J. Jolly, J. Phys. D: Appl. Phys. **33,** 381 (2000).
[24]K. E. Greenberg and P. J. Hargis, Jr., J. Appl. Phys. **68,** 505 (1990).

velocities by exploiting the time resolution of the CCD,[31,32,38] and uses MS to study plasma ions.[34,36]

Figure 2.4 shows a schematic of the IRIS apparatus.[33] In a typical IRIS experiment, feed gases enter a tubular reactor and rf power is applied to produce a plasma. Expansion into a differentially pumped vacuum chamber generates an effusive molecular beam containing virtually all plasma species. A tunable laser intersects the molecular beam and spatially-resolved LIF signals are collected by a CCD located perpendicular to the interaction region. For reactivity measurements, a substrate is rotated into the molecular beam path, Figure 2.4, and LIF signals are again collected. Differences between spatial distributions with and without the surface (see Figure 4.5 for examples) provide radical-surface interaction data.

Spatially-resolved LIF images are interpreted using a quantitative model that reproduces the scattering data in 1D.[33,39] The model calculates the scattering coefficient (S), the fraction of incident radicals scattered from the surface, which is adjusted to best fit the experimental data. For molecules produced at the surface, $S > 1$, whereas for molecules lost at the surface, $S < 1$. Surface reactivity, R, is defined as $1-S$ and is equivalent to surface loss probability, β, the fraction of gas-phase molecules lost upon interaction with a surface, regardless of loss mechanism.

Cavity Ringdown Absorption Spectroscopy (CRDS). CRDS uses laser pulses to measure absorption of a sample placed directly in the optical cavity of a laser. This is accomplished by measuring the temporal decay in the intensity of light leaving the laser's output coupler. The time required for the output signal to decay to a fraction, 1/e, of the initial value is the ringdown time, providing a single pass transmission coefficient. At

non-resonant wavelengths, the ringdown time can be used to correct for effects of mirror reflectivities and cavity dimensions. At resonant wavelengths, sample absorption causes additional signal decay, which can be converted to an absolute absorption.[6,40] Because of its time-dependence, CRDS offers increased sensitivity over conventional OAS. CRDS is well-suited to plasma systems because the sample is in the laser cavity, providing long effective path lengths, and permitting analysis of strongly absorbing species in trace amounts or weakly absorbing species in larger concentrations.[41] Although CRDS is less sensitive than "background free" techniques such as LIF and resonant enhanced multi photon ionization (REMPI), it can be applied when fluorescence and ionization are not practical.[40] CRDS can provide absolute densities,[42] gas-phase loss rates, and β values.[43-45]

Langmuir Probes. The most widely used electrical plasma probe is the Langmuir probe,[22,46] which measures the plasma current potential (*I-V*) relationship, and functions similar to electrodes in electrochemical cells. Probes can be run effectively in potential sweep mode, similar to cyclic voltammetry. From the resulting data, electron and ion distribution functions are derived, providing electron temperature, T_e, electron density, n_e, and plasma potential, V_p. Langmuir probes often have reference electrodes or double probes, wherein a second electrode is part of the electrical circuit.[22,47] Double probes are preferred as they do not present as large a perturbation to the plasma, critical for probe theory validation. A distinct disadvantage arises from probe contamination from sputtered or deposited material affecting the probe's ability to accurately describe V_p.[46]

Fourier Transform Infrared Spectroscopy (FTIR). FTIR is a vibrational spectroscopy applicable across a range of chemistries. FTIR plasma diagnostics focus on

both the gas phase and processed surfaces.[5,48] The gas phase can be analyzed as a non-intrusive in situ probe in the exhaust region to monitor plasma effluent,[49] which also provides information on plasma-generated species. Determination of parent molecule breakdown in the reactor helps ensure the desired chemistry is occurring. FTIR analysis of a plasma-processed sample can occur both in situ, by monitoring the gain or loss of a particular species on the substrate, or ex situ by removing the substrate from the system.

Mass Spectrometry (MS). Quadrupole mass spectrometers[50] are the most common MS instruments used in plasma diagnostics.[51] QMS provides several analytical advantages, including fast analysis with good sensitivity, compactness, and ruggedness. In general, a mass spectrometer consists of an ion source, an analyzer, and a detector. A common ionization source is electron impact, which allows adjustment of the electron energy. Threshold ionization mass spectrometry (TIMS, or appearance potential mass spectrometry (APMS)) uses this source for the detection of neutral radicals by ramping the impact energy of source electrons, yielding successive rises in ion signal and distinguishing species with the same mass-to-charge ratio.[50,52-54]

In addition to providing identity and concentration of plasma species, retarding field analyzers or ion optic elements can be incorporated to characterize ion energy distributions (IEDs). Analysis of IEDs can be used to study the angular distribution of plasma ions.[55] This is especially relevant in etching, where angles of incidence influence etch rates and profiles. Other MS adaptations include cryotrapping assisted MS (CTAMS), in which successive outgassing of cryotrapped plasma species provides mass spectra in complex deposition plasmas,[56] and temperature programmed desorption (TPD), in which a QMS is used to detect desorbing species.[57]

Spectroscopic Ellipsometry (SE) and Second Harmonic Generation (SHG). Ellipsometry involves the measurement of changes in the polarization of light when reflected from a surface.[1] It is non-invasive and can provide in situ characterization of plasma-deposited films. The experimental reflection coefficient ratio can be compared to a model of the material structure to determine thickness and dielectric function. Refractive index, microstructure, and density data can also be determined. SE can achieve sub-monolayer resolution (~0.01 nm), but data quality depends largely on how well the model approximates the experimental system. Although SE is useful in characterizing buried interfaces, analysis becomes increasingly difficult with thicker films. Phase modulated SE (PMSE) is an in situ probe of surface bonds during etching.[58,59]

SHG is related to ellipsometry in that incident light causes variations in the polarization of affected molecules, thereby generating a second electromagnetic field. When this occurs via a linear process, the polarization is linearly proportional to the incoming field, and the generated and incident fields have the same frequency. With more intense light (i.e., a laser), additional terms must be included; in SHG, these are associated with generation of a field whose frequency is twice that of the incident light.[1,60] SHG signals from an interface are reflected and the polarization components are analyzed, the intensity of which depends on the sample's susceptibility.[61] With centrosymmetric media, bulk molecules possess zero susceptibility and do not create a second harmonic response. This symmetry breaks down at a surface,[60] and the sensitivity of SHG to interfaces (exposed and buried) is a particular strength. SHG can be applied under many experimental conditions, and does not require sample isolation in vacuum.

Thus, it can be performed in situ to obtain time-resolved data on adsorption dynamics, orientation, surface charge, and number density of interfacial species with submonolayer sensitivity.[62-64]

3.3 Chemistry of Specific Systems

Many plasma systems have benefited from application of a combination of diagnostic tools, with a focus on understanding the synergy between gas-phase chemistry and the resulting process: etching, deposition, or surface modification. We have selected a few major systems to review here, with an emphasis on understanding the plasma-surface interface.

A. CF_x Plasma Chemistry. Early spectroscopic studies in FC plasmas focused on CF and CF_2, examining spectral characteristics using a FC electrodeless discharge as the CF_x source,[65,66] which was the beginning of understanding CF_x plasma chemistry and properties. Mathias and Miller examined polytetrafluoroethylene (PTFE) decomposition in microwave discharges, identifying C_xF_y products along with SiF_4, CO_2, CO and COF.[67] Proposed mechanisms for plasma-surface interactions included both thermal and radiation-induced reactions. This early work provided a foundation for subsequent studies of FC plasma-surface interactions.

Interest in FC plasmas rose dramatically as the microelectronics industry developed because of the exceptional etching capabilities. This is reflected in comprehensive reviews of the recombination chemistry and parameters affecting etched surfaces.[68-70] Numerical modeling has also offered insight into FC plasma etching.[71,72] Key findings clearly demonstrate ions and neutrals are both central to etching and

deposition mechanisms. Moreover, it is the synergistic activity of FC species in the gas phase and at the processed substrate surface that allows for the development of FC plasma applications.[73]

***CF_x* Density Measurements.** Identification of gas-phase species and changes in density as a function of plasma parameters can help elucidate plasma chemistry. Thus, many FC plasma studies have measured CF_x and CF_x^+ densities using multiple techniques and exploring parameter-based trends. Kiss et al. used LIF and OES to measure the relative densities of CF and CF_2 in CF_4/Ar plasmas.[74] The two techniques provided comparable results and showed LIF results were linearly correlated with actinometric OES results. Booth and coworkers measured relative CF_x densities and internal temperatures with UV-OAS,[13,75] and employed LIF and CRDS in CF_4 capacitively-coupled plasmas (CCPs) to measure absolute CF and CF_2 concentrations.[41,76] CRDS results gave [CF] = 6×10^{11} cm^{-3} in the reactor center, which was considerably lower than that obtained with LIF. The LIF studies demonstrated, however, that [CF] decreased with distance from the electrode. [CF_2] could not be determined with CRDS, but LIF yielded [CF_2] ~ 6.8×10^{12} cm^{-3} near the powered electrode, decreasing with distance from the electrode, similar to CF.

In related studies, [F] in a CF_4 CCP was measured by combined LIF and OES measurements.[26] Using [CF_2] measured by LIF and the actinometric OES ratio of I_F/I_{Ar}, where I_F and I_{Ar} are emission intensities of the F and Ar signals, respectively, Cunge et al. determined the absolute [F] with and without a Si substrate. [F] without a Si substrate increased as a function of *P*, to a maximum of ~6.5×10^{14} cm^{-3}. With a Si substrate, [F] was substantially lower because etching reactions allow for recombination with etch

products. Graves and coworkers measured neutral and ionic number densities in CF_4 inductively coupled plasmas (ICPs) using APMS, QMS and a Langmuir probe.[52,77] A key result was that [CF_x] varies with wall conditions, suggesting wall interactions control FC gas-phase chemistry.

FC plasmas are known to selectively etch Si over SiO_2, primarily as a result of different plasma-surface interactions. Miyoshi and coworkers used computerized tomography OES (CT-OES) to measure the spatio-temporal structure of etchants, etch products and their daughter products during Si and SiO_2 etching in CF_4/Ar mixtures.[78] They measured number densities of excited Ar, Si, SiF, and F and found [F*] decreased as the Si etching rate increased, whereas [SiF*] increased during SiO_2 etching. This was attributed to the deposition regime in SiO_2 etching, wherein FC film deposition prevents reactive etchants such as F atoms and CF_x^+ ions from reaching the underlying SiO_2 layer. Studies such as these provide insight into selective etching mechanisms in FC plasmas.

CF_x Energetics. Understanding the dynamic processes that influence plasma species behavior is critical to refining overall etch or deposition processes in FC plasmas. The kinetic behavior of plasmas relies heavily on the energies of its constituents; thus, measurement of T_e and T_g, provides one method for examining energy distribution in a plasma. Donnelly and coworkers applied trace rare gas OES (TRG-OES) to measure T_e and T_g in C_2F_6/C_4F_8 plasmas.[79] The feedgas also included a carrier gas and multiple inert probe gases (He, Ne, Ar, Kr, and Xe). The emission behavior of probe gases are predictable from excitation cross sections and relaxation processes. Each gas is sensitive to a different part of the electron energy distribution function; collectively, their emission intensities provide a description of T_e. Emission spectra with N_2 as the probe were used

to characterize T_g from analysis of N_2 rotational spectra. Both T_e and T_g were strongly dependent on carrier gas, suggesting careful selection of carrier gas could provide another degree of control over the energies of plasma species.

Measurements of internal and translational energies of plasma species also provide estimates of T_g. Nagai and Hori measured the rotational temperature (Θ_R) of CF in CF_4 and CF_4/Ar plasmas using OES and IR laser absorption spectroscopy (IRLAS).[80] Θ_R increased from 300 to 380 K as P increased from 375 to 1500 W, and was accompanied by a ~3-fold increase in [CF]. With CF_4/Ar, Θ_R and [CF] were substantially lower, with Θ_R only increasing by ~20 K over the same P range. This likely results from increased elastic collisions leading to CF rotational cooling, and demonstrates rotational heating is not appreciable in these systems. Similar values were obtained using planar LIF to create 2D maps of Θ_R(CF) in CF_4 CCPs.[81] Θ_R displayed strong gradients, increasing with distance from electrodes. These results have implications for density and kinetics studies that examine only a single rotational state.

Both negative and positive ions significantly influence FC plasma etching processes. Negative ion decay occurs only through ion-ion recombination in the plasma bulk. Hebner and coworkers used photodetachment spectroscopy to measure the F^- absolute density in CF_4, C_2F_6, and CHF_3 plasma afterglows.[82] The [F^-] time-dependence yielded ion-ion recombination rates of 0.88×10^{-6}, 1.5×10^{-6}, and 3.9×10^{-6} cm^3/s for CF_4, C_2F_6 and CHF_3, respectively. Positive ions can strongly influence the net rate of ion-ion recombination. The dominant positive ion is CF_3^+ for CF_4 and C_2F_6 plasmas, but CF_2^+ dominates CHF_3 plasmas, suggesting CF_2^+ enhances ion-ion recombination rates in FC plasmas.

Hancock et al. measured F atom emission at different delay times after the power-off in FC plasmas using TR-OES.[83] Decay was attributed to gas-phase recombination processes and losses at the reactor walls. Addition of a Si substrate increased etching reactions, thereby dramatically increasing the decay, whereas addition of O_2 significantly increased [F]. VUV-OAS results of Sasaki et al. indicate rapid decay in [F] in the initial afterglow of their CF_4 plasma, followed by an exponential decay in [F] at longer times. This was attributed to the initial reaction of CF_x on reactor walls and simple diffusion to, and loss at, wall surfaces in the afterglow. These mechanisms are supported by QMS, Langmuir probe and OES studies of Sugai et al. who found heated reactor walls (100-200 °C) resulted in large increases in [CF_x].[84] Using in situ FTIR, OES, and ex situ ATR-FTIR, Goeckner and coworkers[85] found CF_x was lost on low temperature walls in CF_4 plasmas, but preferentially desorbed at high temperatures. They also concluded that both film deposition and etch rate were determined by two major competing processes, direct ion incorporation and ion-assisted surface desorption.

Surface Interactions. In FC plasmas, etching and deposition are competitive processes and often occur simultaneously.[68] Species density studies as a function of plasma parameters reveal film formation and etching are controlled by interactions of plasma species with the substrate. The balance between highly energetic ions and neutral radicals bombarding the substrate dictates the dominant process.

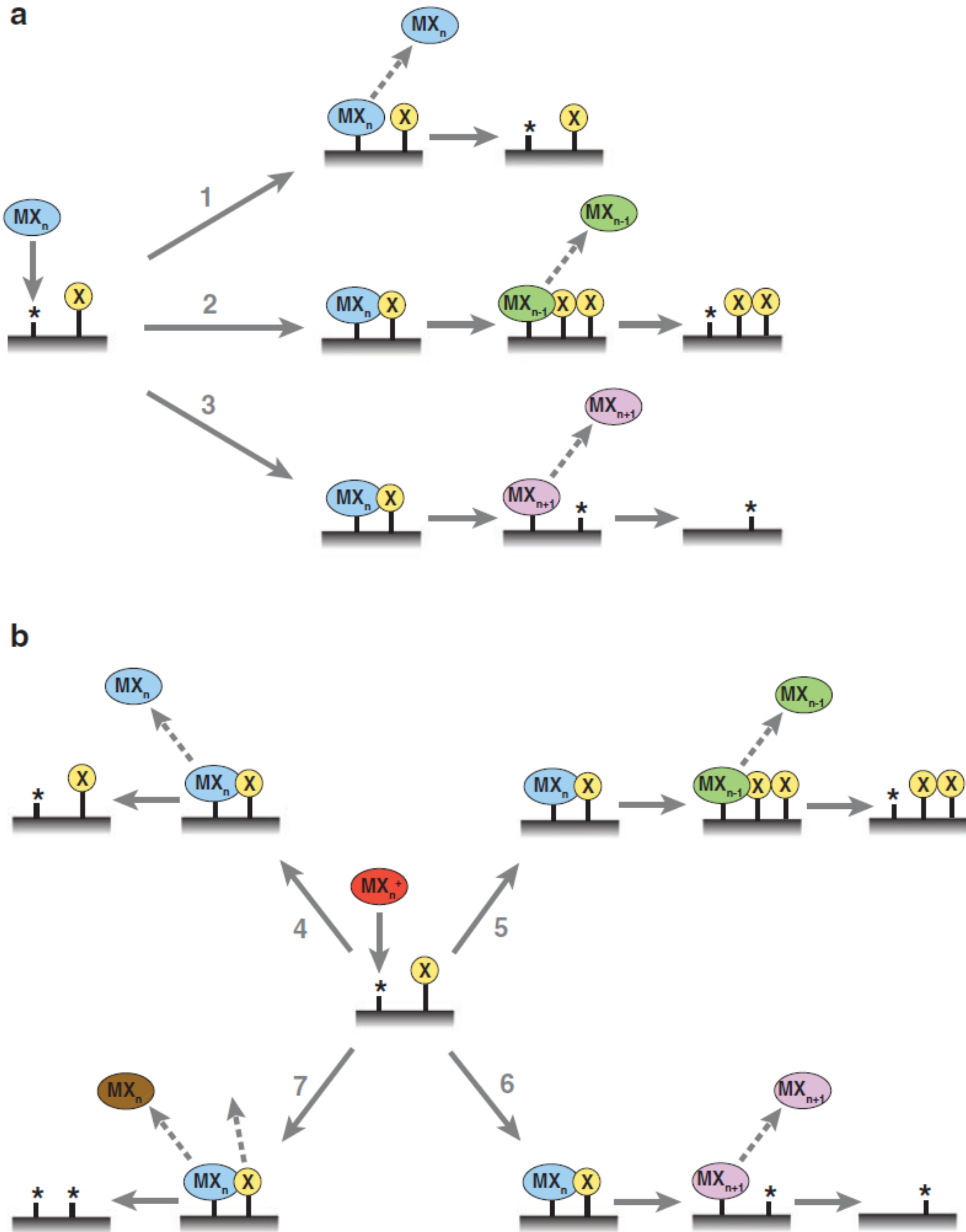

Figure 3.1 Generalized schematic representation of (a) neutral and (b) ionic plasma species interacting with a substrate. Process (1) represents simple adsorption-desorption from a surface, usually with thermal equilibration. Processes (2) and (3) represent dissociative and recombinative adsorption, respectively, with subsequent desorption of products to form an active surface site (*). Processes (4)-(6) are similar to processes (1)-(3) but include surface neutralization of the incident ion. Process (7) represents ion-induced sputtering, wherein multiple volatile reaction products can be formed.

Radical-Surface Interactions. Radical-surface interactions are key steps leading to FC film deposition and to etching of Si substrates. In general, it is assumed that when radicals impinge on a surface, they react with unit probability, essentially the first step in all three radical-surface processes depicted in Figure 3.1a. Indeed, this assumption is regularly made in computer simulations where no experimental data are available. Surface loss, however, can occur via several different processes, including dissociative adsorption, process (2), Figure 3.1a, or surface atom abstraction, process (3), Figure 3.1a. In both cases, the newly formed species can subsequently desorb (as shown), but whether desorption occurs or not, these processes contribute to β. Although the first step of process (1) depicts simple adsorption, which contributes to β, subsequent desorption would result in higher S. CF_x (x = 1-3) are proposed as critical components in FC polymerization.[86-88] Radicals contribute to polymer growth by reacting with "activated" sites on the polymeric surface or by forming addition compounds through gas-phase reactions. Despite these predicted behaviors, growth mechanisms remain unclear, and β values measured during plasma-surface interactions are critical to obtaining a full understanding.[89]

$\beta(CF_x)$ appear to vary dramatically with plasma gas chemistry, surface conditions, and wall history. For example, Booth and coworkers used LIF to measure β (CF) = 0.06-0.24, depending on [F*(g)*].[76,90] APMS measurements of β(F) and $\beta(CF_x)$ on the walls of an ICP reactor were strongly dependent on wall conditions.[91] Hikosaka et al. found that $\beta(CF_2)$ and $\beta(CF_3)$ measured by TIMS were nearly identical in CF_4 plasmas (~0.13), but β decreases by ~10^2 for both species when H_2 is added.[92] In general, CF_x (x

= 1-3) species have low β, and all appear to be strongly coupled to the conditions under which measurements are made.

IRIS studies demonstrated that CF_2 is generated at surfaces (i.e., $S > 1$; $\beta < 0$) under etching conditions (e.g., 100% C_2F_6 plasmas); however, $\beta \sim 0.2$ when a-C:F,H films are produced from 50/50 C_2F_6/H_2 plasmas.[86] IRIS studies of CF_2 using hexafluoropropylene oxide (HFPO), CHF_3, C_3F_8, and C_4F_8 plasmas[14,86,87,93] have yielded three key observations: $S(CF_2)$ is nearly always greater than unity, indicating surface generation of CF_2 during FC processing; $S(CF_2)$ increases with P; and $S(CF_2)$ decreases under ion-free conditions. Time-resolved UV-OAS data for C_2F_4 and HFPO CCPs also found significant CF_2 surface production.[94] Booth and coworkers determined both CF and CF_2 are produced at surfaces in CF_4 plasmas.[26,76,90] Their proposed mechanism relies on energetic ion-surface interactions producing CF_x, either through CF_x^+ neutralization, process (4) Figure 3.1b, or via film sputtering, process (7) Figure 3.1b. With no ion bombardment, many surfaces act as CF_x sinks. These observations indicate CF_2 surface production is strongly correlated to plasma ions. Indeed, Martin et al. found a positive linear correlation between mean ion energy, $\langle E_i \rangle$, in C_3F_8 and C_4F_8 plasmas and $S(CF_2)$.[34] An additional correlation was observed between $S(CF_2)$ and FC film crosslinking for several FC systems.[95] Conditions leading to highly crosslinked films result in higher $S(CF_2)$. Overall, when the surface is not bombarded by energetic species (e.g., ions), CF_2 is contributing to film formation, resulting in a more ordered (high CF_2 content) material.[37]

Ion-Surface Interactions. Given the above, ions clearly play a significant role in both FC plasmas etching and deposition; possible ion-induced mechanisms are shown in

Figure 3.1b. To clarify this role, the behavior of ions or groups of ions in an isolated environment has been investigated. Sawin and coworkers used individual beams of CF_2, F atoms (created from HFPO pyrolysis and F_2/Xe discharges, respectively) and Ar^+ to simulate the CF plasma etching environment.[96,97] Butterbaugh et al. found the etch yield saturates at lower radical flux values when the surface is bombarded with higher energy ions.[96] This was attributed to ion-induced surface roughness producing more active sites and higher β.

Hanley and coworkers examined ion-surface interactions using mass-selected beams of $C_3F_5^+$ or $C_2F_4^+$ ions.[98,99] Ions were accelerated or decelerated into a surface to examine the effects of incident ion energy on the properties of the resulting films, as measured by X-ray photoelectron spectroscopy (XPS). Ion identity and energy strongly affected film thickness and morphology, but not film composition. Goyette et al. used an electrostatic energy analyzer to examine IEDs and ion flux of CF^+ and CF_3^+ in C_2F_6 and C_4F_8 plasmas.[100] At higher pressures, ion flux increased, as did rf modulations, and IEDs were highly dependent on ion mass. Martin et al. measured IEDs, and determined $\langle E_i \rangle$ in C_3F_8 and c-C_4F_8 plasmas.[34] IEDs did not exhibit a strong dependence on ion mass, but clearly showed evidence of sheath effects, as $\langle E_i \rangle$ were relatively high. Increases in $\langle E_i \rangle$ were linearly correlated to $S(CF_2)$.

B. SiF_x Plasma Chemistry. In plasma etching (e.g., FC plasmas), SiF_x species can be volatile etch byproducts, but they can also act as deposition precursors. Thus, there are many similarities between CF_x and SiF_x plasma species and optical diagnostics can elucidate both parent FC gas dissociation and etch product behavior.[101,102] Early SiF_x studies originated with spectroscopic and thermodynamic measurements using plasmas

sources.[103-105] Subsequent studies focused on parameter dependence in processing systems. Hebner measured [CF_x] and [SiF_x] (x = 1, 2) with LIF, and found [CF_x] decreased with P and increased with pressure.[106] In contrast, [SiF_x] increased with P and pressure in C_2F_6 and CHF_3 plasmas, but was independent of pressure for C_4F_8 plasmas. These results suggest C_2F_6 and CHF_3 are more efficient Si etchants than C_4F_8. CT-OES studies of Si and SiF demonstrated production of SiF occurs via gas-phase dissociation of etch products. Other LIF studies distinguished between SiF production in the presence of ion bombardment and by chemical etching of F atoms.[107]

SiF_x Energetics. Giapis and coworkers obtained gas-phase and surface kinetics for SiF_x species using MS.[108,109] For SiF_x^+ (x = 1-3), the time-of-flight (ToF) distributions contained two components, which were attributed to thermally equilibrated species and hyperthermal products of surface reactions. Increases in T_S caused a sharp drop in the SiF_3^+ high-energy component, which suggests the mechanism favors direct surface reactions for SiF_3 formation.

IRIS studies measured Θ_R for SiF and SiF_2 by comparing surface reactivities for different rotational transitions over a range of T_S.[110] This method accounts for changes in rotational state populations for molecules that thermally equilibrate at a substrate, which can result in measured β values being larger or smaller than the true value. When $T_S = \Theta_R$ for the beam species, the state population distribution will not change upon equilibration at the surface, and β for all transitions should coincide. This analysis yielded Θ_R(SiF) = 450 ± 50 K and Θ_R(SiF_2) = 752 ± 100 K for a 170 W SiF_4 plasma. Assuming that the SiF_4 parent gas has Θ_R ~ 300 K, these values suggest thermal equilibration does not take place during surface interactions of SiF_x.[38]

***SiF$_x$* Surface Interactions.** Cunge et al. measured [SiF_2] above Si and SiO_2 substrates in a CF_4 CCP using spatially-resolved LIF.[107] SiF_2 surface generation should produce a linear decrease in [SiF_2] away from the substrate, and gas phase loss or production processes would predictably alter concentration profiles. For Si and SiO_2, no net production of SiF_2 was observed, suggesting SiF_2 is produced primarily at the substrate as an etch product. Data from the plasma afterglow characterized concentration profiles under ion-free conditions. At 50 mTorr, profiles collected 2 ms after rf power interruption reveal SiF_2 continues to be produced at the Si substrate, but is lost on SiO_2. This suggests SiF_2 production from Si results from chemical processes, but production from SiO_2 relies on other species, such as ions. At 50 mTorr, $\beta(SiF_2)$ estimates were 0.8-1.0 and 0.5-0.6 for Si and SiO_2, respectively. At 200 mTorr, β decreases to 0.04 and 0.11 on Si and SiO_2 substrates, respectively.

Williams et al. used LIF, QMS, OES, and ex situ FTIR to study SiF_x surface interactions during etching and deposition from SiF_4 plasmas.[35,110] They found T_S significantly affects mechanisms for SiF_x surface desorption, and surface adlayer composition.[110] Higher T_S resulted in increased SiF and SiF_2 scatter, presumably from increases in process (1), Figure 3.1a, although processes (2) and (3) could also contribute. Thus, elevated T_S increases etching efficiency by enhancing etch product formation. Another IRIS study examined ion influence on SiF_2 surface interactions[35] using a grounded mesh and application of ±200 V substrate bias. Changes in $S(SiF_2)$ demonstrated SiF_2 surface generation is ion-induced, Figure 3.1b, and the amount of SiF_2 generated depends more on energy transfer to the surface than on availability of chemical etching species (e.g., F).

Interestingly, ion-induced processes did not strongly influence SiF surface interactions, with β(SiF) ≤ ~0.8, depending on the overall plasma chemistry.[36,110] The combination of SiF_2 and SiF IRIS data suggested SiF is primarily a deposition precursor, whereas SiF_2 is a major etch product. IRIS studies at elevated T_S found $\beta(SiF_2)$ decreased with T_S (300-575 K), a change attributed to changing surface adlayer composition.[110] For SiF and SiF_2, β increased for T_S > 575 K, as a result of exceeding the desorption energy threshold. ToF-MS studies of SiF_x etch products suggest ion-surface interactions have two components.[108,111] One corresponds to ion equilibration at the surface, process (4), and one producing energetic surface reaction products. Thus, by controlling processes that generate high-energy species, anisotropy and undercutting issues in reactive ion etching processes may be resolved.

SiF and SiF_2 velocities derived from changes in time-delayed LIF images were converted to translational temperatures (Θ_T).[38] As P increased from 80 to 200 W, Θ_T(SiF) and $\Theta_T(SiF_2)$ increased from ~570 to 870 K and from 430 to 560 K, respectively. Differences in Θ_T for the two species were attributed to differences in mass, as lighter species will gain more translational energy. Increases with P were ascribed to increases in ion density, n_e, and collision frequency that accompany higher P. These studies establish that plasmas are not always thermally equilibrated and that T_g estimates from a single species in any plasma should be applied cautiously.

C. SiH_x Plasma Chemistry. Amorphous, hydrogenated silicon (a-Si:H) has been extensively studied because of its widespread use as an inexpensive solar cell material.[112] Although a-Si:H can be produced by a variety of methods, it is most often grown using SiH_4 or Si_2H_6 plasmas, which have afforded a plethora of fundamental experimental and

theoretical studies of gas-phase kinetics, thermodynamics, film characterization, and SiH_x measurements.[113-115]

SiH_x Energetics. Stamou et al. measured Θ_R(SiH) in SiH_4 CCPs using spatially-resolved OES.[116] Θ_R linearly decreased with increasing distance from the rf electrode, from ~2500 K to ~1975 K at 5-16 mm. This was attributed to the sensitivity of Θ_R to high-energy electrons, which are more abundant near the electrode. Θ_R(SiH) peaked 5 mm from the electrode, whereas [SiH*] was highest 7 mm from the electrode. This suggests the region closer to the electrode has more high-energy electrons, even though n_e is lower. Further from the electrode, emission intensity decreases because less SiH_4 dissociation occurs.

IRIS studies determined Θ_R(SiH) and Θ_T(SiH) as a function of P and Ar dilution.[31,117] Θ_T(SiH) > Θ_R(SiH) at all P and both are relatively constant at P > 20 W.[31] Θ_R ~ 500-600 K in all feedgas mixtures, indicating thermal equilibration of rotational energy was established.[117] Differences in Θ_R(SiH) in different studies likely result from differences in plasma configurations. Θ_T(SiH) > Θ_R(SiH) under most Ar dilution conditions, averaging ~1000 K, although in the Si_2H_6/Ar system, Θ_T(SiH) ~ Θ_R(SiH) at the highest Ar dilutions. This suggested equilibration of translational energy occurs more slowly than for rotational energy, and translational energy is equilibrated at different rates in the two silane systems.

SiH_x Surface Interactions. van de Sanden and coworkers utilized an aperture-well assembly to measure a global β value for SiH_x in $Ar/H_2/SiH_4$ plasmas.[118] The apparatus is formed by two substrates 0.5 mm apart, with a 0.1 mm slit in the upper substrate. Radicals adsorb at the lower substrate or are reflected to the underside of the

top substrate. Deposition profiles as a function of H_2 flow were related to a global β of < 0.5, which decreased with H_2 flow. This may indicate the role of SiH_3, which decreases in density with addition of H_2.

Individual contributions of Si and SiH to film growth were derived from CRDS measured densities in comparison with simulated data.[42] Experimental and simulation results suggest at low SiH_4 flows, SiH radicals are lost to charge transfer with Ar^+. SiH production reached a maximum at high SiH_4 flows, where they are predominately lost in reactions with SiH_4. β(Si) and β(SiH) were used to correlate gas phase densities to film growth contributions, revealing Si and SiH contributions are only weakly dependent on H_2 flow. Time-resolved CRDS measurements also provided estimates for β.[44] Si and SiH_3 loss rates yielded β(Si) ~1 and $\beta(SiH_3)$ ~ 0.3 in $Ar/H_2/SiH_4$ plasmas. The latter value was independent of T_S,[114] indicative of surface reactions occurring during film growth. IRIS results confirm β(SiH) ~ 1, regardless of plasma parameters, feed gas, and T_S.[31]

Few studies have focused on SiH_2 surface interactions, primarily because of its high reactivity and therefore low density in silane plasmas. Decay in $[SiH_2]$ measured by LIF in the afterglow of $Ar/H_2/SiH_4$ plasmas found $\beta(SiH_2) = 0.6 \pm 0.15$.[119] TIMS measurements of SiH_3 and Si_2H_5 decay rates in the same apparatus were related to β values using assumptions about surface processes, yielding $\beta(SiH_3) = 0.28 \pm 0.03$ and $\beta(Si_2H_5)$ ~ 0.1 - 0.3.[120] In general, molecular dynamics simulations compare favorably with experimental values for $\beta(SiH_x)$.[121-123]

D. CH_x Plasma Chemistry. Although methane plasmas are widely used to deposit a-C:H films, most studies have focused on film properties, providing scant data

on gas-phase processes.[124] The predominant species in methane plasmas are CH_3 and H atoms.[125] MS studies show, however, that larger C_xH_y ($x > 1$) species are formed in hydrocarbon plasmas.[15,124]

CH_x Energetics. Energy distribution characterization in CH_4 plasmas focused on measuring Θ_R(CH) and Θ_T(CH) in CH_4/Ar plasmas with LIF.[17] Θ_R was ~1450 K, independent of P and [Ar]. However, Θ_T(CH) was significantly higher than Θ_R, decreasing from 9000 to 2500 K as P increased from 20 to 100 W, plateauing at $P > 100$ W. A similar trend was observed in [CH], and collectively, these results were attributed to plasma coupling modes. [Ar] did not significantly affect Θ_T, but lower Θ_T occurred at higher pressures, mimicking T_e. Thus, CH is rotationally very hot and is not thermally equilibrated, with the disparity becoming more pronounced at lower P and pressures. In situ FTIR spectra were used to derive Θ_R(C_2H_2) in an expanding thermal arc plasma.[126] Although these measurements were unreliable where C_2H_2 consumption was high (low absorbances), simulated spectra reproduced the experimental data, yielding Θ_R ~300-450 K, with no dependence on gas flow.

CH_x Surface Interactions. van de Sanden and coworkers used TIMS, Rutherford backscattering, and ellipsometry to study film properties and C_xH_y species as a function of the C_2H_2/Ar flux ratio, F.[127,128] Radical densities' (~10^{16}-10^{17} m^{-3}) dependence on F were modeled and ultimately related to β. For $F < 1$, C and C_2 dominate the gas phase and are strong contributors to film growth, whereas for $F > 1$, radicals with an odd number of carbons contribute the most. Ellipsometric refractive indices were used to correlate C_3 radical density to a-C:H film quality.

CH and H radical beams in conjunction with isotope labeling and in situ

ellipsometry studies reveal a-C:H deposition mechanisms.[125,129,130] Under CH_3 radical flux, the surface coverage of methyl groups reaches a steady state. With H-beam flux, generation of active sites occurs via surface hydrogen abstraction. This leads to film erosion as neighboring active sites relax to form C-C bonds. Alternatively, active sites promote chemisorption of CH_3 and subsequent film growth. Ion-induced processes were studied by exposing surfaces to CH_3 and He^+ beams, wherein film growth was promoted via ion-induced creation of reactive sites. In plasmas, the presence of both ions and H influence film formation. The importance of H flux is supported by $\beta(CH_3)$, which increases from 10^{-4} to 10^{-2} with H atom flux, as well as by isotope labeling studies. Controlled exposure to D-labeled beams result in surface composition changes that suggest active sites can be created several monolayers deep. Deeper active sites form C-C bonds, whereas shallow sites promote CH_3 chemisorption.

Time-resolved TIMS in CH_4 plasma afterglows provide $\beta(CH_3)$ values from $[CH_3]$ decay.[120] Results show $\beta(CH_3)$ decreases from $\sim 10^{-2}$ in the plasma to $\sim 10^{-3}$ 10 ms after discharge termination, indicating active site quenching occurs rapidly. Spatially-resolved TIMS results of Sugai et al. yielded $\beta(CH_3) = 0.001$ and $\beta(CH_2) = 0.028$.[131,132] Measurements by Loh et al. using UV-OAS resulted in $\beta(CH_3) = 10^{-2}$ in CH_4/H_2 plasmas,[133] and recent IRIS studies yielded $\beta(CH)$ near unity in CH_4/Ar pasmas[17] and $\beta(C_3) = 0.1\text{-}0.4$ in CH_2F_2/C_3F_8 plasmas, depending on substrate bias and gas ratios.[134]

E. NH_x Plasma Chemistry. N_2 and NH_3 are used for nitride film deposition and polymer surface modification.

NH_x Energetics. Tahara et al. used spatially-resolved OES to investigate NH_3 and N_2/H_2 plasmas,[135] and found $T_g \sim 10^3$ K. In N_2/H_2 plasmas, T_g gradually decreases

downstream from the plasma arc. For NH_3 plasmas, Θ_R(NH) drops precipitously. Electrostatic probe measurements suggest n_e is lower in the NH_3 system, and this disparity is likely responsible for changes in Θ_R(NH). CRDS was applied to NH_x species in Ar/NH_3 plasmas to extract Θ_R(NH) = 1920 ± 100 K.[136] This is comparable to Θ_T(NH) = 1750 ± 100 K, suggesting energy equilibration of NH. Temperatures and trends found in OES and CRDS studies were comparable and suggest thermal equilibration of NH_x species occurs readily.

Several IRIS studies have focused on NH_x energetics in NH_3 plasmas. Changes in rotational spectra upon interaction with a heated substrate yielded $\Theta_R(NH_2) \sim 340$ K,[137] indicating formation of NH_2 does not involve significant rotational heating. $\Theta_T(NH_2)$ in the molecular beam averaged 500-650 K, and was positively correlated with *P*.[30,32] Θ_T of NH_2 scattered from a substrate, $\Theta_{Tsc}(NH_2)$, was lower than in the beam (300 K< Θ_{Tsc} < 550 K), but higher than T_S (300 K). Using an ion-free molecular beam, Θ_{Tsc} was much closer to T_S, indicating ion-induced processes are responsible for elevated Θ_{Tsc}.[30] In addition, Θ_{Tsc} was dependent on substrate material (metals or polymers), with polymeric substrates having a stronger *P* dependence. This suggests substrate material influences energy transfer during plasma-surface interactions.

NH_x Surface Interactions. β(NH) and $\beta(NH_2)$ measured in NH_3 plasmas show the behavior of the two species are affected in very different ways by *P*, substrate material, and the presence of ions.[30,32,138] Increases in $S(NH_2)$ with *P* are accompanied by decreased *S*(NH), suggesting NH surface generation comes at the expense of NH_2, potentially via process (2), Figure 3.1a. As $\Theta_{Tsc}(NH_2) > T_S$, NH_2 surface generation must occur via processes that do not allow full thermal equilibration at the surface.[30,32]

Processing of polymers such as polyethylene (PE) in NH_3/H_2 plasmas is controlled by gas-phase species.[139,140] OES data indicate N_2, NH, and H are dominant NH_3 decomposition products. Increases in $[H_2]$ in the feed were accompanied by decreases in PE N/C ratios because hydrogen reduces surface NH_x, ultimately promoting formation of volatile NH_x. *P* dependence data revealed that although low-energy ion bombardment activates the surface for grafting, high energy bombardment increases sputtering, process (7) and limits grafting efficiency.[141] Ishikawa et al. characterized film etching in N_2/H_2 plasmas using in situ ATR-FTIR spectroscopy and electron spin resonance (ESR).[142] With no substrate bias, treatment resulted in formation of CN and NH moieties in the film. As bias voltage was increased, these disappeared from the spectra, and at bias > 200 V, etching was observed. Although surface nitriding may produce etch resistance, N-containing etch products were detected, suggesting nitrogen both facilitates and inhibits etching. [NH] and $[NH_2]$ CRDS measurements in NH_3/Ar plasmas suggest Ar^+ undergoes charge transfer reactions with NH_3; subsequent NH_3 decomposition occurs via dissociative recombination. Thus, Ar^+ is largely responsible for the NH_3 breakdown.

3.4 Global Remarks on Plasma-Surface Interactions

The studies reviewed above clearly demonstrate that diagnostic tools reveal details of plasma process chemistry. Currently, however, only a limited number of techniques are available to determine β values for plasma species. Given the complexity of plasma-surface interactions, it would be useful to establish some global trends. One

characteristic that could be critical is the electronic configuration of unsaturated species.[143]

In addition to spectral properties, Table 3.2 contains dipole moments and relative surface reactivities (also referred to as "stickiness" factors) for plasma species. Trends that can be gleaned from these data suggest that several doublet species (SiH, CH, CN) are highly reactive, with $\beta \sim 1$ under all conditions. Other doublets, such as NH_2, OH, and SiF display moderate β during film deposition, Table 3.2. Possible explanations for the observed differences in β of these doublet species could result from relative electronegativities. Molecules with stronger dipole moments (SiF, OH, NH_2) appear to be less reactive than those with smaller dipole moments (CH, SiH, CN). Reactivities may also be related to the availability of surface reaction partners, for example H atoms.[39] The one triplet species in Table 3.2, NH, has very low β, despite having two unpaired electrons, suggesting that NH may not be an active film precursor. Finally, the isoelectronic singlet species CF_2, SiF_2, and $SiCl_2$ are clearly generated during plasma-surface interactions ($S \gg 1$). This may be related to these species' inherent stability, such that they are extremely probable reaction products. The low β values strongly suggest MX_2 species (M = Si, C; X = F, Cl) may not be film precursors, although ion-induced production of MX_2 is a significant contributor. Notably, singlet species without strongly electron-withdrawing substituents (SiH_2, C_3) exhibit moderate reactivity, suggesting these species likely contribute to film growth.

Although these are generalizations, they represent a beginning for the difficult task of characterizing plasma-surface interactions. Areas requiring continued study include: (1) measurement of internal and kinetic temperatures for multiple species within

a plasma system to determine energy partitioning and kinetics. As evident from Θ_R and Θ_T measurements discussed above, knowing only one of these does not representatively assess T_g. Moreover, data for only a single plasma species can result in a limited picture of energy partitioning. (2) Continued development of diagnostics applicable to a wider range of plasma species. CRDS is perhaps the closest to meeting this need as it has the widest applicability. (3) Increased focus on measurement of β values during processing to provide broader views of plasma chemistry. Thus, in situ measurement methods and creation of radical-surface interaction databases to describe contributions of Figure 3.1 processes to the overall plasma chemistry are critical. These efforts will significantly enhance understanding of process chemistry, with the goal of controlling plasma-surface interactions to create tailored materials.

3.5 References

[1]I. P. Herman, *Optical Diagnostics for Thin Film Processing* (Academic Press, San Diego, 1996).

[2]G. S. Selwyn, *Optical Diagnostic Techniques for Plasma Processing* (AVS Press, New York, 1993).

[3]V. M. Donnelly, in *Plasma Diagnostics*, edited by O. Auciello and D. F. Flamm (Academic Press, Boston, 1989).

[4]R. A. Gottscho and T. A. Miller, Pure Appl. Chem. **36,** 189 (1984).

[5]N. Hershkowitz and R. A. Breun, Rev. Sci. Instrum. **68,** 880 (1997).

[6]J. J. Schere, J. B. Paul, A. O'Keefe, and R. J. Saykally, Chem. Rev. **97,** 25 (1997).

[7]T. G. M. Freegarde and G. Hancock, J. de Physique IV **7,** 15 (1997).

[8]V. M. Donnelly, M. V. Malyshev, M. Schabel, A. Kornblit, W. Tai, I. P. Herman, and N. C. M. Fuller, Plasma Sources Sci. Technol. **11,** A26 (2002).

[9]M. V. Malyshev and V. M. Donnelly, Phys. Rev. E **60,** 6016 (1999).

[10]S. Iordanova and I. Koleva, Spectrochim. Acta B **62,** 344 (2007).

[11]J. L. Hueso, A. R. Gonzalez-Flipe, J. Cotrino, and A. Caballero, J. Phys. Chem. A **109,** 4930 (2005).

[12]W. J. Balfour, J. Y. Cao, Prasad, C. V. V., and C. X. W. Qian, J. Chem. Phys. **101,** 10343 (1994).

[13]J. P. Booth, H. Abada, P. Chabert, and D. B. Graves, Plasma Sources Sci. Technol. **14,** 273 (2005).

[14]I. T. Martin and E. R. Fisher, J. Vac. Sci. Technol. A **22,** 2168 (2004).

[15]D. Liu, J. Zhou, and E. R. Fisher, J. Appl. Phys. **101,** 023304 (2007).

[16]J. Luque, W. Juchmann, and J. B. Jeffries, J. Appl. Phys. **82,** 2072 (1997).

[17]J. Zhou and E. R. Fisher, J. Phys. Chem. B **110,** 21911 (2006).

[18]H. Ito, S. Y. Ichimura, K. C. Namiki, and H. Saitoh, Jpn. J. Appl. Phys., Part 1 **42,** 7116 (2003).

[19]Y. Ushirozawa, H. Matsuda, and K. Wagatsuma, Jpn. Soc. Anal. Chem. **53,** 699 (2004).

[20]R. Foest, J. K. Olthoff, R. J. VanBrunt, E. C. Benck, and J. R. Roberts, Phys. Rev. E **54,** 1876 (1996).

[21]G. Hancock, J. P. Sucksmith, and M. J. Toogood, J. Phys. Chem. **94,** 3269 (1990).

[22]G. A. Hebner, P. A. Miller, and J. R. Woodworth, in *Handbook of Advanced Plasma Processing Techniques*, edited by R. J. Shul and S. J. Pearton (Springer-Verlag, Berlin, 2000).

[23]P. A. Miller, G. A. Hebner, and R. L. Jarecki, J. Vac. Sci. Technol. A **16,** 3240 (1998).

[24]J. Amorim, G. Baravian, and J. Jolly, J. Phys. D: Appl. Phys. **33,** R51 (2000).

[25]G. Cunge, J. P. Booth, and J. Derouard, Chem. Phys. Lett. **263,** 645 (1996).

[26]G. Cunge, P. Chabert, and J. P. Booth, J. Appl. Phys. **89,** 7750 (2001).

[27]T. Sakurai, Plasma Sources Sci. Technol. **16,** S101 (2007).

[28]J. Amorim, G. Baravian, and G. Sultan, Appl. Phys. Lett. **68,** 1915 (1998).

[29]J. Bowles, R. McWilliams, and N. Rynn, Phys. Plasmas **1,** 3814 (1994).

[30]C. I. Butoi, M. L. Steen, J. R. D. Peers, and E. R. Fisher, J. Phys. Chem. B **105,** 5957 (2001).

[31]W. M. M. Kessels, P. R. McCurdy, K. L. Williams, G. R. Barker, V. A. Venturo, and E. R. Fisher, J. Phys. Chem. B **106,** 2680 (2002).

[32]P. R. McCurdy, V. A. Venturo, and E. R. Fisher, Chem. Phys. Lett. **274,** 120 (1997).
[33]P. R. McCurdy, K. H. A. Bogart, N. F. Dalleska, and E. R. Fisher, Rev. Sci. Instrum. **68,** 1684 (1997).
[34]I. T. Martin, J. Zhou, and E. R. Fisher, J. Appl. Phys. **100,** 013301 (2006).
[35]K. L. Williams and E. R. Fisher, J. Vac. Sci. Technol. A **21,** 1688 (2003).
[36]K. L. Williams, I. T. Martin, and E. R. Fisher, J. Am. Soc. Mass. Spectrom. **13,** 518 (2002).
[37]D. Liu, I. T. Martin, and E. R. Fisher, Chem. Phys. Lett. **430,** 113 (2006).
[38]J. Zhang, K. L. Williams, and E. R. Fisher, J. Phys. Chem. A **107,** 593 (2003).
[39]K. H. A. Bogart, J. P. Cushing, and E. R. Fisher, J. Phys. Chem. B **101,** 10016 (1997).
[40]G. Berden, R. Peeters, and G. Meijer, Internat. Rev. Phys. Chem. **19,** 565 (2000).
[41]J. P. Booth, G. Cunge, L. Biennier, D. Romanini, and A. Kachanov, Chem. Phys. Lett. **317,** 631 (2000).
[42]W. M. M. Kessels, J. P. M. Hoefnagels, M. G. H. Boogaarts, D. C. Schram, and M. C. M. van de Sanden, J. Appl. Phys. **89,** 2065 (2001).
[43]J. P. M. Hoefnagels, Y. Barrell, W. M. M. Kessels, and M. C. M. van de Sanden, J. Appl. Phys. **96,** 4094 (2004).
[44]J. P. M. Hoefnagels, A. A. E. Stevens, M. G. H. Boogaarts, W. M. M. Kessels, and M. C. M. van de Sanden, Chem. Phys. Lett. **360,** 189 (2002).
[45]A. P. Yalin, R. N. Zare, C. O. Laux, and C. H. Kruger, Appl. Phys. Lett. **81,** 1408 (2002).
[46]R. Piejak, V. Godyak, and B. Alexandrovich, Rev. Sci. Instrum. **72,** 4002 (2001).
[47]M. Tuszewski and J. A. Tobin, Plasma Sources Sci. Technol. **5,** 640 (1996).
[48]M. F. A. M. van Hest, A. de Graaf, M. C. M. van de Sanden, and D. C. Schram, Plasma Sources Sci. Technol. **9,** 615 (2000).
[49]S. Karecki, R. Chatterjee, L. Pruette, R. Reif, V. Vartanian, T. Sparks, and L. Beu, J. Vac. Sci. Technol. B **19,** 1306 (2001).
[50]M. Schmidt, R. Foest, and R. Basner, Low Temp. Plasma Phys. **199,** 199 (2001).
[51]C. R. Eddy, Jr., in *Handbook of Advanced Plasma Processing Techniques*, edited by R. J. Shul and S. J. Pearton (Springer-Verlag, Berlin, 2000).
[52]H. Singh, J. W. Coburn, and D. B. Graves, J. Vac. Sci. Technol. A **17,** 2447 (1999).
[53]S. Agarwal, G. W. W. Quax, M. C. M. van de Sanden, D. Maroudas, and E. S. Aydil, J. Vac. Sci. Technol. A **22,** 71 (2004).
[54]J. Benedikt, S. Agarwal, D. Eijkman, W. Vandamme, M. Creatore, and M. C. M. van de Sanden, J. Vac. Sci. Technol. A **23,** 1400 (2005).
[55]J. Janes, U. Banzinger, C. Huth, P. Hoffmann, G. Neumann, and H.-C. CScheer, Rev. Sci. Instrum. **63,** 48 (1992).
[56]J. A. Ferreira and F. L. Tabares, J. Vac. Sci. Technol. A **25,** 246 (2007).
[57]F. J. Lopez-Garzon, M. Domingo-Garcia, M. Perez-Mendoza, P. M. Alvarez, and V. Gomez-Serrano, Langmuir **19,** 2838 (2003).
[58]H. Motomura, S. Imai, and K. Tachibana, Thin Solid Films **390,** 134 (2001).
[59]T. Shirafuji, H. Motomura, and K. Tachibana, J. Phys. D: Appl. Phys. **37,** R49 (2004).
[60]L. Schneider and W. Peukert, Particle Particle Sys. Charact. **23,** 351 (2007).
[61]G. J. Simpson, Appl. Spectrosc. **55,** 16A (2001).
[62]W. M. M. Kessels, J. J. H. Gielis, I. M. P. Aarts, C. M. Leewis, and M. C. M. van de Sanden, Appl. Phys. Lett. **85,** 4049 (2004).

[63]I. M. P. Aarts, J. J. H. Gielis, M. C. M. van de Sanden, and W. M. M. Kessels, Phys. Rev. B: Condens. Matter **73,** 045327 (2006).
[64]J. J. H. Gielis, P. M. Gevers, A. A. E. Stevens, H. C. W. Beijerinck, M. C. M. van de Sanden, and W. M. M. Kessels, Phys. Rev. B: Condens. Matter **74,** 1665311 (2006).
[65]R. K. Laird, E. B. Andrews, and R. F. Barrow, Trans. Faraday Soc. **46,** 803 (1950).
[66]P. Venkateswarlu, Phys. Rev. **77,** 676 (1959).
[67]E. Mathias and G. H. Miller, J. Phys. Chem. **71,** 2671 (1965).
[68]H. F. Winters and J. W. Coburn, Surf. Sci. Rep. **14,** 161 (1992).
[69]J. W. Coburn and H. F. Winters, Ann. Rev. Mater. Sci. **13,** 91 (1983).
[70]J. W. Coburn and H. F. Winters, CRC Crit. Rev. Solid State Mater. Sci. **10,** 119 (1981).
[71]D. B. Graves and D. Humbird, Appl. Surf. Sci. **192,** 72 (2002).
[72]D. Zhang and M. J. Kushner, J. Appl. Phys. **87,** 1060 (2000).
[73]I. T. Martin, B. Dressen, M. Boggs, Y. Liu, C. S. Henry, and E. R. Fisher, Plasma Process. Polym. **4,** 414 (2007).
[74]L. D. B. Kiss, J.-P. Nicolai, W. T. Conner, and H. H. Sawin, J. Appl. Phys. **71,** 3186 (1992).
[75]J. P. Booth, G. Cunge, F. Neuilly, and N. Sadeghi, Plasma Sources Sci. Technol. **7,** 423 (1998).
[76]J. P. Booth, G. Cunge, P. Chabert, and N. Sadeghi, J. Appl. Phys. **85,** 3097 (1999).
[77]H. Singh, J. W. Coburn, and D. B. Graves, J. Vac. Sci. Technol. A **19,** 718 (2001).
[78]Y. Miyoshi, M. Miyauchi, A. Oguni, and T. Makabe, J. Vac. Sci. Technol. A **24,** 1718 (2006).
[79]M. J. Schabel, V. M. Donnelly, A. Kornblit, and W. W. Tai, J. Vac. Sci. Technol. A **20,** 555 (2002).
[80]M. Nagai and M. Hori, Jpn. J. Appl. Phys., Part 1 **46,** 1176 (2007).
[81]K. L. Steffens and M. A. Sobolewski, J. Appl. Phys. **96,** 71 (2004).
[82]G. A. Hebner and P. A. Miller, J. Appl. Phys. **87,** 7660 (2000).
[83]G. Hancock, J. P. Sucksmith, and M. J. Toogood, J. Phys. Chem. **94,** 3269 (1990).
[84]H. Sugai, K. Nakamura, Y. Hikosaka, and M. Nakamura, J. Vac. Sci. Technol. A **13,** 887 (1995).
[85]B. Zhou, E. A. Joseph, S. P. Sant, Y. Liu, A. Radhakrishnan, L. J. Overzet, and M. J. Goeckner, J. Vac. Sci. Technol. A **23,** 1657 (2005).
[86]C. I. Butoi, N. M. Mackie, K. L. Williams, N. E. Capps, and E. R. Fisher, J. Vac. Sci. Technol. A **18,** 2685 (2000).
[87]N. M. Mackie, V. A. Venturo, and E. R. Fisher, J. Phys. Chem. B **101,** 9425 (1997).
[88]G. S. Senesi, E. D. Aloia, R. Gristina, P. Favia, and R. d'Agostino, Surf. Sci. **601,** 1019 (2007).
[89]M. Hori and T. Goto, Appl. Surf. Sci. **253,** 6657 (2007).
[90]J. P. Booth, G. Cunge, P. Chabert, and N. Sadeghi, J. Appl. Phys. **85,** 3097 (1999).
[91]H. Singh, J. W. Coburn, and D. B. Graves, J. Vac. Sci. Technol. A **18,** 2680 (2000).
[92]Y. Hikosaka, H. Toyoda, and H. Sugai, Jpn. J. Appl. Phys., Part 1 **32,** L690 (1993).
[93]N. E. Capps, N. M. Mackie, and E. R. Fisher, J. Appl. Phys. **84,** 4736 (1998).
[94]B. A. Cruden, K. K. Gleason, and H. H. Sawin, J. Appl. Phys. **89,** 915 (2001).
[95]E. R. Fisher, Plasma Process. Polym. **1,** 13 (2004).

[96]J. W. Butterbaugh, D. C. Grey, and H. H. Sawin, J. Vac. Sci. Technol. B **9,** 1461 (1991).
[97]D. C. Gray, H. H. Sawin, and J. W. Butterbaugh, J. Vac. Sci. Technol., A **9,** 779 (1991).
[98]E. R. Fuoco and L. Hanley, J. Appl. Phys. **92,** 37 (2002).
[99]M. B. J. Wijesundara, G. Zajac, E. R. Fuoco, and L. Hanley, J. Adhesion Sci. Technol. **15,** 599 (2001).
[100]A. N. Goyette, Y. Wang, M. Misakian, and J. K. Olthoff, J. Vac. Sci. Technol., A **18,** 2785 (2000).
[101]H. U. Lee, J. P. Deneufville, and S. R. Ovshinsky, J. Non-Crystal. Solids **59-6,** 671 (1983).
[102]N. Mutsukura, M. OOhuchi, S. Satoh, and Y. Machi, Thin Solid Films **109,** 47 (1983).
[103]R. W. Martin and A. J. Merer, Can. J. Phys. **51,** 634 (1973).
[104]J. W. C. Johns and R. F. Barrow, Proc. Phys. Soc. London **71,** 476 (1958).
[105]S. Lee, Y.-C. Tien, and C.-F. Hsu, Plasma Chem. Plasma Process. **19,** 285 (1999).
[106]G. A. Hebner, Appl. Surf. Sci. **192,** 161 (2002).
[107]G. Cunge, P. Chabert, and J. P. Booth, Plasma Sources Sci. Technol. **6,** 349 (1997).
[108]K. P. Giapis and T. K. Minton, Mater. Res. Soc. Symp. Proc. **406,** 33 (1996).
[109]K. P. Giapis, T. A. Moore, and T. K. Minton, J. Vac. Sci. Technol. A **13,** 959 (1995).
[110]K. L. Williams and E. R. Fisher, J. Vac. Sci. Technol. A **21,** 1024 (2003).
[111]K. P. Giapis, T. A. Moore, and T. K. Minton, J. Vac. Sci. Technol., A **13,** 959 (1995).
[112]A. Matsuda, Jpn. J. Appl. Phys., Part 1 **43,** 7909 (2004).
[113]S. Sriraman, E. S. Aydil, and D. Maroudas, J. Appl. Phys. **95,** 1792 (2004).
[114]W. M. M. Kessels, J. P. M. Hoefnagels, P. J. van den Oever, Y. Barrell, and M. C. M. van de Sanden, Surf. Sci. **547,** L865 (2003).
[115]W. M. M. Kessels, D. C. Marra, M. C. M. van de Sanden, and E. S. Aydil, J. Vac. Sci. Technol. A **20,** 781 (2002).
[116]S. Stamou, D. Mataras, and D. Rapakoulias, J. Phys. D: Appl. Phys. **31,** 2513 (1998).
[117]J. Zhou, J. Zhang, and E. R. Fisher, J. Phys. Chem. A **109,** 10521 (2005).
[118]W. M. M. Kessels, M. C. M. van de Sanden, R. J. Severens, and D. C. Schram, J. Appl. Phys. **87,** 3313 (2000).
[119]M. Hertl and J. Jolly, J. Phys. D: Appl. Phys. **33,** 381 (2000).
[120]J. Perrin, M. Shiratani, P. Kae-Nune, H. Videlot, J. Jolly, and J. Guillon, J. Vac. Sci. Technol. A **16,** 278 (1998).
[121]T. Bakos, M. S. Valipa, and D. Maroudas, J. Chem. Phys. **126,** 114704 (2007).
[122]T. Singh, M. S. Valipa, T. J. Mountziaris, and D. Maroudas, Appl. Phys. Lett. **90,** 251915 (2007).
[123]S. Sriraman, S. Ramalingam, E. S. Aydil, and D. Maroudas, Surf. Sci. **459,** L475 (2000).
[124]J. Zhou, I. T. Martin, E. Adams, D. Liu, and E. R. Fisher, Plasma Sources Sci. Technol. **15,** 714 (2006).
[125]A. von Keudell, I. Kim, A. Consoli, M. Schulze, A. Yangua-Gil, and J. Bendikt, Plasma Sources Sci. Technol. **16,** S94 (2007).
[126]M. F. A. M. van Hest, J. R. Haartsen, M. H. M. van Weert, D. C. Schram, and M. C. M. van de Sanden, Plasma Sources Sci. Technol. **12,** 539 (2003).
[127]J. Benedikt, D. C. Schram, and M. C. M. van de Sanden, J. Phys. Chem. A **109,** 10153 (2005).

[128]J. Benedikt, R. V. Woen, S. L. M. van Mensfoort, V. Perina, J. Hong, and M. C. M. van de Sanden, Diamond Rel. Mater. **12,** 90 (2003).
[129]A. von Keudell, T. Schwarz-Selinger, and W. Jacob, J. Appl. Phys. **89,** 2979 (2001).
[130]A. von Keudell, M. Meier, and T. Schwarz-Selinger, Appl. Phys. A **72,** 551 (2001).
[131]H. Sugai and H. Toyoda, J. Vac. Sci. Technol. A **10,** 1193 (1992).
[132]H. Kojima, H. Toyoda, and H. Sugai, Appl. Phys. Lett. **55,** 1292 (1989).
[133]M. H. Loh and M. A. Capelli, Appl. Phys. Lett. **70,** 1052 (1997).
[134]D. Liu and E. R. Fisher, J. Vac. Sci. Technol. A **25,** in press (2007).
[135]H. Tahara, Y. Ando, K. Onoe, and T. Yoshikawa, Vacuum **65,** 311 (2002).
[136]P. J. van den Oever, J. H. van Helden, C. C. H. Lamers, R. Engeln, D. C. Schram, M. C. M. van de Sanden, and W. M. M. Kessels, J. Appl. Phys. **98,** 093301 (2005).
[137]P. R. McCurdy, C. I. Butoi, K. L. Williams, and E. R. Fisher, J. Phys. Chem. B **103,** 6919 (1999).
[138]M. L. Steen, K. R. Kull, and E. R. Fisher, J. Appl. Phys. **92,** 55 (2002).
[139]G. Cicala, G. Bruno, P. Capezzuto, and P. Favia, J. Mater. Res. **11,** 3017 (1996).
[140]M. Creatore, G. Cicala, P. Favia, R. Lamendola, and R. d'Agostino, Mater. Res. Soc. Symp. Proc. **544,** 115 (1999).
[141]G. Cicala, M. Creatore, P. Favia, R. Lamendola, and R. d'Agostino, Appl. Phys. Lett. **75,** 37 (1999).
[142]K. Ishikawa, Y. Yamaoka, M. Nakamura, Y. Yamazaki, S. Yamasaki, Y. Ishikawa, and S. Samukawa, J. Appl. Phys. **99,** 083305 (2006).
[143]D. Liu, I. T. Martin, J. Zhou, and E. R. Fisher, Pure Appl. Chem. **78,** 1187 (2006).

CHAPTER 4

CN SURFACE INTERACTIONS AND TEMPERATURE DEPENDENT FILM GROWTH DURING PLASMA DEPOSITION OF a-CN_x:H FILMS

This chapter contains data from a full paper published in the *Journal of Physical Chemistry C* and written by Joshua M. Stillahn and Ellen R. Fisher. These studies examine global film growth behavior in CH_3CN discharges and discuss the particular contributions of gas phase CN radicals in terms of both their behavior in the gas phase as well as their steady state surface interactions during deposition of a-CN_x:H materials.

4.1 Introduction

Over the last decade, efforts to synthesize the superhard β-C_3N_4 phase of carbon nitride as predicted by Liu and Cohen[1] have been largely unsuccessful.[2,3] An increasing amount of attention, however, has been focused on the properties of amorphous carbon nitride (a-CN_x) materials, with special attention to their tribological, optical, electronic, and chemical properties. These properties have been investigated with respect to their applications in wear-resistant[4-7] and optical[8-10] coatings, field emission devices,[11-14] hydrogen storage,[15-17] and electrochemical systems.[18,19] Various deposition processes, including both physical and chemical vapor deposition (CVD), have been explored to meet the demands of these applications, which generally require smooth, pinhole-free films with good adhesion to the underlying substrate. In plasma-enhanced CVD (PECVD) of a-CN_x:H, focus has been on systems of mixed precursors, often with N_2 or NH_3 acting as the nitrogen source and CH_4, C_2H_2, or C_2H_4 acting as the carbon source. These separate source precursors highlight the important effects of N-content on film properties by allowing direct variation of the feed gas composition.[20,21] They also provide for conjecture on the mechanisms for nitrogen incorporation into the resulting films, which is logically expected to depend on the presence of nitrogen-containing species such as CN*(g)* and NH_x*(g)*. The complexity of mixed precursor systems, however, is increased because several of these nitrogen-containing species may be present simultaneously and in significant numbers. Consequently, the underlying chemical processes are often obscured. Concerted attempts to understand the fundamental gas, surface, and interface chemistry that dominates a-CN_x:H deposition are relatively few,[22-24] and the incorporation of nitrogen remains poorly understood. Here, we have employed CH_3CN

as a single-source precursor to alleviate some of these issues and to help elucidate chemical mechanisms for a-CN_x:H PECVD. It is imperative to examine not only the physical properties of the films, but also the plasma gas phase species and their surface interactions to fully understand the overall deposition process.

We use a multi-pronged approach to examining the plasma chemistry in CH_3CN systems. Specifically, laser-induced fluorescence (LIF) and optical emission spectroscopy (OES) are used as gas phase diagnostic tools to reveal information about the formation, energetics, and density of ground and excited state species, respectively. They thus are crucial to our understanding of the behavior of gas phase species and to our interpretation of the resulting film properties. Characterization of a-CN_x:H films was performed by Fourier-transform infrared (FTIR) spectroscopy, atomic force microscopy (AFM), and profilometry. At the plasma-surface interface, we employ the imaging of radicals interacting with surfaces (IRIS) technique,[25,26] which characterizes gas phase species as well as their surface reactivity during plasma processing of materials. The IRIS method combines plasma and molecular beam technologies with LIF to provide spatially resolved two-dimensional images of radical species during plasma-surface interactions. Here, this technique has been used to measure the surface reactivity of CN radicals under the influence of different plasma conditions and substrate temperatures. These surface reactivity values are then combined with the results of other gas phase and surface analyses to illuminate aspects of the deposition mechanism, including the role of substrate temperature and substrate interactions with CN radicals in CH_3CN plasmas.

4.2 Results

A. Gas phase spectroscopy. Figure 4.1 shows an OES spectrum for a 100% CH_3CN plasma (100 mTorr, 50 W). Significant emission peaks are observed for atomic H and the molecular species CN, H_2, and N_2. Although formation of CH radicals would be expected in this system, previous results from our laboratory have shown that even in CH_4 plasmas, intense signals from CH* emission are not observed with OES.[23] Nonetheless, the CH $B^2\Sigma^- \rightarrow X^2\Pi$ transition overlaps the CN $B^2\Sigma^+ \rightarrow X^2\Sigma^+$ emission peak and may make some contribution to the peak near 388 nm. Expansion of the peak near 337 nm reveals two features, the more intense feature corresponding to emission from the second positive band of N_2 and the other, weaker feature corresponding to the $\tilde{A}^3\Pi \rightarrow \tilde{X}^3\Sigma^-$ transition of NH at 335.88 nm (inset, Figure 4.1).[27] The low emission from NH in this system is likely because creating NH from CH_3CN requires rather extensive bond breakage and formation, decreasing the probability for its formation. No discernable peaks were observed in the regions corresponding to the $\tilde{A}^2A_1 \rightarrow \tilde{X}^2B_1$ rovibronic transition of NH_2 (597 nm)[28] or the $4d^4P \rightarrow 3p^4P^0$ atomic transition of N (674 nm).

Figure 2.5 shows an LIF excitation spectrum for the CN $B^2\Sigma^+ \rightarrow X^2\Sigma^+$ transition collected in 100% CH_3CN plasma (50mTorr, 150W). This spectrum was collected in six separate scans with step sizes of 0.004 nm. Both the R_1 and P_1 branches of the (0,0) vibrational mode are represented. Simulated spectra show that the band head in the P-branch is not apparent at 300 K, and the relatively intense band head in Figure 2.5 is an indication of an elevated Θ_R. Calculated line positions are shown below the spectrum, with high *N*-value peaks excluded for clarity. Figure 4.2 shows an excitation spectrum

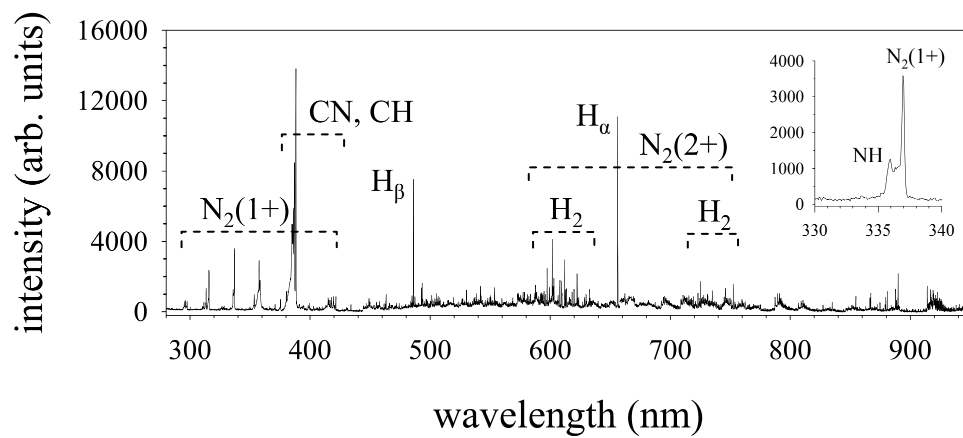

Figure 4.1 Raw OES spectrum 100% CH_3CN plasma (100 mTorr, 50 W) with identities of major emission peaks. Inset shows an expansion of the spectral region from 330 to 340 nm.

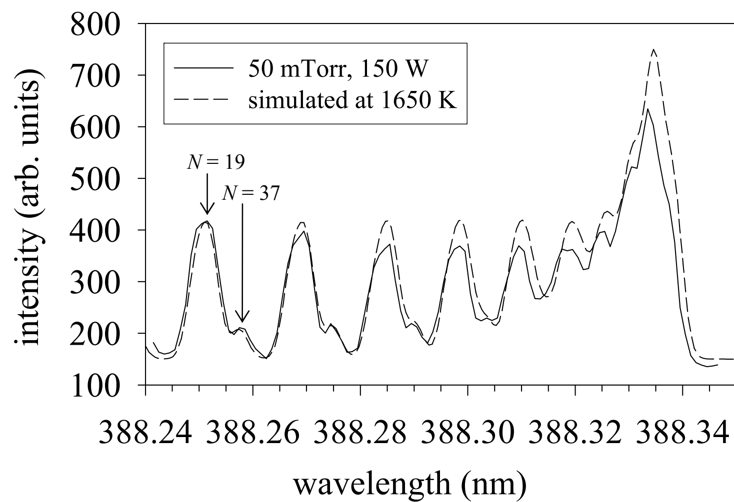

Figure 4.2 LIF excitation spectrum for the CN $X^2\Sigma^+ \rightarrow B^2\Sigma^+$ transition collected in a 100% CH_3CN plasma (50 mTorr, 150 W). The experimental spectrum (solid line) used for determining Θ_R(CN) is superimposed on the simulated spectrum (dashed line). Rotational temperatures were estimated from pairs of adjacent peaks corresponding to N = 19, 37, N = 20, 36, and N = 21, 35.

collected over a smaller spectral region under the same plasma conditions and overlaid with spectral data simulated at 1650 K. In this region of the spectrum, peaks with significantly different *N*-values appear next to each other as a result of the band head in the $P_1(0,0)$ branch. This allows an accurate estimation of the rotational temperature, Θ_R, and the peaks' proximity minimizes any potential effects of drift in laser power. With smaller step sizes of 0.001 nm, spectral line shapes are more clearly distinguished, allowing a more accurate determination of Θ_R. Rotational spectra were collected in this region for different gas compositions, gas pressures, and rf powers. From each spectrum, an average Θ_R was calculated from separate fitting of the *N*-state pairs $N = 19$ and 37, $N = 20$ and 36, and $N = 21$ and 35.

Figure 4.3a shows the variation of Θ_R with gas pressure for rf powers of 50 and 150 W. Over the source pressure range 50–150 mTorr, Θ_R decreases with increasing source gas pressure from about 1800 K to 1300 K, with no strong dependence on rf power. This is also apparent in Figure 4.3b, where Θ_R remains relatively constant for $P =$ 50–150 W, with values of 1300 ± 100 and 1800 ± 100 K at gas pressures of 50 and 150 mTorr, respectively. Adding an inert gas like Ar to the plasma increases the number of nonreactive gas phase collisions and can help distinguish the effects of collision environment and formation mechanisms on Θ_R. In Figure 4.3c, Θ_R is shown as a function of Ar content for CH_3CN/Ar plasmas (150 mTorr, 50 W). For Ar fractions of 40 and 80%, Θ_R values are roughly consistent with values measured in 100% CH_3CN (0% Ar), Figures 4.3a and b.

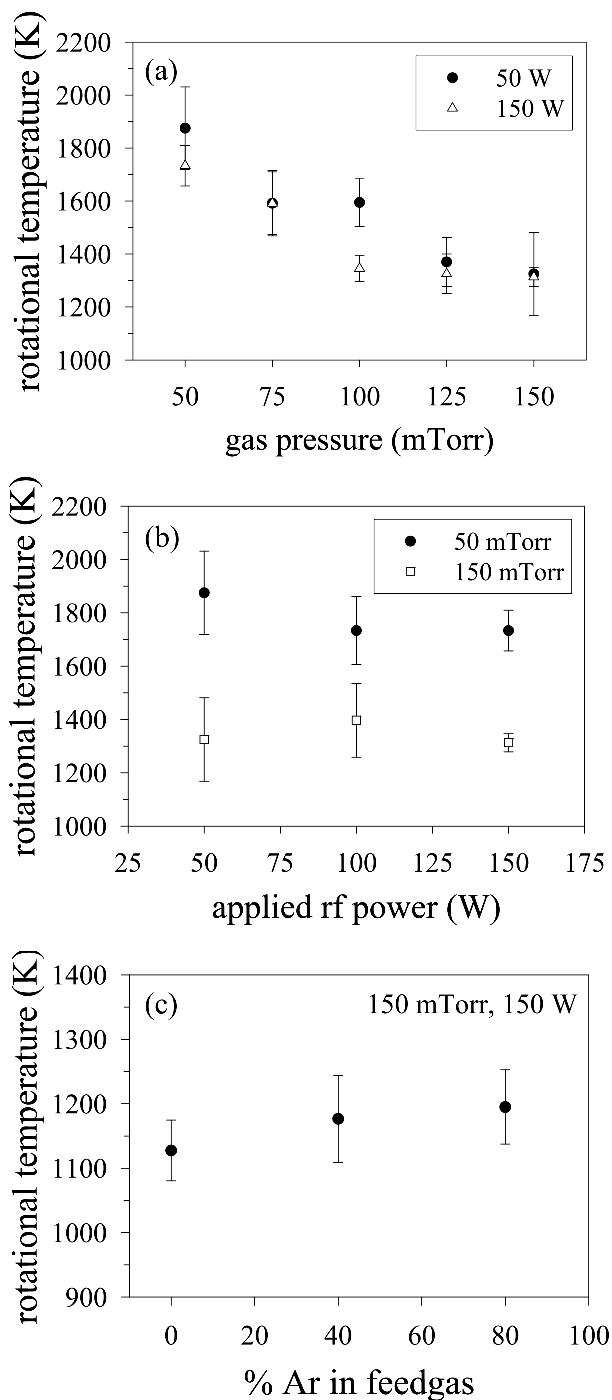

Figure 4.3 Average rotational temperatures, Θ_R, of CN plotted as a function of (a) CH_3CN pressure at 50 and 150 W; (b) rf power in 50 and 150 mTorr of CH_3CN, and (c) Ar fraction (total pressure = 150 mTorr, 150 W). Error bars represent one standard deviation of the mean of several measurements ($n \geq 3$).

The intensity of an individual rotational line is proportional to the gas phase number density of the emitting species. Although the selection of a single line in the excitation spectrum as an indicator of CN number density is somewhat arbitrary, the $P_1(0,0)$, $N = 9$ peak, indicated in Figure 4.1a, was chosen to represent CN density in the plasma as it offers a reasonable signal/noise ratio without significant interference from overlapping peaks. Trends in the CN number density were thus derived from average measurements of the $N = 9$ peak intensity and are shown in Figure 4.4 as a function of both applied rf power, Figure 4.4a, and source gas pressure, Figure 4.4b. Over the range of applied rf powers used here, there is a marked increase in the CN number density at both pressures studied. These data suggest a positive correlation between CN number density and gas pressure in this system, but additional data collected as a function of gas pressure, Figure 4.4b, do not reveal any clear dependence on pressure.

B. Reactivity. Figure 2.5 shows a representative set of LIF images, each representing 5000 laser pulses, collected in a 100% CH_3CN plasma (150 mTorr, 150 W). With the substrate rotated into the path of the molecular beam, Figure 4.5a, the LIF signal is collected from molecules incident on the substrate as well as molecules scattering from the substrate. Under the conditions used in these studies, we estimate the total flux of molecules on the substrate to be $\sim 10^{14}$ molecules $cm^{-2}s^{-1}$. Given that CN generally constitutes <10% of the dissociation products of CH_3CN, we estimate the flux of CN radicals to be $\sim 10^{13}$ molecules $cm^{-2}s^{-1}$ (upper limit). Figure 4.5b shows an LIF image with the substrate rotated out of the path of the molecular beam. With no exposed substrate surface, LIF signal arises only from radicals in the incident molecular beam. The image in Figure 4.5c represents the pixel-by-pixel difference between Figures 4.5a

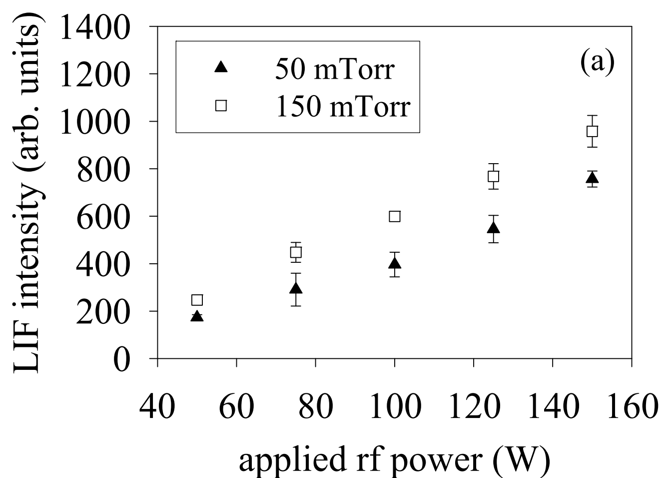

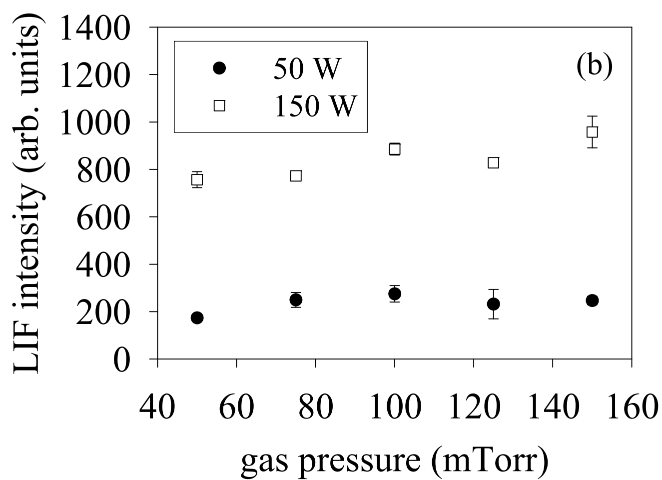

Figure 4.4 Average CN LIF intensity in pure CH_3CN plasma as a function of (a) applied rf power for 50 and 150 mTorr and (b) gas pressure for 50 and 150 W. Error bars represent one standard deviation of the mean.

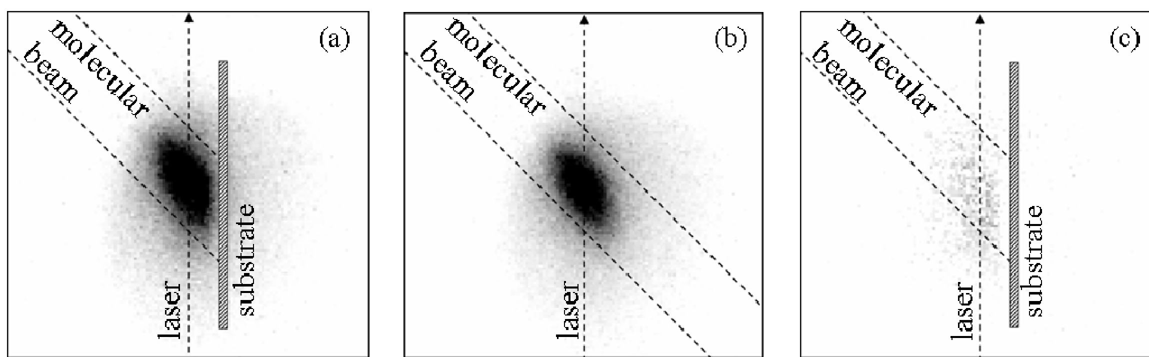

Figure 4.5 Two-dimensional ICCD images of CN LIF emission from radicals in a CH_3CN plasma molecular beam (150 mTorr, 150 W). LIF signal is imaged in (a) with a substrate rotated into the path of the molecular beam at a distance of 3.8 mm from the laser and in (b) with no substrate. Image (c) represents the difference between images (a) and (b) and thus corresponds to the LIF signal generated by radicals scattering from the substrate. Dashed lines indicate the approximate locations of the molecular beam and laser beam.

and 4.5b and thus corresponds to the LIF signal from the molecules scattering from the substrate. By selecting a column of pixels along the laser beam axis and plotting the average LIF intensity in each row, we obtain a one-dimensional cross section of the image. This is shown in Figure 4.6, where cross sections for the incident beam and scattered molecules are calculated from the raw images in Figures 4.5b and 4.5c, respectively. The simulation results for this set of three images, also shown in Figure 4.6, yield S(CN) = 0.15 ± 0.04, corresponding to a surface reactivity of R(CN) = 0.85 ± 0.04.

Figure 4.7a shows the variation of R(CN) with rf power for 50 and 150 mTorr CH_3CN plasmas. Relatively high surface reactivities of ~0.8 are observed at all pressures and powers, indicating that R(CN) does not depend on these parameters to a significant extent. The data collected in 150 mTorr 100% CH_3CN plasmas are plotted again in Figure 4.7b, along with surface reactivites measured in CH_3CN/Ar mixtures. No significant changes are observed in R(CN) values with the introduction of Ar to the plasma, and average values are again ~0.8. R(CN) was also measured (50 mTorr, 50 W, 100% CH_3CN) as a function of T_S as shown in Figure 4.7c. Without actively heating the substrate, T_S is ~ 29 °C, slightly above room temperature. Under these conditions, R(CN) is consistent with values measured under the same conditions where T_S was not actively monitored, Figure 4.7a. No changes in R(CN) are observed at higher T_S, and again, all values are ~0.8. As noted in Section 6.3B, correction of these reactivity data for the effects of rotational temperature leads to higher reactivity values of ~94%. The insensitivity of R(CN) to plasma or substrate conditions has been observed previously for SiH and CH radicals in silane (and disilane) and methane-based systems, respectively,[29,30] and contrasts with results of IRIS studies for surface interactions of

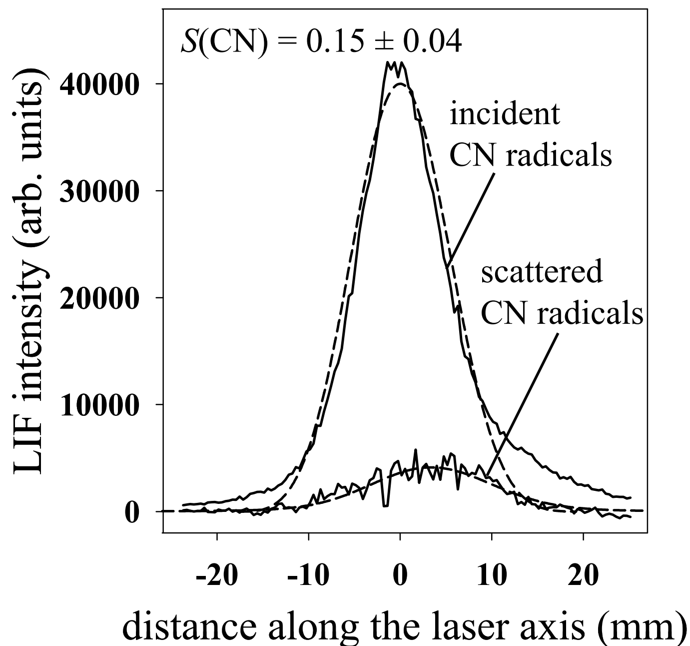

Figure 4.6 Cross sectional data from the CN LIF images shown in Figure 4.5. Intensity cross sections are shown for radicals incident on and scattered from the substrate, corresponding to Figures 4.5b and 4.5c, respectively. Dashed lines represent simulated data fit to the experimental cross-sections (solid lines) with S(CN) = 0.15 ± 0.04. This corresponds to a CN surface reactivity of R(CN) = 0.85 ± 0.04.

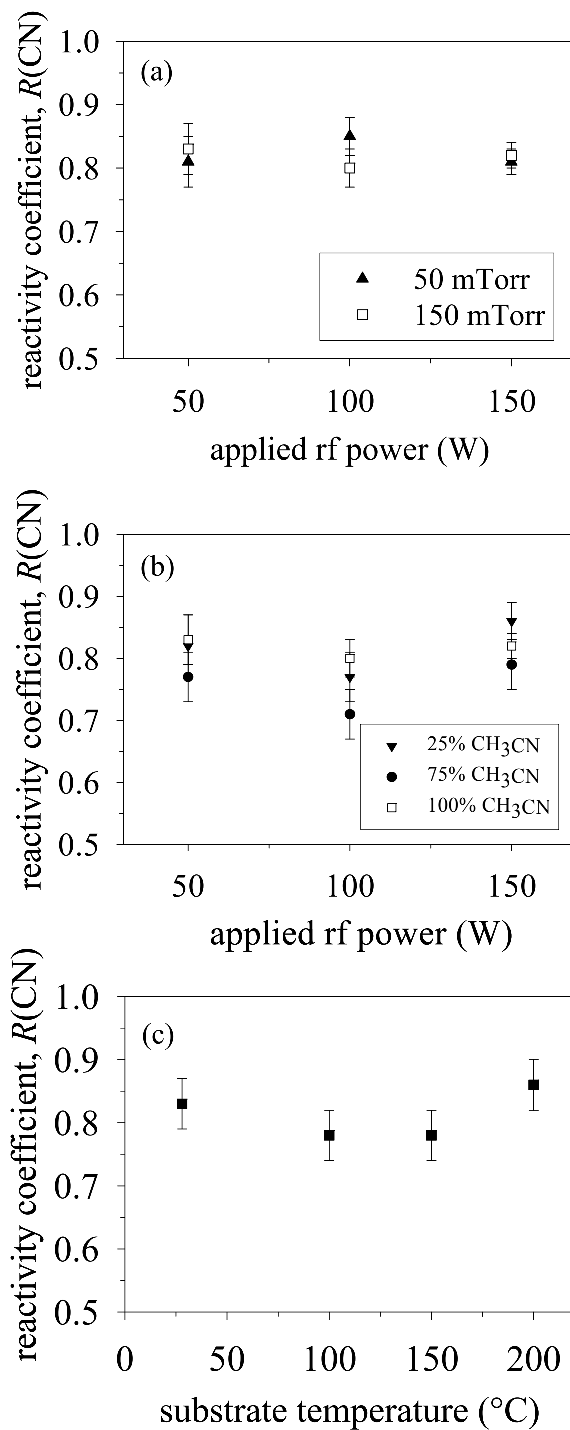

Figure 4.7 Average surface reactivity of CN radicals plotted as a function of (a) applied rf power in 100% CH_3CN plasma at 50 and 150 mTorr, (b) applied rf power in CH_3CN/Ar mixtures (total pressure = 150 mTorr), and (c) substrate temperature (50 mTorr, 50 W).

other molecules (e.g., CF_2[31,32] and OH[25,33]) that appear to be highly dependent on experimental parameters.

C. Deposition Studies. In our film deposition studies, ambient heating of the plasma reactor (likely due to resistive heating of the rf circuit and/or transfer of energy from gas phase species[34]) caused an increase in T_S over the course of the deposition (between 5 and 40 min). This ambient heating is characterized in Figure 4.8a, along with the film thickness, as a function of deposition time. The film thickness measurements were not made in situ, and each point represents a separate set of three depositions. Over a 40 min deposition, T_S increases and then plateaus at ~95 °C. Over the same time period, measured film thicknesses increase steadily, corresponding to a growth rate of 73.4 ± 0.5 nm/min. Connection of the substrate heater leads changed the appearance of the plasma discharge as well as the absolute values of the maximum T_S and the film growth rate, with respective values of ~109 °C and 25 ± 4 nm/min calculated from 10 measurements over the same range of deposition times. These changes may reflect losses in the applied rf power as a result of coupling to the substrate heater apparatus.

The initial substrate temperature ($T_{S,i}$) was also controlled by actively heating the substrate prior to deposition. The resulting changes in film growth rate are characterized in Figure 4.8b for a series of 20 min depositions. Without actively heating the substrate, $T_{S,i}$ = 23.2 ± 0.4 °C and the average growth rate (30 ± 3 nm/min) is within experimental error of the value obtained from the variation of the deposition time. The growth rate decreases by more than a factor of three over the range $T_{S,i}$ = 23-150 °C. At $T_{S,i}$ = 200 °C, deposited films were too thin to allow measurement of film thickness by

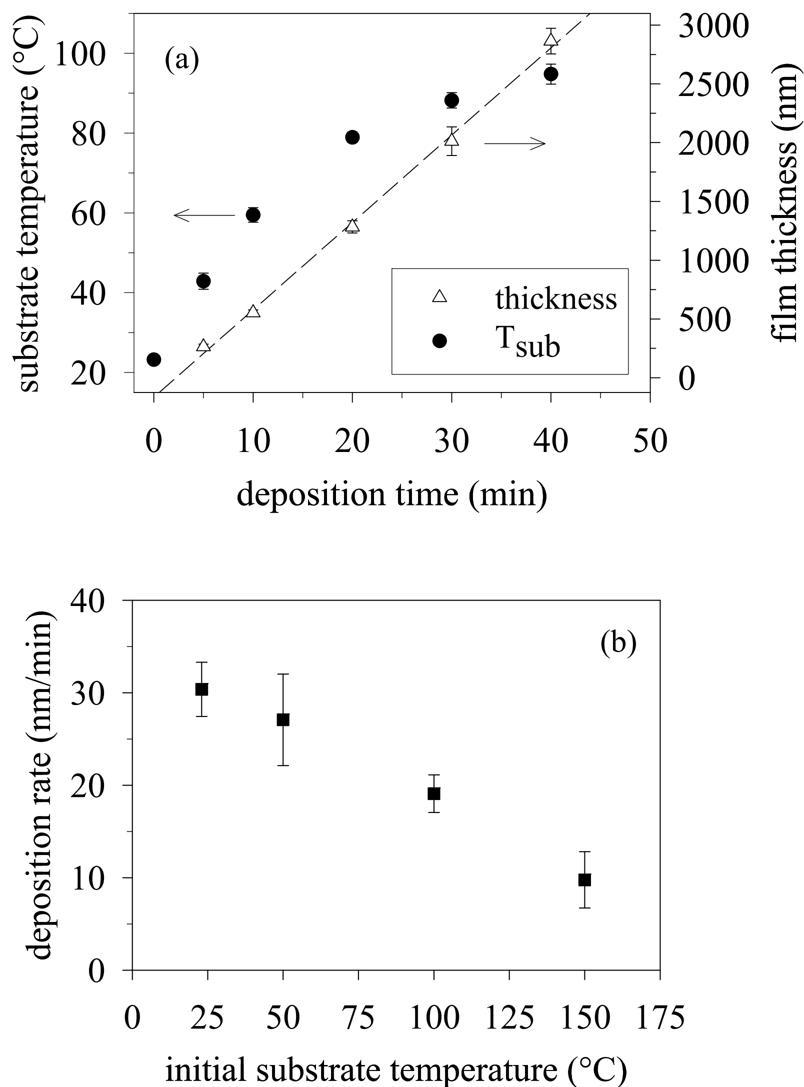

Figure 4.8 Deposition rate measurements made in CH_3CN plasma (100 mTorr, 50 W). In (a), the average film thickness and average substrate temperature are plotted as a function of the deposition time, and the deposition rate is obtained from regression analysis of film thickness data (dashed line). In (b), the average deposition rate is plotted as a function of the initial substrate temperature.

profilometry. Note that, given the change in growth rate with the connection of the substrate heater, we cannot discount the possibility that coupling effects may also contribute to the observed decrease in growth rate as higher voltages are applies to the substrate heater.

Films used for thickness measurements were also analyzed by AFM, XPS, and FTIR to evaluate their morphology and composition. Representative AFM images are shown in Figure 4.9 for films deposited with $T_{S,i}$ = 23 °C and 100 °C. In these images, film grains are resolved and appear to be tens of nm in size at both $T_{S,i}$. Average root-mean-square and peak-to-peak roughness factors (R_{rms} and R_{p-p}, respectively) were calculated from three films deposited at each $T_{S,i}$. At $T_{S,i}$ = 23 °C, R_{rms} and R_{p-p} are 2.8 ± 0.6 and 23 ± 5 nm, respectively; at $T_{S,i}$ = 100 °C, the corresponding values are 2.5 ± 0.2 and 18 ± 1 nm, respectively. Thus, $T_{S,i}$ does not appear to be significantly affecting roughness factors for the deposited a-CN_x:H films. X-ray photoelectron spectroscopy (XPS) data collected for films deposited at $T_{S,i}$ = 23 °C indicate a significant amount of N-content, with a N/C ratio of 0.41 ± 0.02. Some O incorporation is observed as well, yielding O/C = 0.12 ± 0.01, and may be a result of oxidation following the films' exposure to atmosphere.[35] A notable change in N-content is observed at $T_{S,i}$ = 100 °C, as the observed values of N/C and O/C values are 0.34 ± 0.01 and 0.13 ± 0.01, respectively. Temperature dependent loss of N from a-CN_x materials due to heating has been reported by others. In general, these studies suggest that this is due to recombination of N in unstable bonding environments in the material, forming volatile species such as N_2 or NH_3, which then diffuse out of the material through voids in the film structure.[36-40]

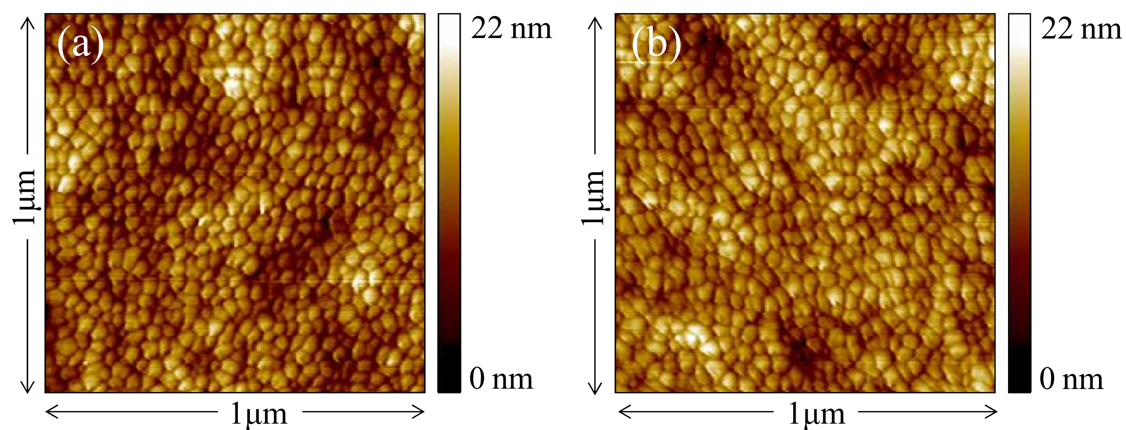

Figure 4.9 Representative AFM images of films deposited in CH_3CN plasma (100 mTorr, 50 W) with (a) $T_{sub,i}$ = 23°C and (b) $T_{sub,i}$ = 100°C.

Figure 4.10 shows a representative transmission FTIR spectrum for a film deposited for 60 min without actively controlling T_S (i.e, allowing ambient heating from the plasma). Major absorption peaks are attributed to CH_x, C=N, and NH_x functional groups. Spectral data from films deposited in this work are consistent with previous studies from our laboratory, which included in-depth FTIR analysis of films deposited under similar conditions.[41]

4.3 Discussion

One of the advantages of PECVD is the ability to activate film precursors in the gas phase, and predictably, the nature of this activation often exerts a strong influence on the nature of the deposited film. Of particular interest are the energetics of those gas phase species which react with high probability at the surface of the growing film. CN radicals exhibit relatively high surface reactivities in the CH_3CN systems studied here, indicative of a contributing role in the deposition process. The origin and gas phase properties of CN are therefore relevant to understanding the overall deposition process in CH_3CN plasmas.

Results of gas phase diagnostics provide direct clues about the formation and behavior of CN radicals in the plasma, and it is useful to begin by considering some possible formation pathways. The most obvious route to formation of CN in a CH_3CN plasma is by simple electron impact dissociation of the C–C bond,

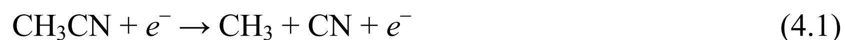

$$CH_3CN + e^- \rightarrow CH_3 + CN + e^- \qquad (4.1)$$

If this process is the primary source of CN, then the CN radical number density, n_{CN}, would be expected to increase with the electron temperature, T_e, which in turn

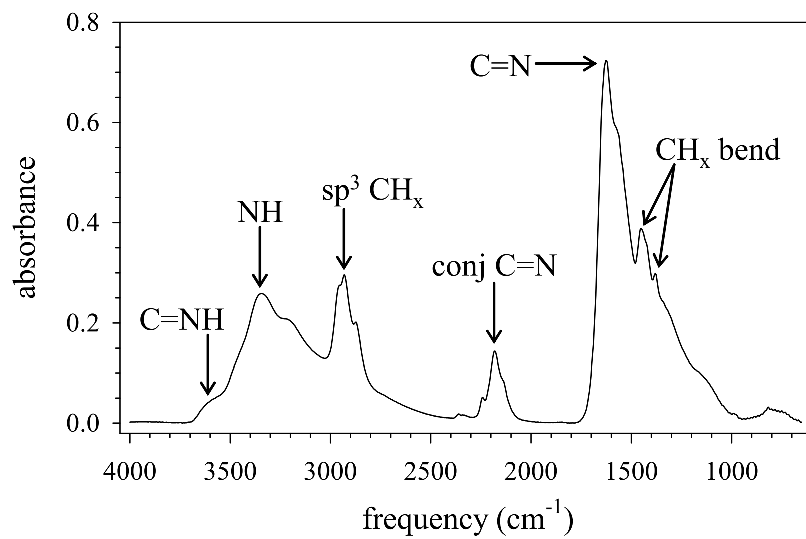

Figure 4.10 Corrected transmission FTIR spectrum of film deposited for one hour on a KBr substrate positioned in the coil region of a 100 mTorr, 50 W CH_3CN plasma.

increases with *P*. Comparison of the ΔH_f for Reaction 4.1 to typical T_e measured in our systems (~5.2 eV and ~5-7 eV,[42] respectively) suggests that Reaction 4.1 is feasible. Figure 4.4a shows that the CN LIF signal does increase nearly linearly with rf power, indicating that Reaction 4.1 is the most likely pathway for the formation of CN. This result is in sharp contrast to the results of Li et al., who observe a decrease in the density of ground-state CN with increasing discharge current. However, their experiments were performed at higher powers than those used in this study. It may also be possible to form CN by inelastic collisions in the gas phase,

$$CH_3CN + M \rightarrow CH_3 + CN + M \qquad (4.2)$$

where M represents a gas phase collision partner. Here, a direct dependence of number density of CN radicals on gas pressure would be expected. This type of dependence, however, is not observed in the CN LIF signal measured as a function of gas pressure, Figure 4.4b, indicating that Reaction 4.2 is not a major source of CN. Finally, it may be possible to generate atomic nitrogen and carbon by dissociation of Reaction 4.1 products and subsequently form CN through recombination processes,

$$C + N \rightarrow CN \qquad (4.3)$$

Mass spectrometric studies of alkyl cyanides suggest that formation of atomic N directly from CH_3CN is not favored,[43-47] and in this work, the steady increase in CN LIF signal, Figure 4.4a, suggests that CN is not lost to fragmentation under the experimental conditions, as has been observed in our laboratory for other diatomic radicals.[29,30] Studies on $CH_3CN \leftrightarrow CH_2CNH$ isomerization[44,47] allude to other pathways to form atomic C and N, Process 4.4,

$$CH_2CNH \rightarrow C_2H_2 + NH \qquad (4.4a)$$

$$CH_2 \rightarrow 2C + 2H \quad (4.4b)$$

$$NH \rightarrow N + H \quad (4.4c)$$

but OES spectra suggest that this is not the case, as no emission is observed from either NH_2 or atomic N, and NH emission is weak. Li and coworkers report significant NH emission in CH_3CN plasmas;[48] as noted above, however, they employed higher powers and would therefore expect generation of NH_x species to a larger extent. In this study, we observe a significant amount of emission from N_2, but given the relative scarcity of other N-containing species, we attribute at least some of this signal to contamination by atmospheric N_2. Thus, Reaction 4.3 does not appear to contribute significantly to the formation of CN radicals in this system.

Given the power-dependent increase in the CN LIF signal, a maximum would be expected in the reactivity of CN radicals if either (a) surface reactive sites are at a premium and/or (b) CN radicals are particularly selective in choosing a surface site for reaction. Based on the constancy of R(CN) in Figure 4.7a, it is therefore reasonable to speculate that CN radicals are not wanting for suitable reactive sites under these conditions.

Additional information can be gleaned from trends in Θ_R. Given the magnitude of Θ_R in this system, it is likely that Reaction 4.1 imparts significant rotational energy to CN radicals and occurs in such a way that limits thermalization of rotational degrees of freedom. Furthermore, the lack of any power-dependence in these data, Figures 4.3a and b, suggests that Θ_R is characteristic not of T_e but of the dissociation process itself. These ideas are explored in greater detail in Chapter 6. Relaxation of rotational degrees of freedom (i.e., rotational cooling) takes place predominately through nonreactive

collisions.[49] Evidence for this type of collisional cooling is seen in Figure 4.3, where Θ_R decreases as a function of gas pressure (also see Figure 6.1 for data from a variety of different precursors). Interestingly, this trend is not reflected in the pressure-dependence of *R*(CN), indicating that in this Θ_R regime, rotational energy does not influence the surface reaction of CN radicals.

Another way to examine the energetic effects of collisions is to introduce an inert gas such as Ar to the plasma feed. Presumably, the fraction of nonreactive collisions will be greater with an inert gas dilution than in an identical pressure of the precursor gas alone, increasing the likelihood of Θ_R thermalization. Figure 4.3c shows, however, that Θ_R is unaffected by increases in Ar content at 150 mTorr, suggesting that the observed decrease in Θ_R, Figure 4.3a, results from collision frequency rather than the nature of the collisions themselves. It follows that a large majority of the collisions experienced by CN radicals in these systems are nonreactive. Interestingly, this insensitivity to Ar content does not appear to hold for all CN-containing precursors, as discussed in Chapter 6.

Changes in the feedgas content are also expected to change the flux of gas phase species at the surface. Figure 4.7b shows that increases in Ar content do not increase the amount of CN generated at the surface of the substrate, as might be expected if the surface was being heavily sputtered. Thus, the contribution of sputtered CN to the observed LIF signal can be largely dismissed.

Aside from the energetic properties of gas phase CN radicals, it is reasonable to expect that surface reactivities might also be influenced by the energetic properties of the substrate. In this work, however, the insensitivity of *R*(CN) to T_S refutes this notion.

Rather, these data provide some general information about the relative rate of CN surface reactions. That is, incident CN radicals react, through either surface incorporation or chemical changes, on a time scale that is shorter than their residence time on the surface. Additional measurements at higher T_S may be useful in exploring this competition between surface reaction and desorption.

Taken together, the CN data presented here are consistent with previous results from our lab obtained in mixed precursor systems such as CH_4/N_2.[22,23] Collectively, the results portray a diatomic radical that undergoes surface reaction with a relatively high probability and whose behavior, both in the gas phase and at the surface, is fairly robust with respect to changes in rf power, pressure, gas composition, and T_S.

Based on our surface reactivity measurements, it is likely that CN plays a role in the overall a-CN_x deposition process. Although our IRIS measurements do not distinguish between CN radicals that are incorporated into the film and those that desorb in a chemically-modified form, the prevalence of N-containing functional groups in FTIR spectra, Figure 4.10, begs the question of whether N-content in the deposited films can be attributed to the incorporation of CN radicals. OES spectra suggest that CN is the dominant N-containing species in the plasma. In the absence of strong emission from atomic N, the most likely alternative appears to be N_2. However, the relatively low surface reactivity of N_2[50-53] suggests that it does not contribute significantly to the nitrogen content of the deposited films.

The interaction and relative contributions of CN and the multitude of other species present in these plasmas is very complex; thus, it is useful to consider the global deposition behavior of the system for further insight to the overall deposition process.

From the linear increase in film thickness with deposition time, Figure 4.8a, it is apparent that under steady-state conditions, the film growth rate is not sensitive to increases in T_S. This suggests that up to T_S = 100 °C (and perhaps higher), the rate of steady-state film growth is controlled only by the flux of gas phase precursors to the surface (i.e., mass-transport limited growth). Note that, although the list of species responsible for the trend in Figure 4.8a probably includes a variety of precursors, this insensitivity to T_S is consistent with IRIS measurements of CN steady-state surface reactivity in this study. A markedly different trend is observed when $T_{S,i}$ is varied. As Figure 4.8b shows, the overall growth rate drops considerably with increases in $T_{S,i}$, even over the range of temperatures covered in Figure 4.8a. Similar trends have been observed in the temperature-dependence of a-CN_x and a-CH_x deposition.[54,55] In general, a negative correlation between growth rate and T_S indicates that the surface residence time of film precursors is the dominant factor in film growth.[55,56] In light of the results shown in Figure 4.8a, however, these results can be interpreted more specifically to pertain to film nucleation.

Nucleation is a complex process, even in the simplest case, and is made even more so when accounting for the unique characteristics of PECVD. Generally speaking, the nucleation rate is determined by the growth of monomer clusters, through either diffusion addition or vapor impingement, to form nuclei of a critical size. Among other factors, the rate of diffusion addition will depend on the surface coverage, θ, and mobility of adsorbed monomers, both of which are related to the T_S through the Arrhenius equation.[55-57] At high enough substrate temperatures, the energy of adsorbed monomers facilitates not only monomer diffusion but monomer desorption as well. This reduces the

surface coverage and, therefore, the film nucleation rate. In the CH_3CN deposition system, this decrease in the nucleation rate is manifested as a decrease in the overall film growth rate. These changes in nucleation behavior are not apparent in the film morphology, as there are no statistically significant differences in the roughness factors for films deposited at $T_{S,i}$ = 23 and 100 °C, and film grains shown in Figure 4.9 appear to be very similar in size, suggesting that once steady-state conditions have been reached, film growth proceeds in a very similar manner regardless of the substrate temperature.

If film growth rates in our system were limited only by monomer desorption, they would decay exponentially with increasing $T_{S,i}$ in a typical Arrhenius fashion. The near-linearity of the data in Figure 4.8b, however, suggests that this is not the case. Interestingly, non-Arrhenius behavior has been observed in bimolecular gas phase reactions of CN with both H_2 and O_2 (see the review article by Smith[58] and references therein). Smith proposed that the curvature in the Arrhenius dependence of these data is a result of steric effects, which introduce additional degrees of freedom in the respective transition state complexes for these reactions. Although these results are not directly relevant to the consideration of film nucleation rates, it is possible that the surface interactions of dominant film precursors in this system are sensitive to their orientation on the substrate as a result of steric effects. Alternatively, one might reasonably suggest that the trend in Figure 4.8b does not reflect the kinetic behavior of a single precursor species but instead represents a convolution of many species' behaviors and interactions at the surface. In this case, the complexity of the nucleation mechanism would preclude its explanation with simple kinetic arguments.

4.4 Summary

The work presented here encompassed both substrate temperature-dependent film growth studies and gas-phase characterization of CN radicals during a-CN_x:H film deposition. Temperature-dependent film growth rate studies suggest that higher substrate temperatures cause a decrease in the rate of film nucleation but do not affect the steady-state growth of these films. The gas phase behavior of CN was characterized in CH_3CN plasmas as a function of several different processing parameters. Electron impact dissociation is indicated as the primary CN formation pathway, resulting in the generation of rotationally energetic CN radicals. Surface interaction studies using the IRIS technique, measured the surface reactivity of CN, revealing a high surface reactivity of ~0.8, which was insensitive to a variety of parameters, including applied rf power, gas pressure, Ar dilution, and substrate temperature. These results suggest that the CN radical contributes to the deposition of a-CN_x:H films. Furthermore, the scarcity of other nitrogen containing gas phase species observed with OES suggests the CN radical is a significant source of nitrogen in the deposited films. Overall, the observation that CN reacts with high probability at the surface of depositing a-CN_x:H films is consistent with previous results from our laboratory for other group IV singlet diatomic species such as CH and SiH.

4.5 References

[1]A. Y. Liu and M. L. Cohen, Science **245,** 841 (1989).
[2]G. Goglio, D. Foy, and G. Demazeau, Mat. Sci. Eng. R **58,** 195 (2008).
[3]S. Muhl and J. M. Mendez, Diamond Relat. Mater. **8,** 1809 (1999).
[4]E. C. Cutiongco, D. Li, and Y.-W. Chung, J. Tribol. **118,** 543 (1996).
[5]T.-A. Yeh, C.-L. Lin, J. M. Sivertsen, and J. H. Judy, IEEE Trans. Magn. **27,** 5163 (1991).
[6]E. Broitman, W. Macdonald, N. Hellgren, G. Radnoczi, Z. Czigany, A. Wennerberg, M. Jacobsson, and L. Hultman, Diamond Relat. Mater. **9,** 1984 (2000).
[7]F. Z. Cui, X. L. Qing, and J. Zhao, Surf. Coat. Technol. **200,** 1009 (2005).
[8]S. Metin, J. H. Kaufman, D. D. Saperstein, J. C. Scott, J. Heyman, and E. E. Haller, J. Mater. Res. **9,** 396 (1994).
[9]D. C. Cameron, Surf. Coat. Technol. **169-170,** 245 (2003).
[10]P. R. Vinod, A. Nakamura-Itakura, M. Kitajima, and T. Terai, Jpn. J. Appl. Phys. **42,** 7057 (2003).
[11]C. Godet, J. P. Kleider, and A. S. Gudovskikh, Phys. Status Solidi B **244,** 2081 (2007).
[12]A. Zhong, G. I. Lee, C. B. Mo, S. H. Hong, and J. K. Kang, Chem. Mater. **19,** 2918 (2007).
[13]G. A. J. Amaratunga and S. R. P. Silva, Appl. Phys. Lett. **68,** 2529 (1996).
[14]J. Chen, N. Y. Huang, X. W. Liu, S. Z. Deng, and N. S. Xu, J. Vac. Sci. Technol., B **21,** 567 (2003).
[15]X. D. Bai, D. Zhong, G. Y. Zhang, C. Ma, S. Liu, E. G. Wang, Y. Chen, and D. Shaw, Appl. Phys. Lett. **79,** 1552 (2001).
[16]S. Y. Kim, H. S. Kim, S. Augustine, and J. K. Kang, Appl. Phys. Lett. **89,** 253119 (2006).
[17]Z. H. Zhu, H. Hatori, S. B. Wang, and G. Q. Lu, J. Phys. Chem. B **109,** 16744 (2005).
[18]H. Cachet, C. Debiemme-Chouvy, C. Deslouis, A. Lagrini, and V. Vivier, Surf. Interface Anal. **38,** 719 (2006).
[19]P. Tamiasso-Martinhon, H. Cachet, C. Debiemme-Chouvy, and C. Desluois, Electrochim. Acta **53,** 5752 (2008).
[20]J. Freire, F.L. and D. F. Franceschini, Thin Solid Films **293,** 236 (1997).
[21]C. Wang, S. Yang, and J. Zhang, J. Non-Cryst. Solids **354,** 1608 (2008).
[22]D. Liu and E. R. Fisher, J. Vac. Sci. Technol., A **25,** 368 (2007).
[23]D. Liu, J. Zhou, and E. R. Fisher, J. Appl. Phys. **101,** 023304 (2007).
[24]L. R. Shaginyan, F. Fendrych, L. Jastrabik, L. Soukup, V. Y. Kulikovsky, and J. Musil, Surf. Coat. Technol. **116-119,** 65 (1999).
[25]K. H. A. Bogart, J. P. Cushing, and E. R. Fisher, J. Phys. Chem. B **101,** 10016 (1997).
[26]P. R. McCurdy, K. H. Bogart, N. F. Dalleska, and E. R. Fisher, Rev. Sci. Instrum. **68,** 1684 (1997).
[27]G. Herzberg, *Molecular Spectra and Molecular Structure I. Spectra of Diatomic Molecules*, 2nd ed. (Van Nostrand Reinhold Company, Inc., New York, 1950).
[28]K. Dressler and D. A. Ramsay, Philos. Trans. R. Soc. London, A **251,** 553 (1959).
[29]W. M. M. Kessels, P. R. McCurdy, K. L. Williams, G. R. Barker, V. A. Venturo, and E. R. Fisher, J. Phys. Chem. B **106,** 2680 (2002).
[30]J. Zhou and E. R. Fisher, J. Phys. Chem. B **110,** 21911 (2006).

[31]D. Liu, I. T. Martin, and E. R. Fisher, Chem. Phys. Lett. **430,** 113 (2006).
[32]I. T. Martin and E. R. Fisher, J. Vac. Sci. Technol., A **22,** 2168 (2004).
[33]M. L. Steen, C. I. Butoi, and E. R. Fisher, Langmuir **17,** 8156 (2001).
[34]H. Kersten, H. Deutsch, H. Steffen, G. M. W. Kroesen, and R. Hippler, Vacuum **63,** 385 (2001).
[35]F. Truica-Marasescu, P. Jedrzejowski, and M. R. Wertheimer, Plasma Process. Polym. **1,** 153 (2004).
[36]I. Jimenez, W. M. Tong, D. K. Shuh, B. C. Holloway, M. A. Kelly, P. Pianetta, L. J. Terminello, and F. J. Himpsel, Appl. Phys. Lett. **74,** 2620 (1999).
[37]G. Soto, E. C. Samano, R. Machorro, M. H. Farias, and L. Cota-Araiza, Appl. Surf. Sci. **183,** 246 (2001).
[38]G.-Q. Yu, S.-H. Lee, and J.-J. Lee, Diamond Relat. Mater. **11,** 1633 (2002).
[39]Z. Wang, C. Wang, and J. Zhang, J. Appl. Phys. **104,** 073306 (2008).
[40]D. G. McCulloch and A. R. Merchant, Thin Solid Films **290-291,** 99 (1996).
[41]A. E. Lefohn, N. M. Mackie, and E. R. Fisher, Plasmas Polym. **3,** 197 (1998).
[42]J. Zhou, I. T. Martin, R. Ayers, E. Adams, D. Liu, and E. R. Fisher, Plasma Sources Sci. Technol. **15,** 714 (2006).
[43]W. Heerma, J. J. de Ridder, and G. Dijkstra, Org. Mass Spectrom. **2,** 1103 (1969).
[44]J. C. Choe, Int. J. Mass Spectrom. **235,** 15 (2004).
[45]J. L. Holmes and P. M. Mayer, J. Phys. Chem. **99,** 1366 (1995).
[46]C.-K. Huang, I.-F. Lin, and S.-Y. Chian, Chem. Phys. Lett. **440,** 51 (2007).
[47]X. Yang, S. Maeda, and K. Ohno, J. Phys. Chem. A **109,** 7319 (2005).
[48]P. Li and W. Y. Fan, J. Appl. Phys. **93,** 9497 (2003).
[49]A. Fridman and L. A. Kennedy, *Plasma Physics and Engineering* (Taylor & Francis Books, Inc., New York, 2004).
[50]L. Diekhoner, H. Mortensen, A. Baurichter, J. E., V. V. Petrunin, and A. C. Luntz, J. Chem. Phys. **115,** 9028 (2001).
[51]R. C. Egeberg, J. H. Larsen, and I. Chorkendorff, Phys. Chem. Chem. Phys. **3,** 2007 (2001).
[52]D. C. Papageorgopoulos, B. Berenbak, M. Verwoest, B. Riedmuller, S. Stolte, and A. W. Kleyn, Chem. Phys. Lett. **305,** 401 (1999).
[53]H. Shi, K. Jacobi, and G. Ertl, J. Chem. Phys. **99,** 9248 (1993).
[54]M. Aono, H. Akiyoshi, S. Kikuchi, N. Kitazawa, and Y. Watanabe, J. Vac. Sci. Technol., A **26,** 966 (2008).
[55]H. Kersten and G. M. W. Kroesen, J. Vac. Sci. Technol., A **8,** 38 (1990).
[56]J. P. Hirth and K. L. Moazed, in *Physics of Thin Films*; *Vol. 4*, edited by G. Hass and R. E. Thun (Academic Press, New York, 1967), p. 97.
[57]J. A. Venables, J. Vac. Sci. Technol., B **4,** 870 (1986).
[58]I. W. M. Smith, Chem. Soc. Rev. **37,** 812 (2008).

CHAPTER 5

ION BOMBARDMENT ENERGIES IN CH_3CN PLASMAS AND THEIR INFLUENCE ON a-CN_x FILM DEPOSITION

This chapter presents data on the use of mass spectrometry to characterize both the identity of gas phase ionic species in CH_3CN discharges as well as the energy with which they bombard surfaces during PE-CVD processing. These measurements are accompanied by deposition studies aimed at understanding whether ambient ion bombardment in CH_3CN discharges has a significant effect on the growth of a-CN_x:H films.

5.1 Introduction

Nitrogenated carbon materials have generated much interest for their mechanical properties, particularly following the 1989 theoretical work of Liu and Cohen,[1] which predicted the β-C_3N_4 phase of carbon nitride to have a bulk modulus higher than that of diamond. Since the publication of those results, much effort has been invested in attempts to synthesize the β-C_3N_4 phase.[2,3] Although there have been isolated and inconclusive reports of success in this effort, a convincing synthesis continues to elude researchers. Some residual interest has developed, however, in the properties of related materials such as amorphous hydrogenated carbon nitride (a-CN_x:H), which, in some cases, exhibit properties useful in wear-resistance,[4-7] optical coatings,[8,9] hydrogen storage materials,[10-12] and electrochemical overlayers.[13-17]

Plasma-enhanced chemical vapor deposition (PECVD) provides one convenient means of depositing a-CN_x:H materials, as it allows reasonable film growth rates with excellent surface coverage and can be carried out at relatively low substrate temperatures, minimizing the loss of N-content from the material that has been shown to accompany high temperature processing.[18-22] Another unique aspect of PECVD is the relative abundance of ions in plasma discharges relative to other types of CVD systems. These ions bombard exposed surfaces during processing and have been shown, in our lab and in the work of others, to make substantial contributions to the process chemistry.[23-26] An understanding of the role of ion bombardment is therefore important in understanding the global behavior of a PECVD system. Several different methods have been developed for studying the behavior of bombarding ions in plasma discharges, including mass spectrometry and electrostatic energy analyzers among others.[27-35] A detailed discussion

of the merits and limitations of each of these techniques is beyond the scope of this work; in all cases, however, an effort must be made to minimize electrostatic perturbations of the discharge to extract meaningful information.

With respect to PECVD, probe studies are often accompanied by deposition and surface characterization work with the aim of directly correlating ion behavior to changes in film growth. The application of a negative bias potential finds frequent use in such studies as it serves to accelerate positively charged ions into the substrate and amplifies their effect on the growth process. In the case of a-CN_x:H deposition, this approach has revealed changes in film composition and morphology in the presence of heavy ion bombardment.[26,36-39] Few reports have been published, however, that attempt to characterize the effects of ambient ion bombardment - that is, ion bombardment that occurs in the absence of a substrate bias - on the deposition of a-CN_x:H materials.

In this work, gas phase characterization of positive ionic species is carried out using mass spectrometry and is accompanied by film deposition studies in which a positive DC bias is applied to the substrate. With a positive bias potential of sufficient magnitude, positive ions are repelled from, rather than accelerated toward, the surface. The information gained from these studies is intended to contribute to the collective understanding of surface properties during a-CN_x:H growth.

5.2 Results

Figure 5.1 shows a mass spectrum for a 100% CH_3CN plasma (50 mTorr, 50 W). In this spectrum, the ionization source in the mass spectrometer is turned off, and the signal arises solely from ions that are generated in the plasma discharge. The parent ion

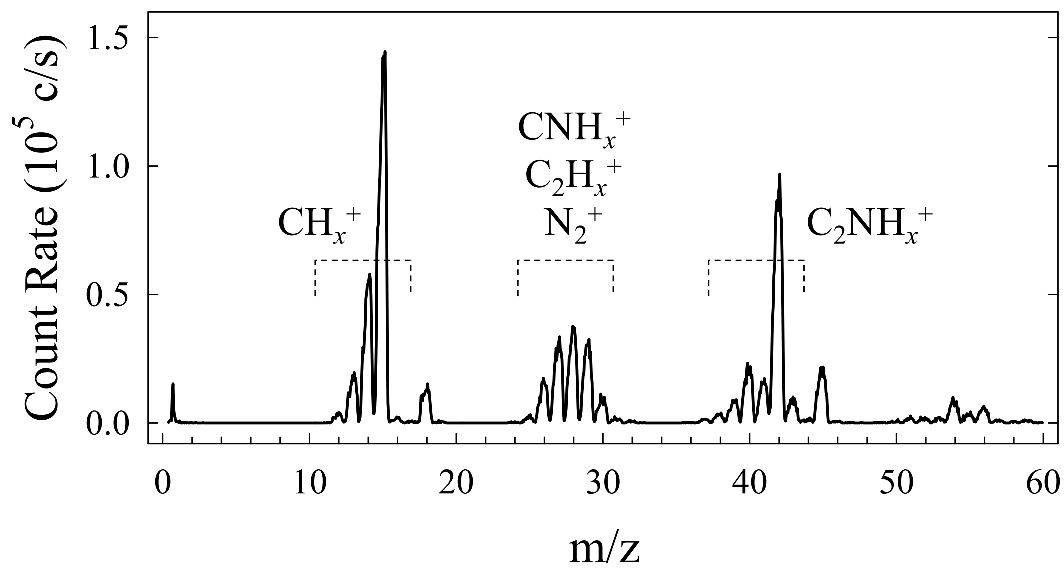

Figure 5.1 Representative mass spectrum of nascent ions in 100% CH_3CN plasma (50 mTorr, 50 W).

(CH_3CN^+, m/z = 41) is observed in the spectrum along with a group of peaks related by the number of hydrogen atoms, $C_2NH_x^+$ (x = 0-4). The substantial peaks near m/z = 42 suggest that, at the powers and pressures used here, fragmentation of the parent species is not extensive, although these peaks may also reflect contributions from recombination of CH_3 and HCN:[40]

$$CH_3^+ + HCN \rightarrow CH_3NCH^+ \qquad (5.1)$$

At lower m/z values, two main groups of ions are present. The first group has m/z values of about 12-15 and likely corresponds to CH_x^+ ions. The second group, with m/z = 26-30, may consist of both $C_2H_x^+$ and CNH_x^+ ions. N_2^+ may contribute some signal at m/z = 28, but this effect is not expected to be substantial.

The presence of the energy analyzer in our mass spectrometer demands that only a fraction of the ion energy distribution be sampled for each ion while the mass is being scanned; this has two important effects on the resulting data. First, it precludes the use of techniques such as threshold ionization mass spectrometry that can be used to distinguish ions with the same m/z, such as the $C_2H_x^+$ and CNH_x^+ ions discussed above. Another effect introduced by the energy analyzer is that, in cases where ion energy distributions for different species are very dissimilar, mass scans do not always provide an accurate representation of their relative densities.

Based on this second idea, we have performed separate energy scans for selected m/z values from each grouping of ions; integration of these energy scans should provide a more accurate indication of how the relative densities of these ions depend on the experimental parameters. These data are shown in Figure 5.2 as a function of applied rf power for m/z = 14, 15, 26-28, 41 and 42. Fragmentation processes are apparent in the

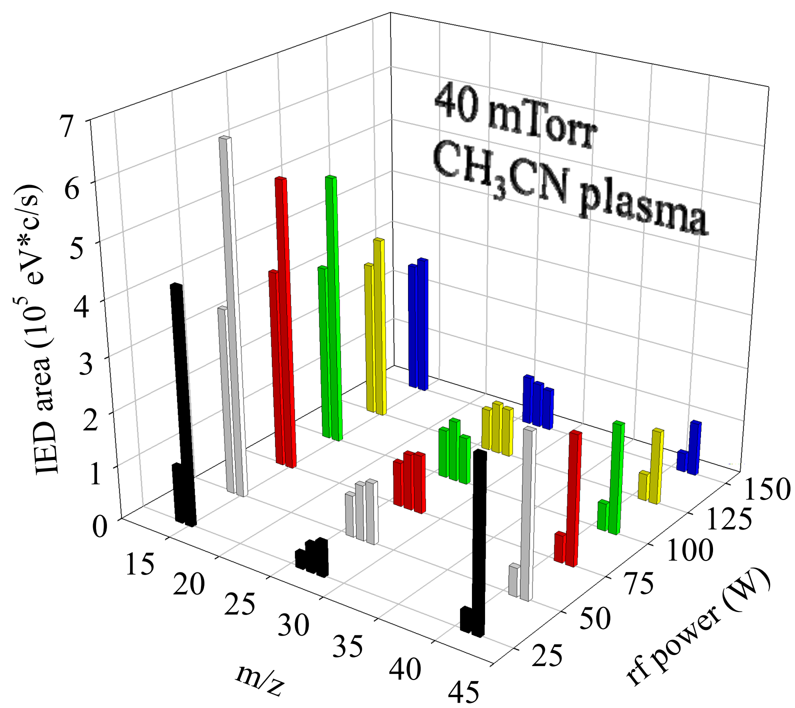

Figure 5.2 Mass signals for selected species in a 40 mTorr CH_3CN plasma as a function of applied rf power. The values for each point were generated by integrating the ion energy distribution for the corresponding *m/z* value and rf power.

variation of these signals with rf power. The *m/z* = 42 signal decreases as the parent molecules are increasingly fragmented, whereas the smaller ions exhibit a smooth progression favoring lower *m/z* peaks at higher powers. In addition, the relative difference between signals at m/z = 15 and 42 becomes greater at increased rf powers, further indication that increased fragmentation occurs under these conditions.

The mass spectral data in Figures 5.1 and 5.2 provide useful information about gas phase ionic species in CH_3CN plasmas. We have also used mass spectrometry to characterize the energies with which ions bombard a surface during processing. To provide an accurate description of the ion energies, our groups has utilized a grounded mesh screen placed between the plasma and the mass spectrometer.[23] Using a screen with holes on the order of the Debye length, λ_D, ensures that the sheath potential is relatively uniform and mimics reasonably well the field that an ion would experience near an actual surface.[41] In the present work, a metal screen with 74.9 μm holes was used (more details in Section 2.2). The Debye lengths expected in our systems are ~86 μm[42]; thus, we expect that the ion energies we measure with this geometry provide a reasonable approximation for surface ion bombardment energies in the same system.

Average ion energy data are shown in Figure 5.3 as a function of applied rf power and gas pressure. Because deposition of insulating CN_x materials on the mass spectrometer probe can cause charging of the sampling cone and subsequent shifts in the observed ion energies, data collection time was minimized by selecting three representative ions for measurement of average ions energies. Specifically, energy scans were performed at *m/z* = 15, 26, and 42, corresponding to the CH_3^+, CN^+, and $C_2NH_4^+$ ions, respectively. This selection of representative ions is supported by comparison of

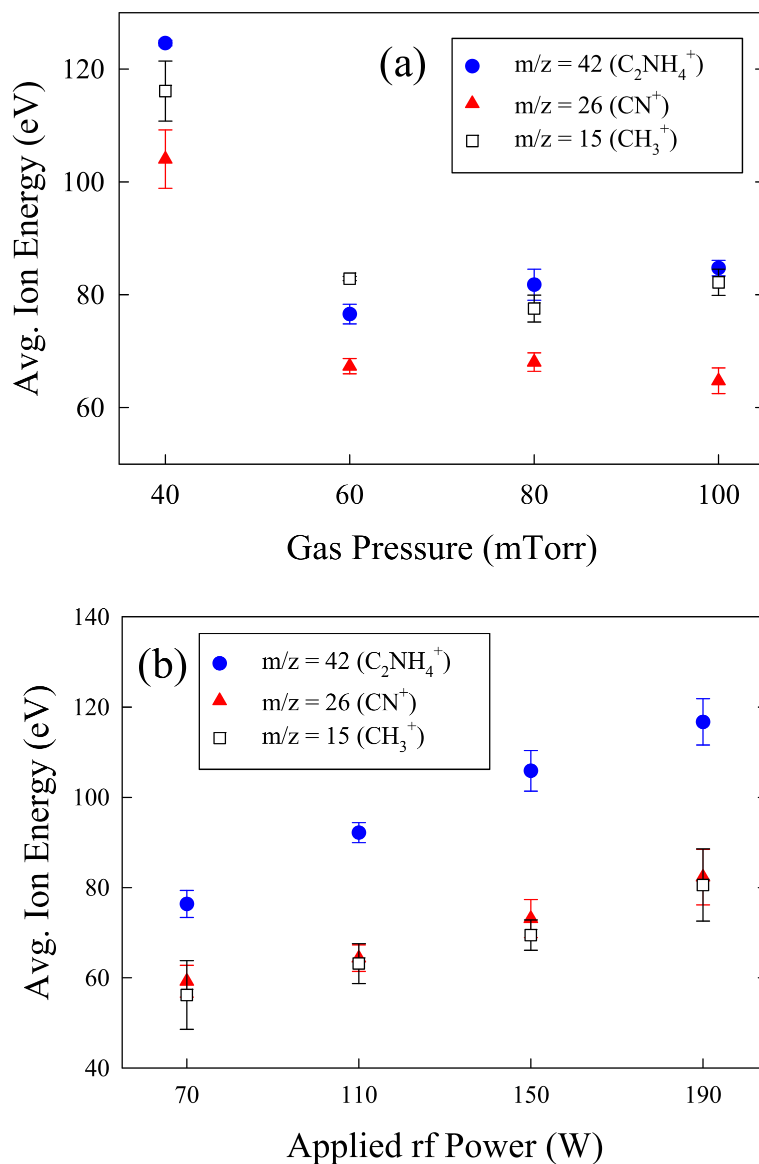

Figure 5.3 Average ion energies for *m/z* = 15, 26, and 42 ion in 100% CH_3CN plasmas, in (a) as a function of gas pressure for a 150 W plasma, and in (b) as a function of applied rf power for a 40 mTorr plasma. Error bars represent the standard deviation of the mean for three data points, each derived from a separate ion energy distribution.

the IEDs from which Figure 5.2 was generated, which indicate that energy distributions for ions from a particular group (e.g., all CH_x^+ ions) are very similar in both shape and position. The energy of one ion from each group should therefore provide a suitable picture of how energies compare across the system. Average ion energies were obtained by processing the raw ion energy distributions according to the following equation:

$$\langle E_{ion} \rangle = \frac{\int E \cdot f(E) dE}{\int f(E) dE} \tag{5.2}$$

Here, E is the ion energy and $f(E)$ is the corresponding mass spectrometer signal.

In Figure 5.3a, average ion energies are shown as a function of gas pressure for a 150 W CH_3CN plasma. Ion energies drop dramatically when the pressure increases from 40 to 60 mTorr, and at pressures >60 mTorr, ion energy does not depend on pressure considerably. A very different trend is shown in Figure 5.3b, wherein average ion energies are plotted as a function of applied rf power for a 40 mTorr CH_3CN plasma. $\langle E_{ion} \rangle$ of the selected ions all exhibit a positive correlation with applied rf power, and notably higher $\langle E_{ion} \rangle$ are observed for $C_2NH_4^+$ (*m/z* = 42) than for CN^+ and CH_3^+ whose energies are equal within experimental error. As a final note, the two sets of data in Figures 5.3a and 5.3b were collected on separate days, and the discrepancy between the 40 mTorr, 150 W energy values in the two data sets suggests that the two graphs cannot be compared directly. However, data from a single collection period are more self-consistent and provide useful information about how ion energies evolve as species approach a surface.

IEDs for CH_3^+ and $C_2NH_4^+$ are shown in Figure 5.4 as a function of pressure for a 150 W CH_3CN plasma. The energy distributions for the CN^+ ion generally look similar to those for CH_3^+ but have lower S/N and were therefore excluded from this figure. All

(a) m/z = 15 (CH_3^+)

(b) m/z = 42 ($C_2NH_4^+$)

Figure 5.4 Ion energy distributions for selected ions as a function of gas pressure in a 150 W CH_3CN plasma. Shown in (a) are the energy distributions for the m/z = 15 peak (CH_3^+) and in (b) are the energy distributions for the m/z = 42 peak ($C_2NH_4^+$).

IEDs were treated with a local smoothing function to reduce noise and facilitate comparison of basic features in the distributions. Figure 5.4 shows the emergence of a second, narrower feature in the CH_3^+ and $C_2NH_4^+$ distributions at pressures >40 mTorr. This feature appears at ~50 eV in the CH_3^+ IEDs and near 0 eV in the $C_2NH_4^+$ IEDs. The broader, higher-energy feature in the IEDs shifts to slightly lower energies with initial increases in pressure, but above 60 mTorr, the position of features in the IEDs do not shift considerably. This is manifested in the plateau in $\langle E_{ion} \rangle$ shown in Figure 5.3a.

The evolution of these IEDs with applied rf power is shown in Figure 5.5. The appearance of the narrower feature at lower energies is observed once again, here by increasing the rf power from 70 to 110 W. For CH_3^+, this peak has a similar position and relative intensity as in Figure 5.4a. In the $C_2NH_4^+$ IEDs, however, the low-energy feature is smaller relative to the broader high-energy feature and appears at higher energies than in Figure 5.4b. For each series of IEDs, features exhibit a progressive shift to higher energies as the rf power is increased. Interestingly, the higher energy feature shifts more significantly, so that the separation of the two features becomes greater at higher rf powers. These changes lead to increased $\langle E_{ion} \rangle$ as seen in Figure 5.3b.

One of the motivating factors for these studies is to gain some understanding of how ions affect the process of film deposition. Application of a positive substrate bias, V_{bias}, during deposition was thus used to inhibit surface ion bombardment and explore accompanying changes in film composition and morphology as characterized by AFM and XPS. Given the ion energies measured in Figure 5.3, a substrate bias of V_{bias} = +200 V was used in these studies to repel positive ions and limit ion bombardment of the film during deposition. Representative AFM images are shown in Figure 5.6 for V_{bias} = 0 V

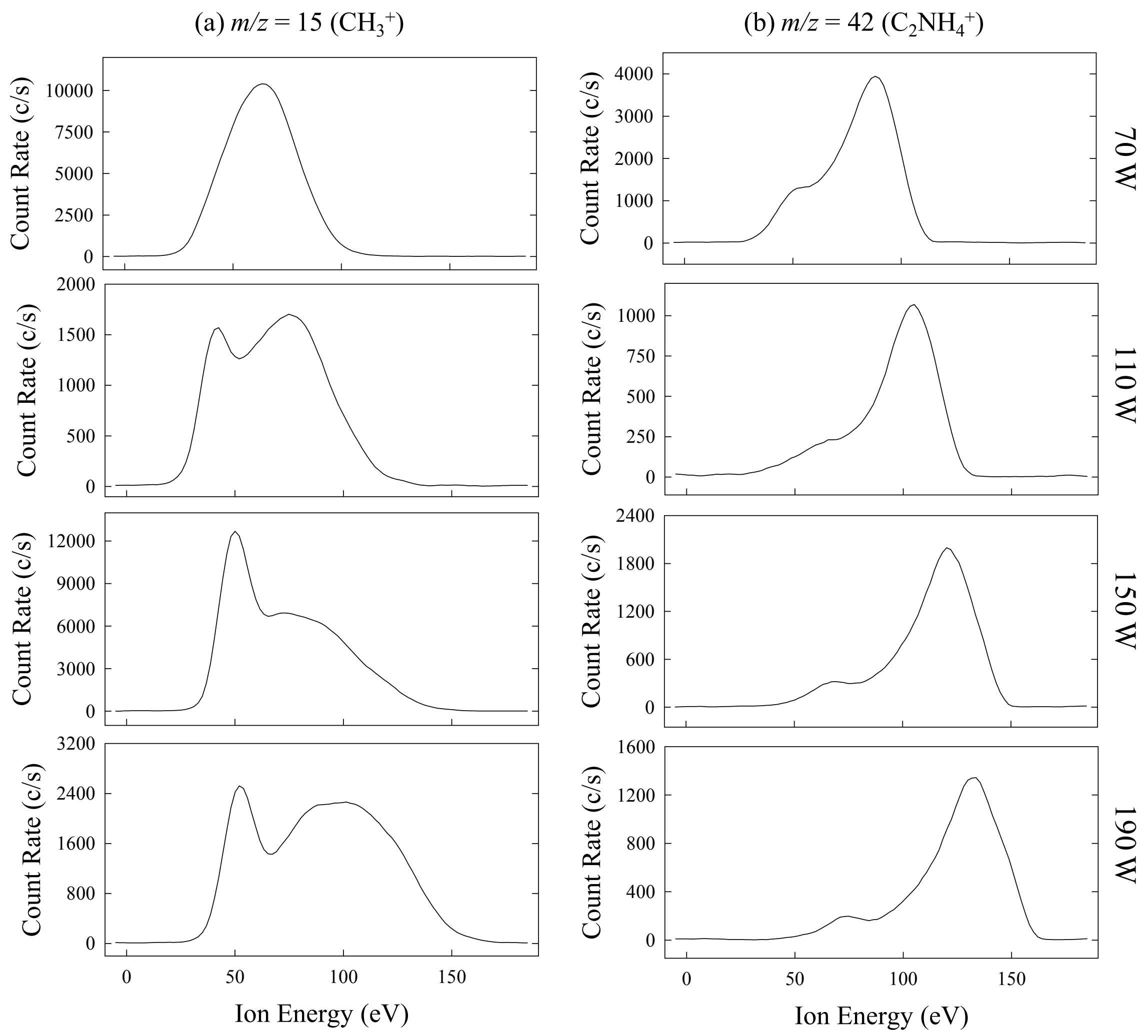

Figure 5.5 Ion energy distributions for selected ions as a function of applied rf power in a 40 mTorr CH_3CN plasma. Shown in (a) are the energy distributions for the *m/z* = 15 peak (CH_3^+) and in (b) are the energy distributions for the *m/z* = 42 peak ($C_2NH_4^+$).

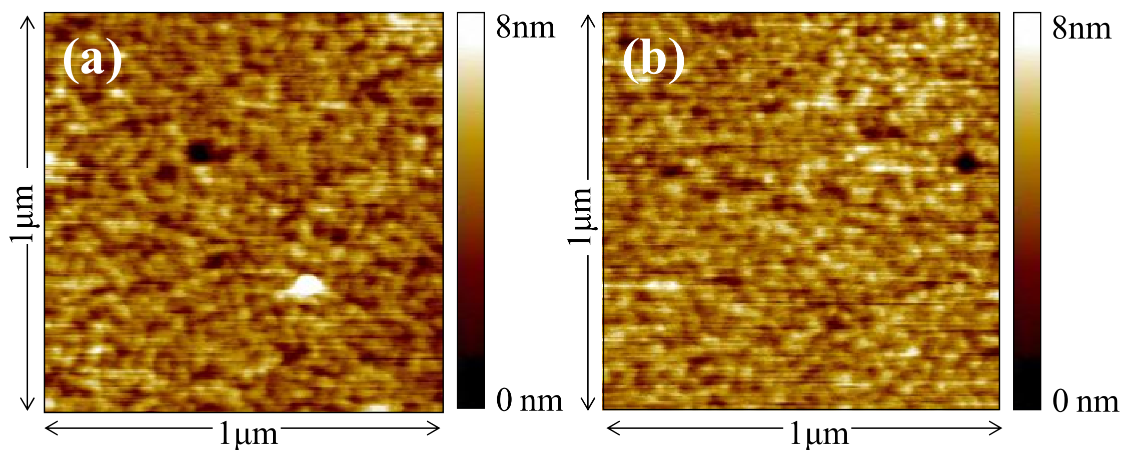

Figure 5.6 Representative AFM images of films deposited in CH_3CN plasma (100 mTorr, 50 W) with (a) V_{bias} = 0 V and (b) V_{bias} = +200 V.

and +200 V DC. Although the spatial resolution in these images is poorer than in some of our other studies (see Figure 4.9, for example), individual film grains can still be distinguished. At both substrate bias values, film grains appear to be tens of nm in size, and the films exhibit similar morphology at all scales. Quantitative support for these similarities comes from measured roughness parameters derived from the AFM images, each representing a 1 μm square area on three different film samples. The root mean square (rms) roughness, R_{rms}, and peak to peak roughness, $R_{p\text{-}p}$, of films deposited with V_{bias} = 0 V are 1.0 ± 0.3 nm and 8.6 ± 2.1 nm, respectively, and at V_{bias} = +200 V, the corresponding values are 0.7 ± 0.1 nm and 7.1 ± 1.0 nm, respectively. Clearly, the data for the different biasing conditions are within experimental error of each other, suggesting that the application of a positive substrate bias in these studies has not affected the morphology considerably. In addition, these values are indicative of relatively smooth films, even when compared to other films deposited in the same reactor and discharge system (compare to values given in Section 4.2C).

XPS data suggest that the composition of these films is similarly unaffected by substrate biasing, with N/C ratios of 0.30 ± 0.03 and 0.30 ± 0.01 at 0 and +200 V substrate bias, respectively. We commonly see some oxygen incorporation in these materials as well, possibly due to exposure to atmosphere following deposition, and the observed O/C ratios of the films deposited with V_{bias} = 0 and +200 V are 0.14 ± 0.01 and 0.15 ± 0.01, respectively. Thus, the film compositions, like the morphologies, are indistinguishable within the error of the characterization techniques used here.

5.3 Discussion

A. Mass Spectral Data. The fragmentation of acetonitrile has been investigated by several research groups;[43-47] in general, these studies highlight the importance of rearrangement and isomerization processes that accompany dissociative ionization of CH_3CN. For example, the removal of an electron from the parent molecule generates the CH_3CN^+ ion, but rearrangement of this ion gives CH_2CNH^+, which is more thermodynamically stable than the parent ion by over 2 eV.[43,45] Although this complicates the identification of specific ions and suggests that ion formation in CH_3CN plasmas cannot be described by a simple breakdown model, it is worth noting that many fragmentation studies focus primarily on lowest-energy ionization processes. As a result, fragmentation patterns presented in the literature do not always provide an adequate representation of the uniquely energetic conditions that exist in plasma discharges. This can be illustrated by consideration of two possible reactions of the parent ion, CH_3CN^+:

$$CH_3CN^+ \rightarrow CH_2CNH^+ \qquad (5.3)$$

$$CH_3CN^+ \rightarrow CH_3^+ + CN\bullet \qquad (5.4)$$

Reaction 5.3 has an energy barrier of <1 eV,[43,45] and, as discussed above, forms a product that is quite stable relative to the parent ion. Reaction 5.4, on the other hand, requires an energy of 3.3 eV. Under most conditions, Reaction 5.3 would be heavily favored thermodynamically, but in our plasma systems, as in most plasma discharges, electron energies in excess of 3 eV are very common (see Ref. 42 for Langmuir probe studies from our lab). This makes Reaction 5.4 more likely and suggests that such higher energy processes can contribute significantly to the gas phase chemistry in these systems. Indeed, our laser induced fluorescence studies (see Chapter 4) support the notion that a

fairly simple electron impact fragmentation process is responsible for the formation of neutral CN radicals in CH_3CN plasmas. Reports in the literature support the significance of high-energy breakdown processes as well.[48,49]

Despite the apparent complexities of ion formation in these systems, simple mass spectral data like those in Figure 5.1 offer some useful information. The observed peaks fall into three main groups, and although the relatively weak signals at $m/z > 50$ indicate that some amount of recombination takes place, the data suggest that breakdown of the parent molecule dominates, and we tentatively designate the ion groupings near $m/z = 15$, 28, and 42 as CH_x^+, CNH_x^+, and $C_2NH_x^+$, respectively.

Peaks separated by only a few *m/z* units likely differ only in the number of H atoms in the ions. Abstraction of H by CNH_x species is common and has been studied in mixtures of CN with hydrocarbons and other species.[48-53] Although the series of peaks with $m/z = 26$-30 are consistent with such a trend, this does not rule out possible contributions of $C_2H_x^+$ ions, as a similar series of peaks might be expected from the stepwise removal of H from C_2H_6. Additional evidence for H removal can be found in the $m/z = 12$-15 region of Figure 5.1, where the series of descending peaks indicates stepwise loss of H from the methyl ion (CH_3^+), as well as in Figure 5.2, where increases in applied rf power bring about increased signals from smaller ions at the expense of adjacent peaks with higher *m/z*.

B. Ion Energy Distributions. One of the objectives of this study was to quantify the surface incident energies of ions generated in CH_3CN discharges, and as discussed above, these energies are characterized by $\langle E_{ion} \rangle$ measured in the presence of a grounded metal screen with sufficiently small openings. Several important aspects of the trends in

$\langle E_{ion} \rangle$, Figure 5.3, are best understood in the context of the IEDs from which they are derived, Figures 5.4 and 5.5. Given the ambiguity regarding the identity of ions in the region of *m/z* = 26-28, energy distributions are only shown for CH_3^+ and $C_2NH_4^+$ ions in Figures 5.4 and 5.5.

In Figure 5.3a, the precipitous drop in $\langle E_{ion} \rangle$ for gas pressures >60 mTorr corresponds to the emergence of a narrow, low-energy feature in the IEDs in Figure 5.4. This feature is attributed to ion-neutral collisions in the plasma sheath, which can generate low-energy ions via charge transfer. For example,

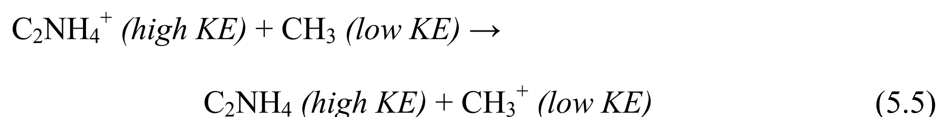

$$C_2NH_4^+ \textit{ (high KE)} + CH_3 \textit{ (low KE)} \rightarrow C_2NH_4 \textit{ (high KE)} + CH_3^+ \textit{ (low KE)} \qquad (5.5)$$

The likelihood of such a collision will depend on the value of the mean free path, which is dependent on pressure, relative to the thickness of the plasma sheath, d_s. Although Langmuir probe measurements have not been made specifically for direct measurement of the sheath thickness in CH_3CN discharges, previous measurements from our lab made in Ar and CH_4/Ar discharges suggest that the sheath thickness is on the order of several hundred μm.[42] Values for the mean free path, λ_{mfp}, at 40 and 60 mTorr are roughly 1250 and 833 μm, respectively; clearly this is in the regime of the expected sheath thickness, and the low energy feature in the IEDs is an indication that $\lambda_{mfp} < d_s$. Notably, this trend may provide a means for estimating the sheath thickness.

Similar low energy features are observed in Figure 5.5 as a function of rf power (gas pressure = 40 mTorr), although it is much less prominent for the $C_2NH_4^+$ ion. Based on the above discussion, collisions in the sheath at a gas pressure of 40 mTorr are not expected; however, power-dependent increases in fragmentation indicated by Figure 5.2

are likely to be accompanied by an increase in the system pressure during processing. It may be that these increases in gas pressure are enough to create conditions where $\lambda_{\mathrm{mfp}} < d_{\mathrm{s}}$, thereby causing the generation of low-KE ions observed in Figure 5.5.

The observed trends in $\langle E_{ion} \rangle$ are also affected by shifts in the high-energy features in the IEDs. This signal corresponds to the ions that do not experience collisions in the sheath, and their energies are primarily dictated by the sheath potential as they pass through the metal screen. Because the metal screen is electrically grounded, the sheath potential should be roughly equal to the plasma potential, V_{pl}. Previous Langmuir probe studies in our lab indicate a negative correlation between V_{pl} and pressure and a positive correlation between V_{pl} and power,[42] and the parameter-dependent shifts in the high-energy features of the IEDs in Figures 5.4 and 5.5 mirror these expected trends in the plasma potential. Interestingly, Robertson et al. suggest that ion-neutral collisions brought about by increases in pressure alter the ion loss rate at the wall and should cause V_{pl} to increase;[54] however, the experimental work that accompanied those studies was performed at lower pressures than are used in the present work, and this may account for at least some of the discrepancy.

C. Substrate Biasing Studies. As indicated by measurements of $\langle E_{ion} \rangle$ in Figure 5.3, ions in our CH_3CN discharge systems bombard the surface with a substantial amount of energy, and it is reasonable to think that this ion bombardment might affect the process of film growth. Several researchers have published reports of ion bombardment effects during a-CN_x:H deposition using a negative substrate bias to promote surface bombardment by positive ions;[36-39,55,56] among the effects noted in these studies are decreases in nitrogen content and film roughness under increased ion bombardment.

In this work, we were interested in the effects of ion bombardment in the absence of substrate biasing (e.g., for ions with bombardment energies approaching those measured in Figure 5.3). A substrate bias of +200 V DC was thus used to repel positive ions, and the morphology and composition were compared to films deposited with 0 V substrate bias. Observed ion energies in these systems are more than sufficient to bring about chemical reactions during film growth. As the XPS and AFM data show, however, both the N/C ratios and roughness factors for films deposited under different substrate bias conditions are within experimental error of each other, suggesting that ambient ion bombardment does not affect a-CN_x:H film growth to a measurable degree.

It should be noted that, in the types of glow discharges used in these studies, the degree of ionization is well below 1%, and ion densities are lower than neutral species densities by several orders of magnitude.[57] Thus, although the ions in these discharges are observed to have relatively high surface bombardment energies, it may be that they are simply not present in great enough numbers to cause an observable change in film morphology or composition. We also find empirically that our a-CN_x:H films are electrically insulating, and it is possible that the growth of these insulating films acts to attenuate the effect of an applied substrate bias as the deposition progresses. However, any changes in the discharge characteristics that might accompany such an effect would be difficult to quantify as insulating films tend to obscure Langmuir probe measurements as well.

5.4 Summary

The data presented in this chapter explore plasma chemistry in CH_3CN discharges via gas phase characterization of ionic species, measurement of ion bombardment energies, and analysis of films deposited in CH_3CN plasmas under different substrate bias conditions. In the first part, ions were sampled downstream from the plasma and detected with a mass spectrometer. Interpretation of the resulting mass spectra indicates that breakdown of the parent species dominates the gas phase chemistry and leads to the generation of CH_x^+, CNH_x^+ and $C_2NH_x^+$ ions. A grounded metal screen was placed between the mass spectrometer and the exit orifice on the plasma chamber to facilitate accurate characterization of IEDs. These IEDs can be generally described as having two features; the narrow, lower-energy features yield information about the collision environment in the plasma sheath, and the higher-energy features are primarily affected by the plasma potential. Both features have an effect on the measured average ion energies, which are observed to have values of roughly 60-120 eV. The practical effects of ion bombardment in CH_3CN discharges were investigated through the deposition of films with and without the application of a +200 V DC substrate bias. No statistically significant differences were found in either the roughness or composition of films deposited under different bias conditions, suggesting that ambient ion bombardment in these systems does not affect the deposition process to a substantial degree.

5.5 References

[1]A. Y. Liu and M. L. Cohen, Science **245,** 841 (1989).
[2]G. Goglio, D. Foy, and G. Demazeau, Mat. Sci. Eng. R **58,** 195 (2008).
[3]S. Muhl and J. M. Mendez, Diamond Relat. Mater. **8,** 1809 (1999).
[4]E. Broitman, W. Macdonald, N. Hellgren, G. Radnoczi, Z. Czigany, A. Wennerberg, M. Jacobsson, and L. Hultman, Diamond Relat. Mater. **9,** 1984 (2000).
[5]F. Z. Cui, X. L. Qing, and J. Zhao, Surf. Coat. Technol. **200,** 1009 (2005).
[6]E. C. Cutiongco, D. Li, and Y.-W. Chung, J. Tribol. **118,** 543 (1996).
[7]T.-A. Yeh, C.-L. Lin, J. M. Siversten, and J. H. Judy, IEEE Trans. Magn. **27,** 5163 (1991).
[8]D. C. Cameron, Surf. Coat. Technol. **169-170,** 245 (2003).
[9]S. Metin, J. H. Kaufman, D. D. Saperstein, J. C. Scott, J. Heyman, and E. E. Haller, J. Mater. Res. **9,** 396 (1994).
[10]X. D. Bai, D. Zhong, G. Y. Zhang, C. Ma, S. Liu, E. G. Wang, Y. Chen, and D. Shaw, Appl. Phys. Lett. **79,** 1552 (2001).
[11]S. Y. Kim, H. S. Kim, S. Augustine, and J. K. Kang, Appl. Phys. Lett. **89,** 253119 (2006).
[12]Z. H. Zhu, H. Hatori, S. B. Wang, and G. Q. Lu, J. Phys. Chem. B **109,** 16744 (2005).
[13]G. A. J. Amaratunga and S. R. P. Silva, Appl. Phys. Lett. **68,** 2529 (1996).
[14]C. Godet, J. P. Kleider, and A. S. Gudovskikh, Phys. Status Solidi B **244,** 2081 (2007).
[15]A. Zhong, G. I. Lee, C. B. Mo, S. H. Hong, and J. K. Kang, Chem. Mater. **19,** 2918 (2007).
[16]H. Cachet, C. Debiemme-Chouvy, C. Deslouis, A. Lagrini, and V. Vivier, Surf. Interface Anal. **38,** 719 (2006).
[17]P. Tamiasso-Martinhon, H. Cachet, C. Debiemme-Chouvy, and C. Deslouis, Electrochim. Acta **53,** 5752 (2008).
[18]I. Jimenez, W. M. Tong, D. K. Shuh, B. C. Holloway, M. A. Kelly, P. Pianetta, L. J. Terminello, and F. J. Himpsel, Appl. Phys. Lett. **74,** 2620 (1999).
[19]G. Soto, E. C. Samano, R. Machorro, M. H. Farias, and L. Cota-Araiza, Appl. Surf. Sci. **183,** 246 (2001).
[20]G.-Q. Yu, S.-H. Lee, and J.-J. Lee, Diamond Relat. Mater. **11,** 1633 (2002).
[21]Z. Wang, C. Wang, and J. Zhang, J. Appl. Phys. **104,** 073306 (2008).
[22]D. G. McCulloch and A. R. Merchant, Thin Solid Films **290-291,** 99 (1996).
[23]I. T. Martin and E. R. Fisher, J. Vac. Sci. Technol., A **22,** 2168 (2004).
[24]A. Amassian, R. Vernhes, J. E. Klemberg-Sapieha, P. Desjardins, and L. Martinu, Thin Solid Films **469-470,** 47 (2004).
[25]A. S. Bakai, A. I. Zhukov, and S. N. Sleptsov, J. Phys.: Condens. Matter **11,** 5681 (1999).
[26]J. Vlcek, K. Rusnak, V. Hajek, and L. Martinu, J. Appl. Phys. **86,** 3647 (1999).
[27]K. Nakamura, M. Tanaka, and H. Sugai, Plasma Sources Sci. Technol. **11,** 161 (2002).
[28]H. Ohtake, B. Jinnai, Y. Suzuki, S. Soda, T. Shimmura, and S. Samukawa, J. Vac. Sci. Technol., A **24,** 2172 (2006).
[29]J. K. Olthoff, R. J. Van Brunt, and S. B. Radovanov, J. Res. Natl. Inst. Stand. Technol. **100,** 383 (1995).

[30]J. R. Woodworth, M. E. Riley, P. A. Miller, G. A. Hebner, and T. W. Hamilton, J. Appl. Phys. **81,** 5950 (1997).
[31]J. Hopwood, Appl. Phys. Lett. **62,** 940 (1993).
[32]U. Kortshagen and M. Zethoff, Plasma Sources Sci. Technol. **4,** 541 (1995).
[33]J. Janes, U. Banziger, C. Huth, P. Hoffmann, G. Neumann, H.-C. Scheer, B. Schneemann, and U. Kohler, Rev. Sci. Instrum. **63,** 48 (1992).
[34]A. Manenschijn, E. Van der Drift, G. C. A. M. Janssen, and S. Radelaar, J. Appl. Phys. **69,** 7996 (1992).
[35]E. A. Edelberg, A. Perry, N. Benjamin, and E. S. Aydil, Rev. Sci. Instrum. **70,** 2689 (1999).
[36]A. Champi and F. C. Marques, Thin Solid Films **501,** 362 (2006).
[37]H. Y. Lee, D. K. Lee, D. H. Kang, J. J. Lee, and J. H. Joo, Surf. Coat. Technol. **193,** 152 (2005).
[38]L. R. Shaginyan, F. Fendrych, L. Jastrabik, L. Soukup, V. Y. Kulikovsky, and J. Musil, Surf. Coat. Technol. **116-119,** 65 (1999).
[39]T. Inoue, S. Oshio, H. Saitoh, and K. Kamata, Appl. Phys. Lett. **67,** 353 (1995).
[40]V. G. Anicich, A. D. Sen, W. T. Huntress, and M. J. McEwan, J. Chem. Phys. **102,** 3256 (1995).
[41]E. A. Edelberg, A. Perry, and N. Benjamin, J. Vac. Sci. Technol., A **17,** 506 (1999).
[42]J. Zhou, I. T. Martin, R. Ayers, E. Adams, D. Liu, and E. R. Fisher, Plasma Sources Sci. Technol. **15,** 714 (2006).
[43]J. C. Choe, Int. J. Mass Spectrom. **235,** 15 (2004).
[44]W. Heerma, J. J. de Ridder, and G. Dijkstra, Org. Mass Spectrom. **2,** 1103 (1969).
[45]C.-K. Huang, I.-F. Lin, and S.-Y. Chiang, Chem. Phys. Lett. **440,** 51 (2007).
[46]D. M. Rider, G. W. Raty, E. J. Darland, and G. E. Leroi, J. Chem. Phys. **74,** 1652 (1981).
[47]E. Kukk, R. Sankari, M. Huttula, S. Mattila, E. Itala, A. Sankiri, H. Aksela, and S. Aksela, Int. J. Mass Spectrom. **279,** 69 (2009).
[48]P. Li and W. Y. Fan, J. Appl. Phys. **93,** 9497 (2003).
[49]Y.-H. So, S. J. Bezuk, and L. L. Miller, J. Org. Chem. **47,** 1475 (1982).
[50]M. A. Blitz, P. W. Seakins, and I. W. M. Smith, Phys. Chem. Chem. Phys. **11,** 10824 (2009).
[51]N. Choi, M. A. Blitz, K. McKee, M. J. Pilling, and P. W. Seakins, Chem. Phys. Lett. **384,** 68 (2004).
[52]V. R. Morris, F. Mohammad, L. Valdry, and W. M. Jackson, Chem. Phys. Lett. **220,** 448 (1994).
[53]L. R. Copeland, F. Mohammad, M. Zahedi, D. H. Volman, and W. M. Jackson, J. Chem. Phys. **96,** 5817 (1992).
[54]S. Robertson, S. Knappmiller, and Z. Sternovsky, IEEE Trans. Plasma Sci. **34,** 844 (2006).
[55]S. Aizawa, M. Aono, D. Sakasegawa, N. Kitazawa, and Y. Watanabe, Adv. Sci. Technol. **39,** 43 (2003).
[56]K. C. Namiki, H. Akasaka, H. Saitoh, and H. Ito, Jpn. J. Appl. Phys., Part 1 **42,** 3682 (2003).
[57]A. Grill, *Cold Plasma in Materials Fabrication: From Fundamentals to Applications* (IEEE Press, New York, 1994).

CHAPTER 6

GAS PHASE ENERGETICS OF CN RADICALS IN RF DISCHARGES: INFLUENCE ON SURFACE REACTION PROBABILITY DURING DEPOSITION OF CARBON NITRIDE FILMS

This chapter contains data from a full paper published in the *Journal of Physical Chemsitry A* and written by Joshua M. Stillahn and Ellen R. Fisher. These data represent a detailed study of the internal energies of CN in CH_4/N_2, CH_3CN, and BrCN plasma discharges. In all cases, vibrational temperatures are significantly higher than rotational temperatures, though both are well above 300 K. Comparison of these data to studies from the literature indicates that the observed internal energies may contribute to the surface reaction of CN; this idea is also supported by a survey of reactivity data for several different molecules studied in our lab.

6.1 Introduction

Low-temperature, or "cold," plasmas allow generation of reactive species for surface processing at relatively low temperatures using a variety of molecular precursors. In these systems, local thermal equilibrium is not established and the electron temperature, T_e, is much greater than the gas temperature, T_g, with typical values of $T_e \sim$ 60,000 K and $T_g \leq 1000$ K. Activation of plasma species is thus dictated by the transfer of energy from electrons to gas-phase molecules. Knowledge of the degree of excitation of these molecules becomes valuable in forming a detailed understanding of gas phase processes, including fragmentation and recombination, as well as surface processes such as film deposition and etching. As small changes in a single parameter can lead to large changes in macroscopic properties (e.g., deposition or etch rate, etch selectivity, etc.) and process chemistries, developing insight into molecular-level characteristics such as energy partitioning in plasmas is an important goal.

Measurement of internal and translational temperatures of gas phase species is often accomplished in plasma discharges through the use of optical emission spectroscopy (OES) or laser-induced fluorescence (LIF) spectroscopy[1] but has also been achieved using other spectroscopic methods,[1,2] as well as thermocouples and temperature probes.[3] Often, the properties of a single gas phase species are used to characterize an entire discharge, either due to the non-specificity of the technique, as is the case with thermocouples and temperature probes, or because such treatments are justified, as is sometimes true with small additions of multiple rare gases.[4] However, especially in more complex gas mixtures, energy transfer can take place more efficiently for some molecules than for others, skewing the plasma chemistry in favor of certain processes. It is

therefore important to consider the gas phase properties of each plasma species separately to elucidate the important chemical processes.

We have studied gas-phase energetics for species in a range of plasma systems,[5-11] some of which deposit amorphous carbon nitride (a-CN_x) films. In a-CN_x deposition systems, our data suggest not only that the CN radical is relatively abundant but that it is one of just a few plasma radicals we have encountered that exhibit rotational temperatures well above 300 K.[12] We have frequently used rotational temperatures as an indicator of molecular internal energies, and the relatively high values obtained for CN suggested the possibility that significant amounts of energy are available in internal degrees of freedom. This tendency is important in that these energies could potentially influence the likelihood of CN undergoing additional reactions within the plasma. Indeed, one possible manifestation of this effect can be found in surface reactivity measurements from our lab (Chapter 4), which suggest CN radicals in these systems undergo surface reactions with a probability of ~94%.[5,13] In light of these observations, we are interested in further exploring the relationship between the gas phase properties and surface behavior of CN.

Photodissociation experiments are an important source of information about energy partitioning in gas phase reactions that produce CN.[14-17] These studies afford control over the energy of the incident photon, so that the disposal of energy during dissociation can be characterized by comparison of the incident photon energy to the internal and kinetic energies of the recoiling fragments. However, the strength of this technique lies in the characterization of gas phase processes, and it does not provide direct information about the influence of energetics on surface reactions. Such

information has been pursued by other researchers[18-20] by performing, in a state-specific manner, both the preparation of surface-incident molecules and characterization of scattering species. These studies highlight the pronounced efficacy of certain molecular degrees of freedom in promoting surface reactions. However, due to the chemical complexity of surface processes (see Hodgson et al.[21] and references therein), these detailed studies are generally limited to the reactions of relatively simple gas molecules (e.g., N_2, H_2) on model surfaces (single-crystal metals). Thus, the primary objective of the present work is to bridge the gap between gas phase energetics and surface reactions for the more complex case of CN radicals in plasma deposition systems. Although the gas phase chemistry and surface structure in these systems are both exceedingly complex, we feel that in the context of work found in the literature, we can reliably establish a relationship between gas phase diagnostics and surface reactivity measurements.

6.2 Results

As discussed in Section 4.2, the relatively intense band head in Figure 2.5 is an indication of an elevated Θ_R. For the purposes of determining Θ_R and Θ_V, we have chosen to scan discrete portions of the CN rotational spectrum using smaller wavelength step sizes. Here, we use the relative intensity of the N = 9-11 peaks (λ_{max} = 387.96, 388.00, and 388.04 nm, respectively) and rotational band head (λ_{max} = 388.34 nm), scanned with step sizes of 0.001 nm, to determine Θ_R as a function of experimental parameters. For each set of conditions, the maximum LIF intensities of the N = 9, 10, and 11 peaks were separately compared to two scans of the band head region, yielding a total of six measurements of Θ_R(CN). Note that this is a different approach than was

described for measuring Θ_R(CN) in Section 4.2. Although the use of measurements in the band head region of the CN spectrum prevent the isolation of individual rotational lines, the approach used here allows comparison of signals with greater absolute intensity, thus improving S/N.

Figure 6.1a shows the dependence of the mean of six such temperature measurements as a function of pressure and power for a 1:3 CH_4/N_2 plasma. The data suggest that for pressures of 40-120 mTorr, Θ_R(CN) in these plasma systems does not depend on power but is negatively correlated with pressure. This type of pressure dependence is also exhibited by CN in other plasma systems, as shown in Figure 6.1b for data collected at 50 W. Here, it is apparent that the pressure dependence of Θ_R(CN) values from CH_3CN plasmas closely mimics the results obtained from CH_4/N_2 plasmas, whereas the Θ_R(CN) values obtained from a 1:4 dilution of BrCN in Ar are ~200 K higher. Our experience with BrCN plasmas suggests that they tend to be relatively difficult to stabilize and Ar dilution was used in these experiments as a means of both stabilizing the discharge and mitigating some of the rapid film deposition on the reactor walls. Nevertheless, the appearance of elevated Θ_R in BrCN/Ar mixtures warranted closer examination, and additional Θ_R measurements were made in BrCN/Ar as a function of Ar content in the feed gas. Results of these studies are given in Figure 6.2, where there is a significant decrease in Θ_R(CN) when the Ar content in the gas mixture is greater than 40%. This trend is a noteworthy departure from those observed in our previous measurements of Θ_R(CN) in CH_3CN plasmas,[5] which indicated that Ar dilution does not affect Θ_R(CN) to a large extent. Additionally, if the BrCN/Ar data in Figure

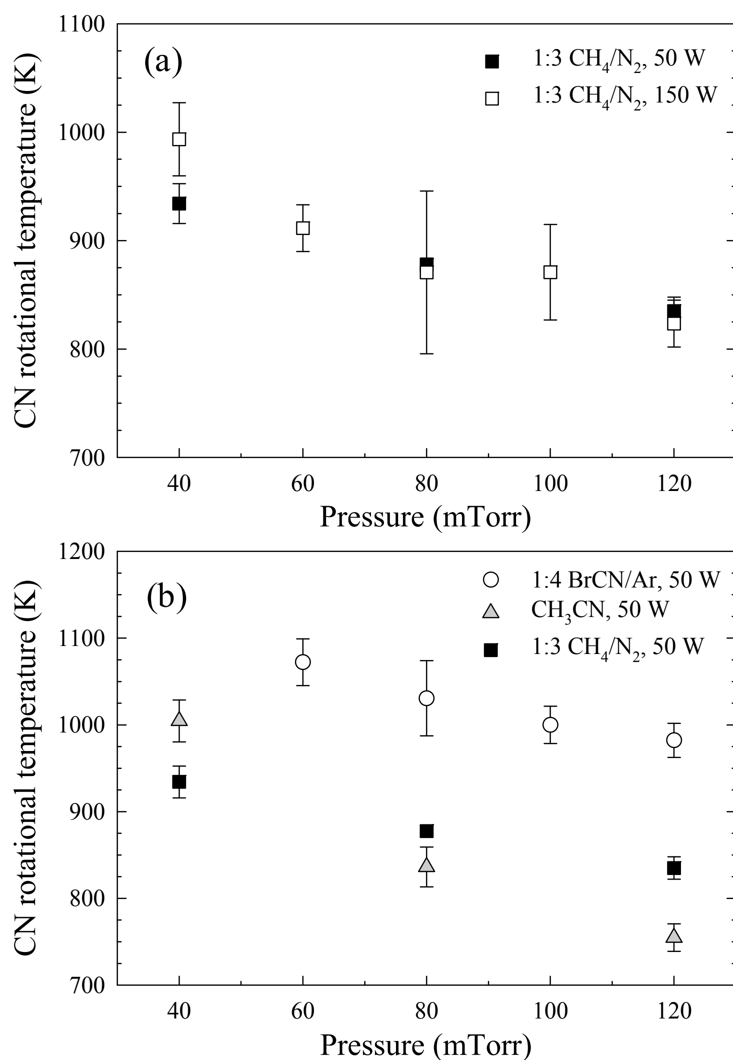

Figure 6.1 Mean rotational temperatures, Θ_R, of CN plotted in (a) as a function of total gas pressure for a 1:3 CH_4/N_2 plasma at 50 and 150 W and in (b) as a function of total gas pressure in 1:4 BrCN/Ar, 100% CH_3CN, and 1:3 CH_4/N_2 plasmas (rf power = 50W). Error bars represent one standard deviation of the mean (6 measurements).

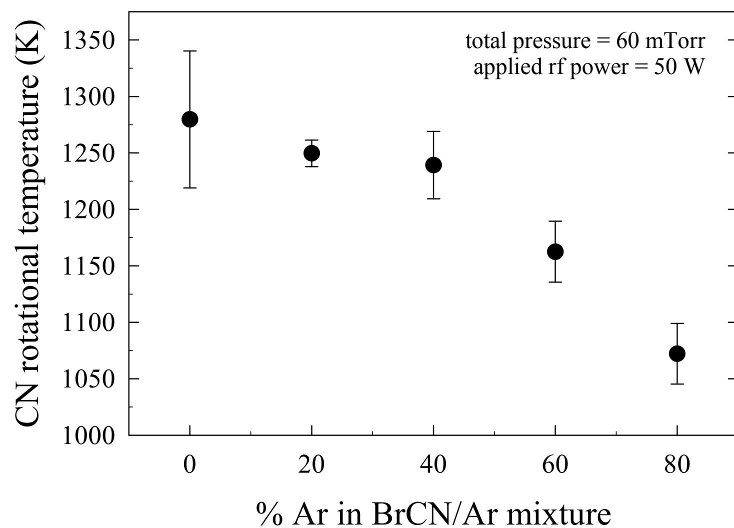

Figure 6.2 Mean rotational temperatures of CN for 50 W BrCN/Ar plasma as a function of Ar content in the gas feed (total gas pressure = 60 mTorr). Error bars represent one standard deviation of the mean (6 measurements).

6.1b are corrected for the dilution-dependent decrease in Θ_R, then their divergence from the CH_3CN and CH_4/N_2 data becomes even more pronounced.

Although such characterization of the rotational excitation provides one means of gauging the internal energy of radicals, the rotational temperature alone does not completely describe the energetics of radicals in plasma discharges. Measurement of vibrational temperature is thus useful in gaining additional insight into the gas phase energetics of plasma species. Figure 6.3a shows a CN excitation spectrum in a 1:3 CH_4/N_2 plasma with steps of 0.002 nm corresponding to a region where the (0,0), (1,1), and (2,2) vibrational bands overlap. Such overlap facilitates the measurement of Θ_V, as do the spacings of individual rotational lines in this particular spectral region. With these lines resolved, comparison of experimental spectra to simulated data provides a measure of Θ_V for ground state CN radicals in these systems.

Optimal fit between experimental and simulated data was determined primarily by measurement of the peak correlation (PC) and χ^2 fitness parameters; the former is defined in Equation 6.1,[22]

$$PC = \frac{nS_{xy} - S_x S_y}{\left[\left(nS_x^2 - S_x^2\right)\left(nS_y^2 - S_y^2\right)\right]^{1/2}} \qquad (6.1)$$

where S_x and S_y are the summation of all data points in either the simulated or experimental spectra, respectively, and n is the number of data points in either spectrum; an interpolation is performed so that n is the same for both spectra. S_{xy} is the cross summation of both the simulated and experimental spectra, Equation 6.2,

$$S_{xy} = \sum_i^n x_i y_i \qquad (6.2)$$

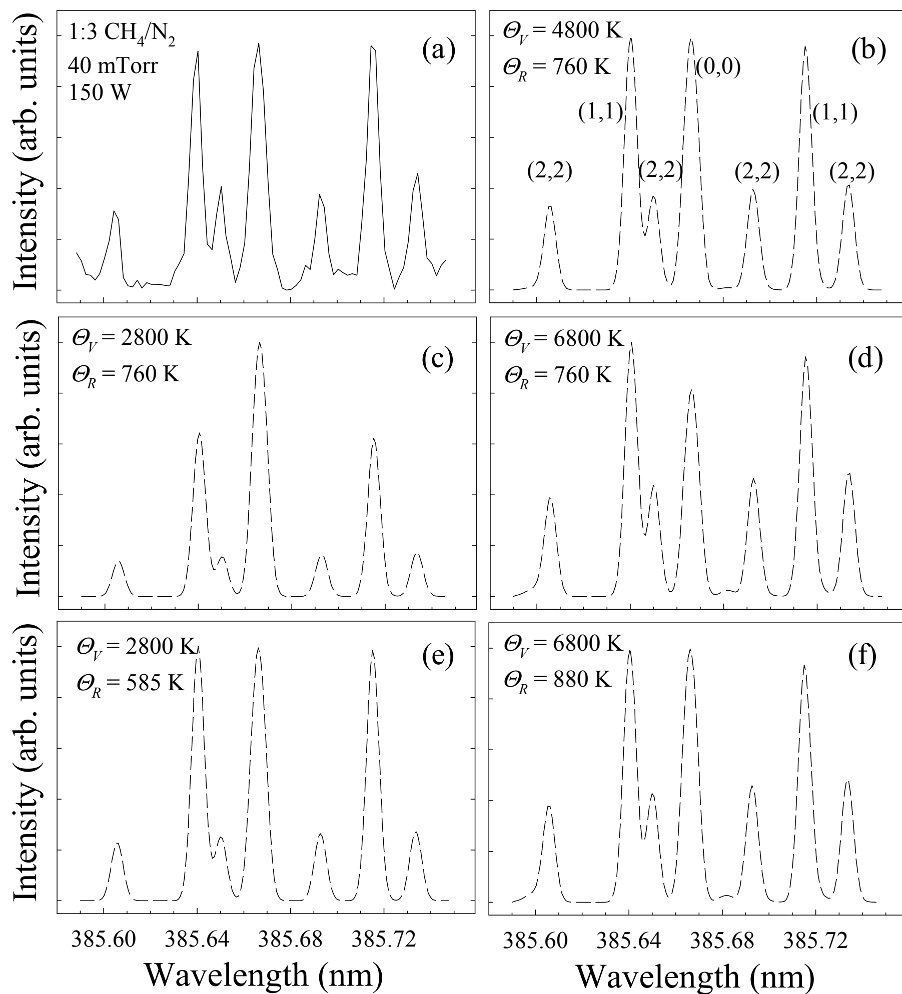

Figure 6.3 CN $B^2\Sigma^+ \leftarrow X^2\Sigma^+$ LIF spectral data in (a) collected in a 1:3 CH_4/N_2 plasma (40 mTorr, 150 W) and in (b-f) simulated at different Θ_R and Θ_V as labeled. Shown in (b) is the best match to the experimental data with identification of the vibrational band corresponding to each rotational line; (c-f) illustrate the influence of Θ_R and Θ_V on these line intensities.

The most favorable fit to the data in Figure 6.3a gives Θ_V = 4800 K and Θ_R = 760 K, as shown in Figure 6.3b. The fit is of much poorer quality when Θ_V is altered significantly, as in Figures 6.3c and 6.3d. Even in these cases, however, careful adjustment of Θ_R brings the simulated data back into rough agreement with the experimental spectrum (Figures 6.3e and 6.3f). In many cases, such qualitatively similar data give rise to very similar PC and χ^2 values, Table 6.1, limiting the precision of the fits and leading to uncertainties of up to ~1000 K for Θ_V and ~200 K for Θ_R. Note that we have also listed in Table 6.1 the fitting parameters for the two cases wherein $\Theta_R = \Theta_V$, at either 4800 K or at 760 K. As can be seen from the much higher PC and lower Θ^2 values, the rotational and vibrational temperatures are clearly not equilibrated with each other at these temperatures. The LIF data presented here are thus semi-quantitative in nature and should be treated as rough estimates of the actual values.

Similar characterization of Θ_V was carried out for CH_4/N_2, CH_3CN, and BrCN plasmas with a gas pressure of 40 mTorr and rf power of 150 W; the spectra, each an average of three separate scans, along with calculated spectra, are shown in Figure 6.4 with Θ_V and Θ_R values derived from the simulated data. Again, the fitting parameters for the simulations shown in Figure 5 are listed in Table 6.1. The results suggest Θ_V(CN) values do not differ dramatically between plasma systems and the apparent differences in the spectra are a result of differences in Θ_R. Specifically, CN derived from BrCN appears to have a higher Θ_R than does CN formed from either CH_4/N_2 or CH_3CN. It is also worthwhile to compare these data to the trend shown in Figure 6.1b. Although the two data sets correspond to different experimental conditions, the relationships between Θ_R(CN) for the different precursors are very similar in each case.

Table 6.1 Fit parameters for spectral simulations

Figure	Θ_V(K)	Θ_R(K)	PC	χ^2
4b	4800	760	0.972	34.98
4c	2800	760	0.933	141.84
4d	6800	760	0.957	49.09
4e	2800	585	0.967	52.10
4f	6800	880	0.968	37.04
Not shown	4800	4800	0.702	336.60
Not shown	760	760	0.568	598.48
5a	4800	760	0.972	34.98
5b	5000	690	0.972	27.36
5c	5800	1300	0.961	35.92
6a	4900	1150	0.993	4.19
6b	6400	1450	0.992	4.44
6c	8000	1600	0.993	4.87

[a]Fits for Figure 6.4b-f, as well as those listed as not shown, reflect comparisons to experimental data shown in Figure 6.4a.

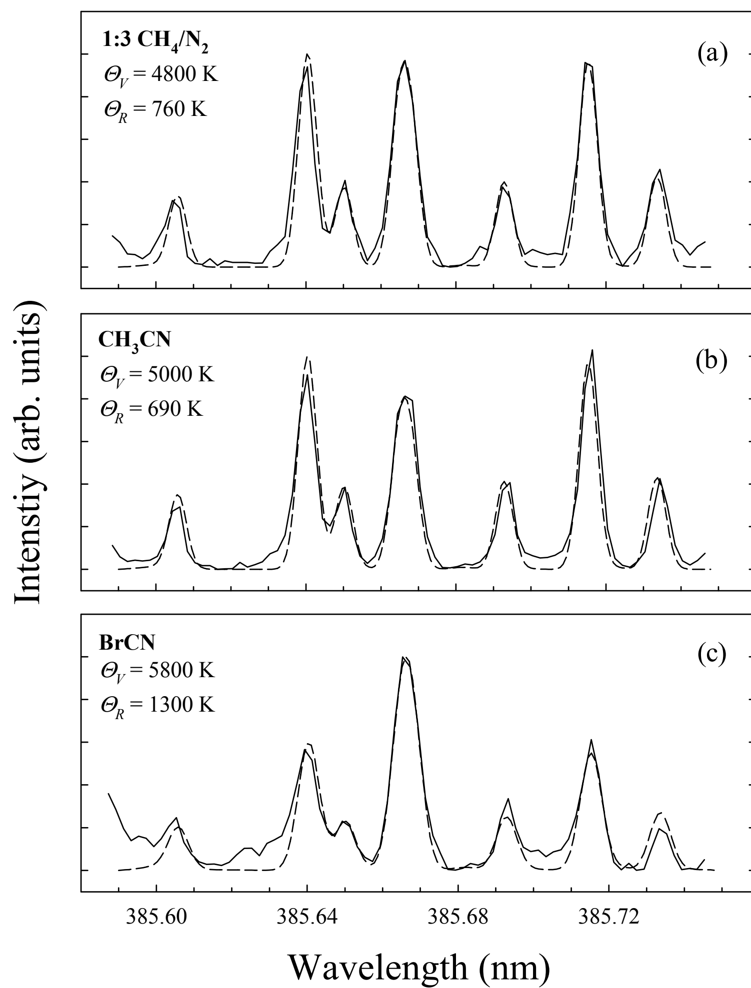

Figure 6.4 Experimental CN $B^2\Sigma^+ \leftarrow X^2\Sigma^+$ LIF spectral data (solid lines) collected in (a) 1:3 CH_4N_2, (b) CH_3CN, and (c) BrCN plasma (40 mTorr, 150 W). Also shown are simulated spectral data (dashed lines) corresponding to the Θ_R and Θ_V values shown.

In addition to the uncertainty associated with simulating this particular spectral region noted above, the measurement of Θ_V by LIF is limited by the time required to scan a narrow-linewidth laser across a spectral window large enough to include multiple vibrational bands. OES offers some advantages as an alternative spectral technique in that it allows the simultaneous collection of data over a much larger spectral window. Note, however, that LIF and OES probe ground state and electronically excited species, respectively, precluding direct comparison of data from these techniques. Nonetheless, we were interested in using OES to gain additional insight into the partitioning of internal energy in CN radicals in these plasma systems.

OES spectra are shown in Figure 6.5 for 1:3 CH_4/N_2, CH_3CN, and BrCN plasmas, and each spectrum shown is an average of three spectra taken at different points in time within a period of ten minutes. The experimental data were simulated by allowing the rotational temperature of each vibrational band to vary independently, yielding a semi-quantitative measurement of Θ_V and Θ_R. For the sake of brevity, only the Θ_R values corresponding to the (0,0) vibrational band are listed in Figures 6.5a-c. In practice, however, the Θ_R values for other vibrational bands were higher than in the (0,0) band. Precedent for this type of behavior exists in the literature,[16] and it is possible that inclusion of the additional rotational energy in excited vibrational states would reveal a more statistical distribution of internal energy. Inclusion of rotational temperatures of higher vibrational states in estimates of Θ_R from our OES data indicate that this may be true to a certain extent but even with these included, vibrational energy is still significantly higher than the total rotational energy by more than 0.17 eV for all systems. The largest discrepancy between the experimental and simulated data is observed for the

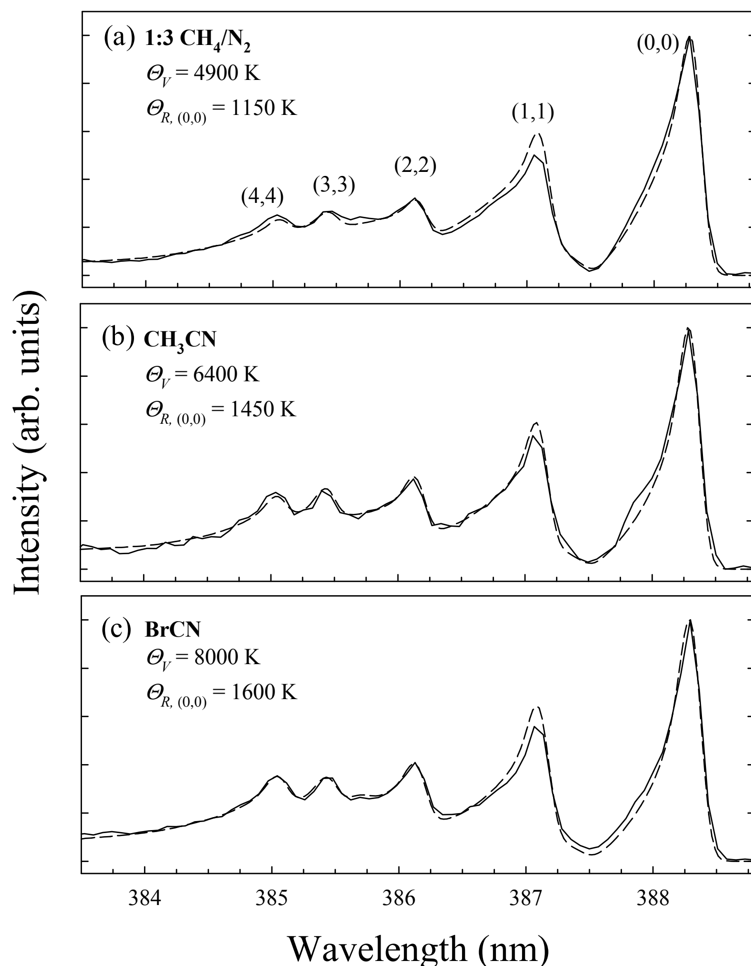

Figure 6.5 Optical emission spectra of (a) 1:3 CH_4/N_2, (b) CH_3CN, and (c) BrCN plasma in the spectral region corresponding to the CN $B^2\Sigma^+ \rightarrow X^2\Sigma^+$ transition. The experimental spectra shown (solid lines, 100 mTorr, 50 W) each represent an average of three spectra and were fit with simulated data (dashed lines) corresponding to different values of Θ_V (vibrational bands identified in (a)) and Θ_R (values of Θ_R for each vibrational band were allowed to vary independently, but only the value corresponding to the (0,0) vibrational band is shown).

(1,1) vibrational band, accounting for up to 23% of the disparity in total residual area. In spite of these inconsistencies, overall PC and χ^2 values, Table 6.1, were consistently on the order of 0.99 and 4.5, respectively, indicating that the simulated data reproduce the experimental spectra reasonably well. The resulting temperatures are consistently higher than in the LIF data but support the observation of greater CN internal energies in BrCN plasma and significantly higher Θ_V than Θ_R in all cases.

6.3 Discussion

A. Formation of CN. CN radicals are produced in copious amounts in all three plasma systems studied and under all experimental conditions employed. Given the clear differences in the CN precursors used, it is useful to explore possible formation mechanisms and how those mechanisms may affect energy disposal in the CN molecule. The spectral data presented here are largely consistent with previous studies from our laboratory, which explored Θ_R in CH_3CN plasmas.[5] In these previous studies, Θ_R(CN) was not affected by changes in the applied rf power but did exhibit a negative correlation with pressure, which was credited to collisional cooling effects. Here, the investigation of these trends has been extended to include alternate CN precursors, namely BrCN and CH_4/N_2. The observed trends are very similar; Θ_R(CN) values decrease with pressure for all precursors and are independent of rf power, with the latter trend illustrated for the CH_4/N_2 system in Figure 6.1a. Thus, it appears that the parameter-dependence of Θ_R(CN) is a function of the CN radicals themselves and not the plasma system in which they are generated. Notably, Θ_R(CN) values obtained in CH_3CN plasmas here are significantly lower than those measured in our previous work, which were measured

using peaks from a different region of the LIF excitation spectrum. We attribute these differences to the manner in which the line profile of the laser light affects the apparent intensity of the lines in different spectral regions. We believe our current measurements are more accurate as they are not as susceptible to the background signal associated with amplified spontaneous emission (ASE) in the exciting beam. Furthermore, the data collected in the current work are self-consistent and provide a good basis for comparison of experimental parameters and gas composition.

The examination of the current data obtained in different feedgas mixtures reveals some interesting differences with implications for mechanisms of gas phase formation of CN. Upon first inspection of the precursors studied here, it may seem reasonable to hypothesize that CN radicals formed in CH_3CN would resemble radicals generated in BrCN more closely than those generated in a CH_4/N_2 mixture. Like CH_3CN, BrCN allows the formation of CN through the scission of a single covalent bond, whereas the CH_4/N_2 system requires some form of reaction or recombination to form CN. The data in Figure 6.1b paint a very different picture, however, with BrCN values much higher those obtained in CH_3CN and CH_4/N_2 plasmas, the latter two systems yielding CN radicals with internal temperatures that are nearly the same within experimental error. This trend suggests that CN formation in CH_4/N_2 plasmas may not consist simply of recombination of atomic carbon and nitrogen species, Reaction 6.3,

$$C(g) + N(g) \rightarrow CN(g) \quad (6.3)$$

but instead may involve the formation of larger intermediate species such as CH_xNH_y, Reaction 6.4,

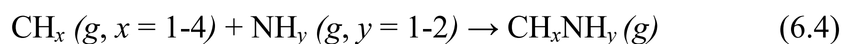

$$CH_x\ (g, x = 1\text{-}4) + NH_y\ (g, y = 1\text{-}2) \rightarrow CH_xNH_y\ (g) \quad (6.4)$$

from which CN is formed in a process more closely resembling the decomposition of CH_3CN. Moreover, the data suggest there is an important difference associated with the BrCN precursor, giving rise to Θ_R values that are ~35% higher than those in CH_3CN or CH_4/N_2 plasmas. Notably, this result is consistent with the photodissociation work of Ashfold and Simons.[14,15]

The simplest explanation for this difference in Θ_R might be that BrCN has a lower ΔH_r to form CN (3.80 eV in BrCN vs. 5.24 eV in CH_3CN),[23] so that a larger amount of excess energy is available following electron impact dissociation of BrCN, which is partitioned into the internal and kinetic degrees of freedom of CN. This hypothesis is supported by the work of Ashfold and Simons,[15] who studied the photodissociation of a series of cyanogen molecules, CNX, where X is I, Br, Cl, CH_3, or H. For a given photon energy, dissociation of CNX generally produced more rotationally-excited CN in cases where more energy was available after dissociation (i.e. for dissociation reactions with lower ΔH_r). A similar trend is evident in the variation of photon energy for a given molecule. That is, increasing the photon energy increases the amount of energy in excess of the dissociation energy and is accompanied by more extensive rotational excitation of CN after dissociation. One additional relevant observation from Ashfold and Simons' work is that when photodissociation occurred from the predissociative "C" band system of BrCN, the C-N bond length was increased, but the molecule retained a near linear geometry. Predissociation from this state resulted in more energy disposal in vibrational modes relative to translational excitation. A concomitant increase in energy disposal via rotational excitation was also observed. These observations from the literature suggest

that formation of CN in the plasma gas mixtures studied here may be occurring with sufficient energy to access these excited states.

An alternative explanation for the increased Θ_R(CN) in the BrCN system involves changes in the timescale associated with precursor dissociation, as indicated in a number of photodissociation studies.[17,24] These studies suggest that fast, impulsive dissociation of CN-containing precursors proceeds through a linear transition state and that, because the molecular fragments do not have a chance to thermally equilibrate, such conditions give rise to lower rotational temperatures and potentially higher translational temperatures. In contrast, slower reaction dynamics favor a bent transition state and allow more complete equilibration of the molecular degrees of freedom, producing CN radicals with higher rotational temperatures. Thus, the higher Θ_R(CN) values we measure for BrCN (relative to the other two precursor systems) may be a reflection of slightly slower dissociation dynamics that allow more compete equilibration of the rotational modes. In accord with this hypothesis, Bird and Donaldson have suggested that the rotational energy of CN formed from dissociation of polyatomic species (e.g., CH_3CN or CH_2CHCN) is directly proportional to the product of $\sin^2\theta$ and the available energy, where θ is the bond angle between CN and the other fragment (e.g., CH_3 in CH_3CN).[25] Again, this relationship suggests that molecular geometry plays an important role in determining the rotational energy of the CN fragment after dissociation, and although the lower Θ_R(CN) values observed in CH_3CN and CH_4/N_2 suggest a transition state with a lower Θ_R value than in the BrCN system, it is possible that the relevant bond angle does not correspond to an entirely linear transition state.

It is also possible that the Θ_R(CN) values we measure are influenced by spin-orbit coupling in the parent molecule. Such coupling in BrCN has been explored in detail;[26,27] generally, these studies suggest that strong spin-orbit coupling induced by the relatively heavy Br atom may provide access to otherwise forbidden BrCN* excited states during dissociation, leading to very different excitation profiles in the recoiling fragments. Indeed, a number of studies suggest that the dissociation of cyanogen halides gives rise to the population of some unusual excited states, such as the $^4\Sigma^+$ and $^4\Pi$ states of CN.[28,29] Moreover, both photodissociation and electron impact dissociation studies suggest Rydberg states of the BrCN parent molecule may also affect rotational and vibrational excitation of the resulting CN.[15,26] Although a detailed exploration of precursor-dependent differences in our Θ_R(CN) data is not within the scope of the current study, it is possible that one or more of these effects is prevalent in the plasma systems studied here.

The distinctions between precursors shown in Figure 6.1b are also apparent in the analysis of the more complex spectral region shown in Figure 6.4. That is, Θ_R(CN) values in BrCN plasmas are much higher than those obtained in CH_3CN and CH_4/N_2 systems, and values from the two hydrocarbon-based plasmas are quite similar. However, comparison of absolute Θ_R(CN) values from the two data sets reveals a disparity of about 200 K (the most direct comparison being between the 40 mTorr, 150 W data in Figure 6.1a and Figure 6.4a). This disparity may be a result of the small number of rotational states analyzed in the spectral window shown in Figure 6.4, but within the larger error associated with Figure 6.4 data, the two sets of data agree reasonably well. We find that a relatively large degree of error exists in our measurement of Θ_V(CN) as

well, making distinctions between precursors in Figure 6.4 very difficult. Still, the measured vibrational temperature is much higher than the rotational temperature in each system, suggesting that a larger amount of energy is partitioned into the vibrational degrees of freedom during CN formation. To confirm this observation, we used OES to analyze CN emission over a wider spectral window. Although the uncertainty of these measurements once again prevents detailed interpretation of the data, it is clear that a very similar relationship exists between Θ_V and Θ_R. In addition, we note that in most cases, temperatures measured with OES are higher than those obtained with LIF, which might indicate that electronic excitation of CN radicals also leads to the excitation of vibrational and/or rotational degrees of freedom.

The observation that Θ_V(CN) is much higher than Θ_R(CN) in our plasma systems is consistent with a number of previous studies that suggest that energy disposal into vibrational modes of CN is efficient, regardless of the precursor. For example, Nagata et al. found that the vibrational temperature of CN($B^2\Sigma^+$) formed via electron impact dissociation of BrCN was higher than expected from simple energy calculations.[26] Likewise, several photodissociation studies of both BrCN and CH_3CN have found similarly hot vibrational temperatures for the resulting CN fragment.[14,15,17] Howle et al. found Θ_V(CN) ~ 5000 K for CN formed in the photodissociation of CH_3CN using photon energies of 11.5-16 eV,[17] and in all cases, a greater than statistical proportion of the available energy was deposited in vibrational modes of CN. Corresponding Θ_R(CN) values were calculated for distributions in low rotational states, yielding values of ~600 K, ~500 K, and ~400 K for the v = 0, 1, and 2 bands, respectively. The similarities

between these values and those determined here suggest formation of CN in our plasmas may occur through similar mechanisms.

B. Surface Interactions of CN. Aside from the information that the Θ_V(CN) and Θ_R(CN) values provide about the gas phase chemistry of the different plasma systems, additional insight into the film deposition process can be gained from considering the way that these temperatures influence the surface behavior of the CN radical. Previous IRIS studies of CH_3CN plasmas (Chapter 4) suggest that CN radicals undergo surface reactions with a probability of about 80%, irrespective of the experimental conditions.[5] These reactivity data have since been improved to include a correction for the effects of Θ_R, leading to higher reactivity values with a global average of ~94%. Our previous reactivity measurements in N_2/CH_4 and NH_3/CH_4 plasmas also show near unity CN surface reactivities,[13] indicating CN radicals participate in the deposition chemistry in some capacity. X-ray photoelectron spectroscopy (XPS) data reported in Chapter 4 show films deposited in CH_3CN plasmas contain significant amounts of nitrogen, with N/C ratios of ~0.4, and OES spectra suggest that few species other than CN are present in the gas phase which could contribute to the N-content of the deposited films. In light of these data, we concluded that the high surface reactivities observed in these systems strongly suggests the incorporation of CN radicals in the growing a-CN_x film. The current work is a valuable progression of these studies, as it allows the development of a more complete model of the chemical dynamics of the CN radical during plasma processing.

The high CN vibrational and rotational temperature data presented here indicate significant excitation of CN radicals in these systems. For example, at a vibrational

temperature of 5000 K, greater than half of the $CN(X^2\Sigma^+)$ molecules are in an excited vibrational state, with significant population of states as high as $\nu = 5$. The energies of these vibrational levels are 0.04-0.20 eV above the ground vibrational state, so that vibrationally excited CN radicals in these systems can transfer energies to the surface that are equivalent to several k_BT, potentially increasing the likelihood of surface reactions. Indeed, Voevodin et al. have suggested a correlation between the deposition of highly vibrationally excited CN (Θ_V up to 4 eV) and the formation of more fullerene-like CN_x films.[30]

Several studies have more directly examined the efficacy of internal energy in promoting surface reactions,[19,31] many of them building upon the gas-phase work of Polanyi et al.[32] In general, these studies support the idea that internal energy may help promote surface reactions, especially for those characterized by late-barrier potential energy surfaces.[31-33] This term describes a potential surface in which the barrier to product formation is located closer to the exit channel. Molecules that enter these late-barrier surfaces with significant internal energy (particularly vibrational energy) tend to approach the reaction barrier with a larger component of their momentum along the reaction coordinate oriented perpendicular to the reaction barrier. Vibrational energy is therefore more effective than translational energy in promoting surface reaction in these cases.

To further explore the hypothesis that the gas-phase energetics of plasma species are related to the measured surface reactivities from IRIS experiments, we have compiled data for several different diatomic species formed in a range of plasma systems, Table 6.2. Although not all the values are available for some molecules, some broad trends

Table 6.2 Surface interaction data for selected plasma species.

Radical	Θ_R(K)	Θ_V(K)	Θ_T(K)	Reactivity, R[a]	Rel. reactivity[b]	System	Refs.
CH	1450	–	6000	0.99	high	CH_4/Ar	11
CN	1000	5000	–	0.94	high	CH_3CN	5
SiH	600	–	1200	0.95	high	SiH_4	8
OH	380	–	675	0.55-0.65[c]	moderate	DMDMOS/O_2	34
NH	370	–	390	0.40-0.80	moderate	NH_3	35
NH_2	340	–	650	(-0.29)-0.13[c]	low	NH_3	6,7

[a]Surface reactivity measured using our imaging of radicals interacting with surfaces (IRIS) technique. Negative reactivity coefficient reflects surface generation.
[b]Relative reactivity scale: low = < 0.25; moderate = 0.25-0.8; high = > 0.8.
[c]This value is highly dependent on substrate temperature (300-700 K).

emerge from these data. As predicted, plasma radicals with elevated internal and kinetic energies (e.g., CH, CN, SiH) exhibit much higher surface reactivity values than species with near room temperature Θ_R values (e.g., OH, NH, NH_2).[12] Although we currently only have Θ_V data for CN, additional support for internal energy influencing surface interactions comes from ongoing work in our laboratories using CF_4 and C_2F_6 plasmas.[36] In these systems, we have measured $\Theta_V(CF_2{}^*)$ ~400-1400 K in CF_4 and C_2F_6 plasmas; corresponding IRIS reactivity studies yield extremely low surface reactivities for CF_2. Interestingly, of the species listed in Table 6.2, the NH molecule is apparently the most energetically equilibrated. NH surface reactivities range from 0.4 to 0.8, depending on the plasma conditions, which suggests other plasma species may be contributing to the observed interactions. Notably, the surface reactivity of CH, CN, and SiH do not change appreciably with experimental parameters, creating a sharp contrast with the other three molecules in Table 6.2, whose surface interactions are highly dependent on plasma and substrate conditions. Although these data suggest that the internal and kinetic energies of plasma species do influence their surface behavior, additional data (currently being pursued by other members of the Fisher group) are needed in order to understand this relationship in greater detail.

6.4 Summary

Previous IRIS studies have shown that during the steady state growth of a-CN_x films, CN plasma radicals react with high probability at the film surface. The present work examined the gas phase energetics of CN radicals with LIF and OES, revealing that CN generated from CH_4/N_2, CH_3CN and BrCN plasmas are characterized by Θ_R and Θ_V

values well above room temperature. The highest Θ_R values were observed for CN generated in BrCN plasma. Parallels between these data and the results of photodissociation studies of single-molecule cyanogen species suggest that the differences we observe in Θ_R may reflect, among other things, subtle differences in the geometries of the respective transition states. Although precursor-dependent differences in vibrational temperature were below the sensitivity of the current work, the measurements show that Θ_V is significantly higher than Θ_R in all systems, with approximate values of 5000 and 1000 K, respectively. Finally, in the context of studies that correlate the internal excitation of diatomic molecules to their surface reaction probability, we conclude that the internal (and perhaps kinetic) energies of CN plasma radicals are largely responsible for their high surface reactivity.

6.5 References

[1]I. P. Herman, *Optical Diagnostics for Thin Film Processing* (Academic Press, San Diego, 1996).

[2]S. G. Belostotskiy, Q. Wang, V. M. Donnelly, D. J. Economou, and N. Sadeghi, Appl. Phys. Lett. **89,** 251503 (2006).

[3]W. C. Roman and J. C. Hermanson, Pure Appl. Chem. **66,** 1259 (1994).

[4]M. J. Schabel, V. M. Donnelly, A. Kornblit, and W. W. Tai, J. Vac. Sci. Technol., A **20,** 555 (2002).

[5]J. M. Stillahn and E. R. Fisher, J. Phys. Chem. C **113,** 1963 (2009).

[6]P. R. McCurdy, C. I. Butoi, K. L. Williams, and E. R. Fisher, J. Phys. Chem. B **103,** 6919 (1999).

[7]C. I. Butoi, M. L. Steen, J. R. D. Peers, and E. R. Fisher, J. Phys. Chem. B **105,** 5957 (2001).

[8]W. M. M. Kessels, P. R. McCurdy, K. L. Williams, V. A. Venturo, G. R. Barker, and E. R. Fisher, J. Phys. Chem. B **106,** 2680 (2002).

[9]J. Zhang, K. L. Williams, and E. R. Fisher, J. Phys. Chem. A **107,** 593 (2003).

[10]J. Zhou, J. Zhang, and E. R. Fisher, J. Phys. Chem. A **109,** 10521 (2005).

[11]J. Zhou and E. R. Fisher, J. Phys. Chem. B **110,** 21911 (2006).

[12]J. M. Stillahn, K. J. Trevino, and E. R. Fisher, Annu. Rev. Anal. Chem. **1,** 261 (2008).

[13]D. Liu and E. R. Fisher, J. Vac. Sci. Technol., A **25,** 368 (2007).

[14]M. N. R. Ashfold and J. P. Simons, J. Chem. Soc., Faraday Trans. 2 **74,** 1263 (1977).

[15]M. N. R. Ashfold and J. P. Simons, J. Chem. Soc., Faraday Trans. 2 **74,** 280 (1978).

[16]J. Guo, T. Carrington, and S. V. Filseth, J. Chem. Phys. **115,** 8411 (2001).

[17]C. R. Howle, A. N. Arrowsmith, V. Chikan, and S. R. Leone, J. Phys. Chem. A **111,** 6637 (2007).

[18]H. A. Michelsen, C. T. Rettner, and D. J. Auerbach, J. Chem. Phys. **98,** 8294 (1993).

[19]L. B. F. Juurlink, D. R. Killelea, and A. L. Utz, Prog. Surf. Sci. **84,** 69 (2009).

[20]B. E. Hayden and C. L. A. Lamont, Phys. Rev. Lett. **63,** 1823 (1989).

[21]A. Hodgson, Prog. Surf. Sci. **63,** 1 (2000).

[22]J. Luque, personal communication.

[23]S. G. Lias, J. E. Bartmess, J. F. Liebman, J. L. Holmes, R. D. Levin, and W. G. Mallard, J. Phys. Chem. Ref. Data **17,** 1 (1988).

[24]J. A. Coxon, J. Chem. Phys. **58,** 2244 (1973).

[25]C. A. Bird and D. J. Donaldson, Chem. Phys. Lett. **249,** 40 (1996).

[26]T. Nagata, T. Kondow, and K. Kuchitsu, Chem. Phys. Lett. **95,** 97 (1983).

[27]W. S. Felps, G. L. Findley, and S. P. McGlynn, Chem. Phys. Lett. **81,** 490 (1981).

[28]J. M. Cook, B. R. Zegarski, and T. A. Miller, J. Chem. Phys. **68,** 4763 (1978).

[29]H. Ito, Y. Ozaki, K. Suzuki, T. Kondow, and K. Kuchitsu, J. Chem. Phys. **96,** 4195 (1992).

[30]A. A. Voevodin, J. G. Jones, J. S. Zabinski, Z. Czigany, and L. Hultman, J. Appl. Phys. **92,** 4980 (2002).

[31]C. Diaz and R. A. Olsen, J. Chem. Phys. **130,** 094706 (2009).

[32]J. C. Polanyi and W. H. Wong, J. Chem. Phys. **51,** 1439 (1969).

[33]G. R. Darling, Handbook of Surface Science **3,** 141 (2008).

[34]J. Zhang and E. R. Fisher, J. Phys. Chem. **108,** 9821 (2004).

[35]E. R. Fisher, P. Ho, W. G. Breiland, and R. J. Buss, J. Phys. Chem. **96,** 9855 (1992).
[36]M. F. Cuddy and E. R. Fisher, J. Appl. Phys. (manuscript in preparation).

CHAPTER 7

DEPOSITION OF a-CN_x MATERIALS IN PLASMAS CONTAINING BrCN: EXPLORING ADHESION BEHAVIOR AS AN INDICATOR OF FILM PROPERTIES

In this chapter, preliminary data are presented concerning the delamination of materials deposited in BrCN-containing plasmas. Our observations of this phenomenon are consistent with studies from the literature, which suggest that humidity and film stress play a contributing role. Such delamination is not observed, however, in related systems, such as CH_3CN discharges. The exploration of these dramatic differences in delamination behavior focuses on the possible contributions of hydrocarbon species and ion bombardment during deposition. Early results from these studies suggest that the presence of Br may be a critical factor, and possible directions for future studies are suggested.

7.1 Introduction

As discussed in Section 1.1, studies of a-CN_x deposition in PECVD systems often focus on precursor mixtures, such as CH_4/N_2, which allow independent control over C and N densities in the gas phase. Previous results from our lab highlight the relatively high surface reactivity of CN radicals in CH_4/N_2 discharges,[1] but the chemical complexity of these mixed systems limits the confidence with which one can establish the contribution of CN radicals to the deposition process. In an effort to alleviate some of this ambiguity, much of the work in this dissertation has focused on single source precursors as a means of understanding the deposition chemistry in greater detail. Results presented in Chapter 4 extend our results from mixed systems to the study of CN in CH_3CN discharges; similarly high reactivities were observed, and accompanying deposition studies suggest that these surface reactions favor the incorporation of CN during film deposition. Chapter 6 included BrCN as an alternative precursor system for CN generation, and results from those studies were used to develop our understanding of the relationship between the internal energy and surface reactivity of CN.

BrCN presents an interesting opportunity to extend our studies of a-CN_x deposition for several reasons. Aside from the substantially elevated CN rotational temperatures we observe in BrCN plasmas, Chapter 6, studies from the literature suggest that BrCN may generate some rarely-observed quartet electronic states of gas phase CN,[2,3] which could, in turn, affect their incorporation into a-CN_x films.[4] In addition, BrCN is well-suited to the reductionist approach we have taken to studying a-CN_x systems as it allows observation of CN radical behavior in the absence of other depositing species, such as H or CH_x species.

Because CN is the primary deposition species in BrCN discharges, it becomes feasible to deposit a-CN_x materials that do not contain H. Such films have been shown to exhibit substantially different microstructures and mechanical properties;[5-8] however, these films are predominately obtained by sputtering graphite in a N_2 atmosphere, and reports of the formation of H-free a-CN_x by PECVD are few.[8,9] Thus, it becomes clear that there is much to be learned from the exploration of PECVD processes in BrCN discharges.

This chapter presents initial results from our investigation of a-CN_x depositions in systems containing BrCN. Adhesion of the deposited film to the underlying substrate has proven to be an important issue with these materials; given the clear implications of film adhesion in commercial applications, our exploratory work has focused on evaluating two hypotheses (discussed below) to explain changes in film adhesion behavior.

7.2 Results and Discussion

Our observations of films deposited in 100% BrCN discharges indicate that, when the films are exposed to atmosphere, they tend to delaminate from the underlying substrate and become visibly rougher. Scanning electron microscopy (SEM) was used to obtain a more detailed picture of the film morphology following delamination, and the micrographs in Figure 7.1, corresponding to films deposited in a 100% BrCN plasma (100 mTorr, 50 W), show that the delaminated areas of the film have buckled into ridge-like structures. The time required for delamination is observed to decrease at longer deposition times, and, as comparison of Figures 7.1a and 7.1b shows, delamination ridges formed at longer deposition times (i.e., for thicker films) are substantially larger.

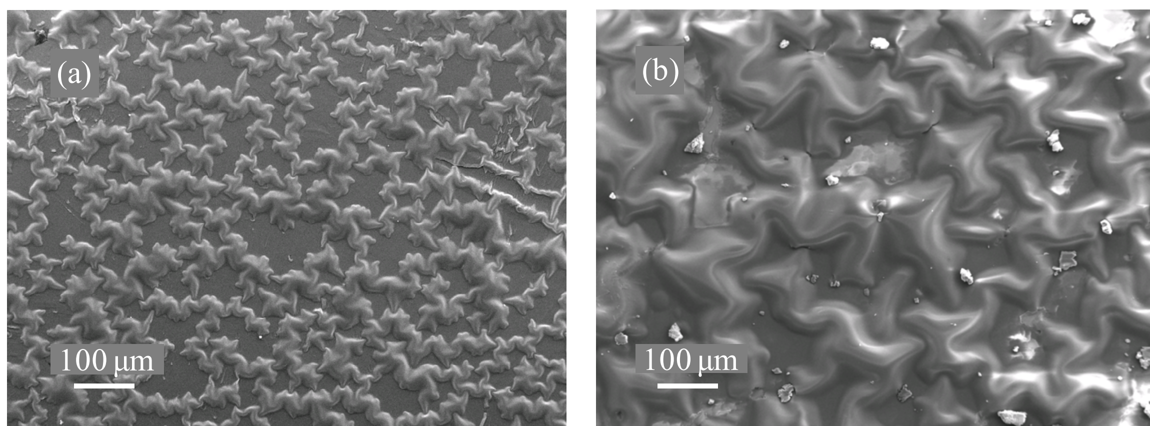

Figure 7.1 SEM micrograph of CN_x film on a KBr pellet after exposure to atmosphere. The films were prepared in 100% BrCN plasma (100 mTorr, 50 W) with deposition times of (a) 20 min and (b) 60 min.

This type of delamination behavior has been observed by other researchers, not only in the deposition of carbon nitride materials,[10] but for boron nitride as well.[11] These studies highlight the role of both humidity and compressive material stress in bringing about delamination. Peponas et al. employed infrared absorption spectroscopy measurements to suggest that delamination involves chemical reactions between H_2O and isocyanate (R–C=N=O) groups at the film-substrate interface.[12] Although this type of absorption spectroscopy constitutes a bulk characterization technique and thus does not provide conclusive evidence of this type of interfacial reaction, the data show that the process of delamination is not simply a mechanical phenomenon, but involves chemical changes as well.

Another notable aspect of both the boron nitride and carbon nitride studies is that they deal with materials deposited by sputter coating; our observation of the same behavior in PECVD systems thus suggests that there are some basic chemical similarities between films deposited with the two deposition methods. Interestingly, however, we do not observe delamination of films deposited in CH_3CN plasmas. This is illustrated by the phase contrast microscope images shown in Figure 7.2. Contrast in these images arises from changes in the refractive index or optical path of light reflected from the underlying substrate, and the ridges formed by the delaminated film become very apparent. The film deposited in 100% CH_3CN is not delaminated and has a uniform appearance throughout the field of view, Figure 7.2a, whereas the film deposited in 100% BrCN is very clearly delaminated, Figure 7.2b. Benlahsen and coworkers have characterized the cross-sections of delamination ridges like these to extract information about the mechanical stress in the material.[10] In our preliminary studies, however, delamination was simply

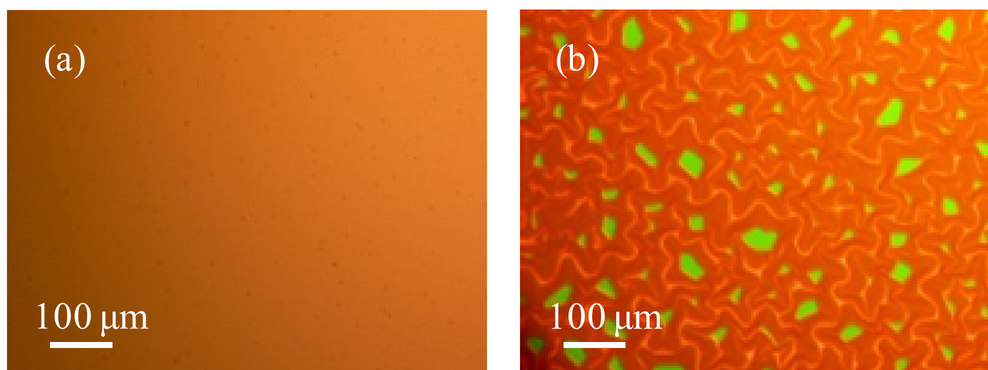

Figure 7.2 Phase contrast microscope images of films deposited for 40 min in (a) 100% CH_3CN and (b) 100% BrCN. In each case, total gas pressure = 100 mTorr and rf power = 50 W.

used as a binary indicator of film behavior.

A more quantitative characterization of these materials was pursued using FTIR absorption spectroscopy, and the resulting absorption curves for films deposited on KBr pellets are shown in Figure 7.3. The absorption curve corresponding to a 100% CH_3CN plasma comes from deposition studies discussed in Chapter 4. In those studies, absorption features in the region of 1500 cm^{-1} are assigned to C=N stretching and CH_x bending modes, and similar features are apparent in Figure 7.3 for the films deposited in 100% BrCN. Similarly, the broad absorption centered near 3400 cm^{-1} is visible in both spectra, though it is somewhat obscured by overlapping peaks in the 100% CH_3CN film. This absorption feature was assigned to C=NH in Chapter 4, but it is associated with OH stretching in the work of Benlahsen and coworkers.[12] Further studies are needed to resolve this discrepancy, but this absorption feature may prove to be useful in understanding the effects of H_2O on delamination behavior. The absence of NH and sp^3 CH_x absorption in the BrCN films is not surprising as we do not expect to have hydrogen in the discharge, but the lack of conjugated C=N absorption in the BrCN film is notable, as this is indicative of differences in the films' microstructures. Lastly, it is important to note that the BrCN absorption curve in Figure 7.3 was measured after film delamination, and may not accurately portray the composition and structure of the virgin material.[12] Further investigation of film delamination focused on establishing fundamental connections between the behavior of films from the different systems, and as the composition and morphology of pressed KBr pellets are somewhat unpredictable, Si wafers were used as substrates for the remainder of the studies.

One of the inherent conclusions in the work of Benlahsen and coworkers is that

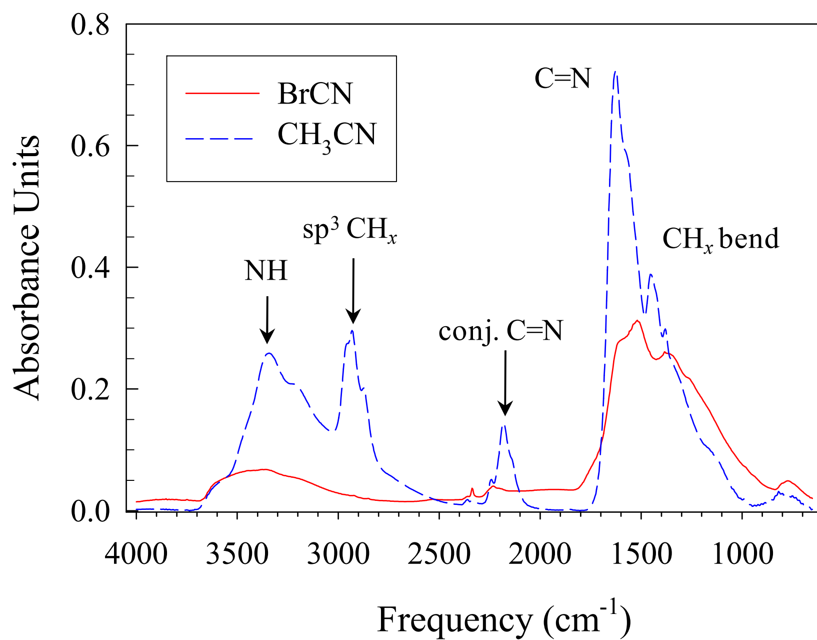

Figure 7.3 Corrected transmission FTIR spectra of film deposited for one hour on a KBr substrate in 100% BrCN (solid line) and 100% CH_3CN (dashed line).

the material is porous enough to allow the diffusion of water vapor to the film-substrate interface, and these researchers suggest that this property arises because the incorporation of CN leads to a high density of terminating functional groups in the film network.[10] Indeed, the films we deposited in BrCN plasmas delaminate more quickly when placed in a humid environment. Moreover, we find evidence of the diffusion of water through the material in optical micrographs like the one in Figure 7.4. Here, a delamination "island" is observed in the lower-left corner of the image, indicating that the porous structure of the film allows delamination to proceed not only from the corners and edges of the substrate but in isolated regions of the film as well.

With this in mind, one of our hypotheses for why film adhesion differs so dramatically in BrCN and CH_3CN discharges was that the films deposited in BrCN are less cross-linked (i.e., have a higher density of terminating functional groups) than films deposited in CH_3CN. Given the composition of the two precursors, we predicted that the presence of CH_x and atomic H might be responsible for differences in the film properties and used mixtures of BrCN and CH_4 to mirror the gas phase composition in CH_3CN discharges. Indeed, we find that films deposited in 100% BrCN plasma are etched effectively in a 100% H_2 plasma. Additional evidence of the effects of both CH_x and H can be found in mechanistic studies of diamond-like carbon (DLC) deposition. Von Keudell and coworkers[13] have shown that atomic H can abstract terminating H atoms from the surface of a growing film to create active sites; the presence of these active sites then promotes cross-linking as additional precursors (particularly CH_3) arrive at the growth front. The observation of CH_x^+ and H* in CH_3CN plasmas (see Sections 5.2 and 4.2, respectively) along with the abundance of unsaturated C≡N bonds would seem to

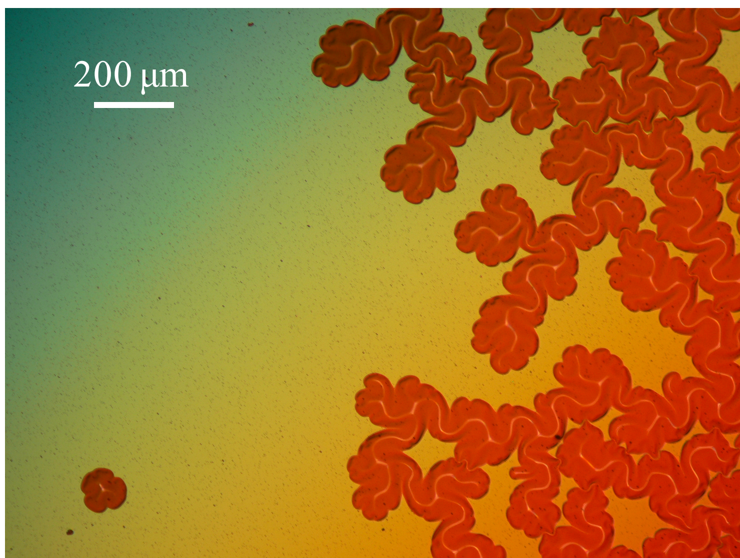

Figure 7.4 Phase contrast microscope image of CN_x film deposited on Si in a 100% BrCN plasma (100 mTorr, 50 W) for 40 min.

favor such a mechanism in a-CN_x deposition as well. Indeed, the same strategy was shown by Kim et al. to improve the adhesion of carbon-containing boron nitride (BN:C) materials obtained by PECVD, with reductions in both the compressive stress of the material and its susceptibility to humidity.[14]

This does not appear to be the case in our systems, however, as shown by the optical micrograph in Figure 7.5a of a film deposited in a plasma containing equal partial pressures of BrCN and CH_4. Clearly, delamination has occurred, indicating that the film remains porous enough to allow diffusion of water vapor into the film. Such images suggest that the presence of hydrocarbons and atomic H does not sufficiently alter the deposition chemistry so as to prevent film delamination.

An alternative hypothesis to explain the cause of the delamination behavior focuses on the influence of ion bombardment during deposition. The densification of CVD films subjected to ion bombardment has been studied extensively,[15-17] and it may be that the porosity of films deposited in BrCN discharges arises, at least in part, as a result of milder ion bombardment conditions relative to CH_3CN plasmas. The possibility of milder ion bombardment conditions in BrCN plasmas may be justified based on the presence of electronegative Br. This is illustrated by the work of Ito and coworkers, who reported dramatic decreases in electron density upon the addition of BrCN to Ar discharges.[18] Thus, if atomic Br scavenges free electrons, the ensuing decrease in electron density might be accompanied by decreases in the positive ion density and/or sheath potential, leading to a lower energy flux at the surface. Although plasma characteristics in electronegative plasmas are quite complex[19-24] and the model used here probably represents an oversimplification, it provides a means of exploring the effects of

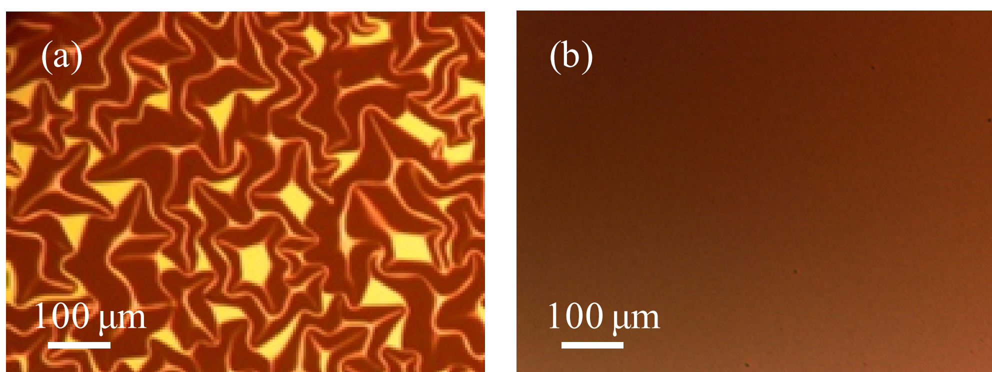

Figure 7.5 Phase contrast microscope images of films deposited for 40 min in (a) 1:1 $BrCN/CH_4$ and (b) 1:1:1 $CH_3CN/BrCN/CH_4$. In each case, total gas pressure = 100 mTorr and rf power = 50 W.

gas phase Br-content on a very basic level. Notably, deposition of a-CN_x in the presence of halogens has also been investigated by Ricci et al.[8] They studied deposition in CH_4/N_2 discharges to which small amounts (≤ 5% of the total flow rate) of Cl_2 were added to scavenge hydrogen. Although they report changes in the physical properties and composition of the deposited films, they do not provide an explanation for how Cl_2 addition causes these changes.

To explore the hypothesis that Br-content is responsible for the delamination of these films, mixtures of gas phase precursors were used according to a simple model that allows for variation of the effective Br-content in the gas phase. Specifically, the precursors CH_3CN, BrCN, and CH_4 were each considered in terms of the number of equivalents of Br, CH_x, and CN they each contribute to the discharge. A list of the different precursor mixtures used in this study is shown in Table 7.1. As shown, the CH_x/CN ratio is the same for each mixture, and the relative amount of Br varies. Films deposited in each mixture were characterized with variable angle spectroscopic ellipsometry (VASE) to extract information about the film thickness and optical properties.

The growth rate data in Table 7.1 were calculated based on the film thicknesses and deposition times. A significant decrease in growth rate is observed as the relative equivalents of Br increase from 0 to 0.5; beyond this point, the growth rate is essentially unchanged within experimental error. This suggests that the mere presence of Br in the discharge is enough to alter the deposition behavior significantly.

Optical band gaps of these films were characterized in terms of the Tauc gap, E_{Tauc}, as extracted from the VASE data (details on this analysis can be found in

Table 7.1 a-CN_x film properties and delamination behavior as a function of Br-content.

Partial Pressure (mTorr)			CH_x:CN:Br	Growth Rate (nm/min)	Tauc Gap, E_{Tauc} (eV)	Delami-nation[a]
CH_3CN	BrCN	CH_4				
100	--	--	2:2:0	31 ± 4	1.5 ± 0.4	N
60	20	20	2:2:0.5	15 ± 2	2.7 ± 0.2	--
33	33	33	2:2:1	13 ± 1	2.9 ± 0.2	N
14	43	43	2:2:1.5	9 ± 2	2.5 ± 0.1	--
--	50	50	2:2:2	13 ± 2	1.2 ± 0.2	Y

[a]Presence of delamination was empirically determined from CN_x films deposited for 40 min in 100 mTorr, 50 W plasmas of the specified compositions.

Appendix A). The resulting data, Table 7.1, suggest that E_{Tauc} is highest for the three-component mixtures, which have similar E_{Tauc} values. Based on published studies of the optical properties of a-CN_x,[25-32] it is possible that the trend in E_{Tauc} in Table 7.1 is related to changes in the N-content and microstructure of the material. However, additional data are needed in order to establish this trend more conclusively.

As mentioned above, deposition of thicker films in100% BrCN plasmas leads to more rapid delamination, highlighting the role of compressive stress in bringing about delamination. In light of the importance of film thickness, one of the objectives of theVASE measurements in Table 7.1 was to gain some perspective on how growth rate varies with Br-content. The data show that the films deposited in 100% CH_3CN, which never delaminate, are actually the thickest films in the series. Given this trend, it is evident that delamination of the films deposited in 100% BrCN is not simply a consequence of differences in film thickness, and additional factors must be involved. Initial steps have been taken to characterize the effect of Br-content on delamination more directly. Specifically, the behavior of thick films (thickness > 500 nm) was compared for three gas mixtures selected from Table 7.1: 100% CH_3CN, 100% BrCN, and an intermediate mixture yielding CH_x:CN:Br = 2:2:1. As discussed above, films deposited in 100% CH_3CN never delaminate, whereas films deposited in 100% BrCN consistently delaminate (for sufficient film thickness) upon exposure to atmosphere. Figure 7.5b shows an optical micrograph for the intermediate case; as can be seen from the image, the film has not delaminated, and this holds true even when the film is placed under humid conditions (on a watchglass in a closed jar containing a moist sponge). This

is a promising result in that it suggests that films with thicknesses on the order of several hundred nm can be deposited in the presence of Br without subsequent film delamination.

Given the aforementioned complexities associated with introducing an electronegative species such as Br into a plasma discharge, additional studies were also carried out to examine the effects of ion bombardment on a more fundamental level. Specifically, films deposited in a 100% BrCN plasma were subjected to a 10 min post-deposition treatment in a 100% N_2 plasma. The thickness and composition were then characterized using VASE and XPS, respectively, and the results were compared to control data for films deposited in a 100% BrCN plasma without post-deposition treatment in a N_2 plasma. For post-deposition treatment, the plasmas were situated in the rf coil region to promote ion bombardment of the film, and the choice of N_2 as a feed gas in these treatments was made in the interest of minimizing N loss from the films, which might result from the use of a heavier bombarding species such as Ar.

Generally speaking, mild ion bombardment causes densification of plasma polymers, giving way to sputtering as the ion bombardment conditions becomes more severe.[17,33,34] In our studies, post-deposition N_2 plasma treatment at an rf power of 100 W caused the visible fringence patterns of the as-deposited film to diminish and eventually disappear; subsequent analysis by XPS confirmed that the film had been sputtered away, leaving behind a surface composed primarily of SiO_2 with trace amounts of C, N, and Br. Based on these results, post-deposition treatment at 50 W was expected to yield a film thinner than the original but with a denser top layer due to ion bombardment. However, as the VASE data in Table 7.2 show, post-deposition treatment in a 50 W N_2 plasma actually caused the film thickness to increase by ~100 nm. This

Table 7.2 CN_x film properties with and without N_2 plasma treatment.

Conditions	Thickness (nm)	N/C
no post-treatment	214 ± 18	0.71 ± 0.02
10 min post-treatment[a]	211 ± 8 + 112 ± 36	0.97 ± 0.08

[a]Post-treatment was performed in a 100 mTorr, 50 W, 100% N_2 plasma.

was confirmed by cross-sectional SEM, Figure 7.6, and suggests that the 50 W post-deposition treatment favors sputtering and/or chemical etching[35] of materials from the reactor walls and their re-deposition on the original film. The demarcations between different layers are visible in Figure 7.4, giving thicknesses within experimental error of the VASE data. Notably, XPS data show an increase in the N/C ratio following post-deposition treatment, suggesting that some additional N incorporation occurs during re-deposition or upon exposure to atmosphere.

7.3 Summary and Future Work

In this work, the delamination of films deposited in plasma discharges containing BrCN was reported. Examination of similar phenomena in the literature suggests that this behavior is largely a result of H_2O diffusion through voids in the films; our attempts to understand this behavior therefore focused on two approaches to controllably altering the film microstructure. The first approach involved the introduction of hydrocarbons (in the form of CH_4) into the discharge, with the intention of promoting cross-linking (and thereby reducing porosity). Ensuing deposition studies, however, suggested that this approach did not prevent delamination of the film from the underlying substrate.

The second approach focused on investigating the effects of ion bombardment on deposition through (a) variation of the effective Br-content in the discharge and (b) post-deposition treatment of a-CN_x films in a 100% N_2 plasma. Treatment of the films in N_2 plasmas did not cause densification of the films. Rather, it resulted in sputtering of materials from the reactor walls and continued growth of the films. Although there may be some value in additional studies of the mechanism responsible for this sputtering, it is

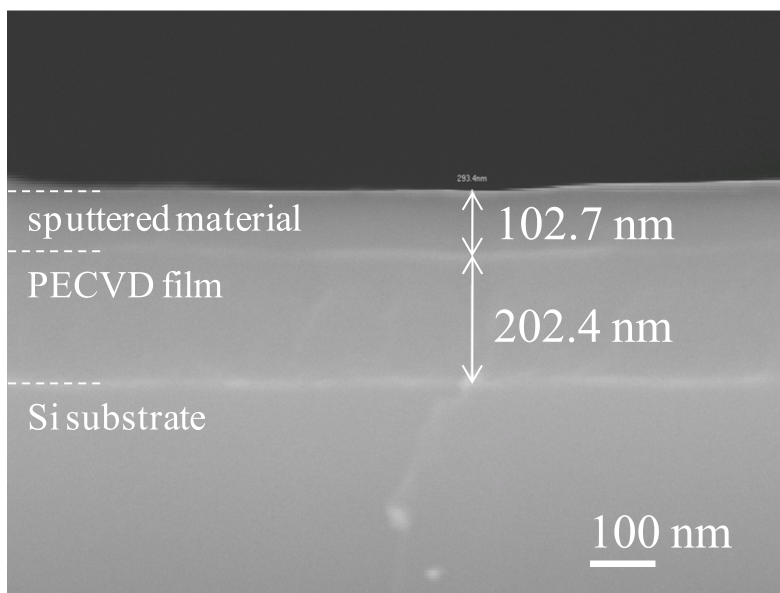

Figure 7.6 Cross-sectional SEM image of CN_x film deposited on Si in a 100% BrCN plasma (100 mTorr, 50 W) for 20 min and subsequently treated with a 100% N_2 plasma (100 mTorr, 50 W) for 10 min.

evident that post-deposition N_2 plasma treatment does not provide an elegant way to isolate the effects of ion bombardment on the density of a-CN_x films. More promising are studies in which gas phase Br-content was varied. These experiments reveal reproducible changes in the growth rate and optical properties of the deposited material, and preliminary results suggest that films deposited in the presence of moderate amounts of Br maintain their adhesion to the substrate, even under humid conditions. Continued development of this research should focus on a few key areas. Most immediately, Table 7.1 should be developed more completely to include additional delamination behavior for thick films as well as the compositional characterization of films deposited in each system.

In the longer term, this research could be extended to include Langmuir probe studies, which could be of great value in clarifying the effects of Br on plasma characteristics in these systems. Although Langmuir probe measurements are especially difficult in systems that deposit materials on the probe filament, it may be possible to obtain relevant information by diluting the species of interest in Ar, as has been done previously in our lab.[36]

Lastly, sum frequency generation (SFG) spectroscopy could be of great value in this research. SFG spectroscopy can be used to probe a number of relevant vibrational modes in this system, including OH, NH, and CN, and the evaluation of SFG signals for these modes under changing humidity conditions might provide direct and conclusive evidence of the chemical interactions leading to film delamination.

7.4 References

[1]D. Liu and E. R. Fisher, J. Vac. Sci. Technol., A **25,** 368 (2007).
[2]H. Ito, Y. Ozaki, K. Suzuki, T. Kondow, and K. Kuchitsu, J. Chem. Phys. **96,** 4195 (1992).
[3]H. F. Schaefer III and T. G. Heil, J. Chem. Phys. **54,** 2573 (1971).
[4]H. Ito, N. Ito, T. Takahashi, H. Takamatsu, D. Tanaka, and H. Saitoh, Jpn. J. Appl. Phys., Part 1 **39,** 1371 (2000).
[5]J. M. Mendez, A. Gaona-Couto, S. Muhl, and S. Jimenez-Sanoval, J. Phys.: Condens. Matter **11,** 5225 (1999).
[6]N. Hellgren, M. P. Johansson, B. Hjorvarsson, E. Broitman, M. Ostblom, B. Liedberg, L. Hultman, and J.-E. Sundgren, J. Vac. Sci. Technol., A **18,** 2349 (2000).
[7]P. Hammer, N. M. Victoria, and F. Alvarez, J. Vac. Sci. Technol., A **16,** 2941 (1998).
[8]M. Ricci, M. Trinquecoste, F. Auguste, R. Canet, P. Delhaes, C. Guimon, G. Pfister-Guillouzo, B. Nvesten, and J. P. Issi, J. Mater. Res. **8,** 480 (1993).
[9]H. Saitoh, H. Takamatsu, D. Tanaka, N. Ito, S. Ohshio, and H. Ito, Jpn. J. Appl. Phys., Part 1 **39,** 1258 (2000).
[10]S. Peponas, M. Guedda, and M. Benlahsen, Solid State Commun. **146,** 78 (2008).
[11]J. Moller, D. Reiche, M. Bobeth, and W. Pompe, Surf. Coat. Technol. **150,** 8 (2002).
[12]S. Peponas, M. Benlahsen, and M. Guedda, J. Appl. Phys. **106,** 013525 (2009).
[13]A. von Keudell, T. Schwarz-Selinger, and W. Jacob, J. Appl. Phys. **89,** 2979 (2001).
[14]K.-B. Kim and S.-H. Kim, J. Vac. Sci. Technol., A **18,** 900 (2000).
[15]A. Amassian, R. Vernhes, J. E. Klemberg-Sapieha, P. Desjardins, and L. Martinu, Thin Solid Films **469-470,** 47 (2004).
[16]J. Vlcek, K. Rusnak, V. Hajek, and L. Martinu, J. Appl. Phys. **86,** 3647 (1999).
[17]A. S. Bakai, A. I. Zhukov, and S. N. Sleptsov, J. Phys.: Condens. Matter **11,** 5681 (1999).
[18]H. Ito, Y. Sato, and H. Saitoh, Jpn. J. Appl. Phys., Part 1 **43,** 7277 (2004).
[19]A. M. Marakhatanov, M. Tuszewski, M. A. Lieberman, A. J. Lichtenberg, and P. Chabert, J. Vac. Sci. Technol., A **21,** 1849 (2003).
[20]G. Franz, J. Vac. Sci. Technol., A **23,** 369 (2005).
[21]M. Li, M. A. Vyvoda, S. K. Dew, and M. J. Brett, IEEE Trans. Plasma Sci. **28,** 248 (2000).
[22]T. E. Sheridan, P. Chabert, and R. W. Boswell, Plasma Sources Sci. Technol. **8,** 457 (1999).
[23]T. H. Chung, Phys. Plasmas **16,** 063503 (2009).
[24]I. G. Kouznetsov, A. J. Lichtenberg, and M. A. Lieberman, J. Appl. Phys. **86,** 4142 (1999).
[25]S. R. P. Silva, J. Robertson, G. A. J. Amaratunga, B. Rafferty, L. M. Brown, J. Schwan, D. F. Fanceschini, and G. Mariotto, J. Appl. Phys. **81,** 2626 (1997).
[26]A. Canillas, M. C. Polo, J. L. Andujar, J. Sancho, S. Bosch, J. Robertson, and W. I. Milne, Diamond Relat. Mater. **10,** 1132 (2001).
[27]C. Godet, G. Adamopoulos, S. Kumar, and T. Katsuno, Thin Solid Films **482,** 24 (2005).
[28]Y. Hayashi, G. Yu, M. M. Rahman, K. M. Krishna, T. Soga, T. Jimbo, and M. Umeno, Appl. Phys. Lett. **78,** 3962 (2001).

[29]M. Jelinek, W. Kulisch, M. P. Delplancke-Ogletree, J. Lancok, L. Jastrabik, D. Chvostova, C. Popov, and J. Bulir, Appl. Phys. A **73,** 167 (2001).
[30]S. E. Rodil, S. Muhl, S. Maca, and A. C. Ferrari, Thin Solid Films **433,** 119 (2003).
[31]N. Tsubouchi, B. Enders, A. Chayahara, A. Kinomura, C. Heck, and Y. Horino, J. Vac. Sci. Technol., A **17,** 2384 (1999).
[32]J. Wei and P. Hing, J. Appl. Phys. **91,** 2812 (2002).
[33]D. W. Hess and D. B. Graves, in *Chemical Vapor Deposition:Principles and Applications*, edited by M. L. Hitchman and K. F. Jensen (Academic Press, San Diego, CA, 1993), p. 385.
[34]M. Nastasi, A. Misra, and J. W. Mayer, in *Materials Processing Handbook*, edited by J. R. Groza (CRC Press LLC, Boca Raton, FL, 2007), p. 1.
[35]P. Hammer and W. Gissler, Diamond Relat. Mater. **5,** 1152 (2006).
[36]J. Zhou, I. T. Martin, R. Ayers, E. Adams, D. Liu, and E. R. Fisher, Plasma Sources Sci. Technol. **15,** 714 (2006).

CHAPTER 8

SURFACE INTERACTIONS OF SO_2 AND PASSIVATION CHEMISTRY DURING ETCHING OF Si AND SiO_2 IN SF_6/O_2 PLASMAS

This chapter contains data from a full paper published in the *Journal of Vacuum Science & Technology A*. The manuscript was written by Joshua M. Stillahn and edited by Jianming Zhang and Ellen R. Fisher. A substantial portion of the data was collected by Jianming Zhang; Joshua M. Stillahn corroborated these data and performed additional surface characterization. The studies herein focus on the influence of SO_2, both in the gas phase and at surfaces, on the evolution of gas phase species during Si and SiO_2 processing in SF_6/O_2 plasmas. A variety of diagnostics are used to show that SO2 promotes the liberation of free F by inhibiting the reformation of SO_xF_y ($y > 1$) species during breakdown.

8.1 Introduction

In semiconductor manufacturing, the selective etching of materials is often achieved through the careful application of plasma discharges; the resulting etch architectures form complex systems of electrical components that are used in nearly all modern electronic devices. The progression of semiconductor technology and the pressure to meet the demands of industry roadmaps has led to reduced critical dimensions and lower tolerance for contamination and structural non-uniformity. Much effort is therefore dedicated to improvements in these areas.

Sulfur hexafluoride (SF_6) has been used as an etchant for Si as it produces copious amounts of atomic fluorine, a reactive etching species. One of the downsides to using SF_6 in etch processes as well as a gaseous insulator,[1,2] however, is that it is an environmental pollutant with a very high global warming potential.[3] Another limitation of SF_6 in etch processes is that it etches Si isotropically and therefore does not provide the necessary level of control over feature size.[4,5] This was first addressed with the development of the Bosch process, in which short periods of isotropic SF_6 etching are punctuated by a passivation step where an etch-resistant fluorocarbon material is deposited. Subsequent etching takes place primarily at the bottom of the etch feature, where ion bombardment exposes fresh Si. Extrapolation of these cycles leads to an etch process that is collectively anisotropic. Although this process has been used successfully in the semiconductor industry for a number of years, it has some inherent weaknesses, including potential for contamination while switching process chemistries as well as sidewall scalloping, where successive etch steps create periodic undulations in the sidewall profile.

To address these issues and improve etch technology, studies have turned to plasma systems with the potential to etch Si in a continuous, anisotropic manner. Plasma mixtures of SF_6 and O_2, recognized as useful etching systems for many years,[6] have seen increased interest since the development of cryogenic etching by Tachi et al.[5] This process involves cooling the substrate to cryogenic temperatures to promote effective competition between etching by atomic F and the formation of a siliconoxyfluoride (SiO_xF_y) passiviation layer, which leads to anisotropic etching. The delicate balance between etching and passivation depends critically on the relative contributions of important gas phase species, and although the etch behavior of atomic F has been studied extensively, the chemical details that govern the formation of the passivation layer are still unclear.

As a component of this research problem, it is important to consider the contributions of different gas phase species generated in the plasma. For example, sulfur dioxide (SO_2) is generated in SF_6/O_2 plasmas through fragmentation and recombination reactions. As an oxygen-containing species, SO_2 has the potential to promote some of the same reactions as O_2, and it can produce similar etch behavior when used as a replacement for O_2 in mixtures with SF_6.[7] It is worth noting that, in its own right, SO_2 has been considered as a useful etchant of polymeric materials in pattern transfer steps for multilayer resist technologies.[8-11] Although these systems proved to be effective for both etching and sidewall passivation of the polymeric resist material, the formation of sulfides on copper interconnects emerged as a deleterious side effect.[12] This highlights the importance of obtaining a chemically specific understanding of how reactive species behave in etch systems.

In this work, we examine the fate of SO_2 during processing in SF_6/O_2 discharges using the imaging of radicals interacting with surfaces (IRIS) method, along with fundamental aspects of passivation chemistry in these systems. Si and SiO_2 substrates are used as model systems and allow comparison to reports from the literature; however, F-containing discharges have been used for processing a number of other semiconductor and dielectric materials as well, including Ta_2O_5,[13,14] HfO_2,[15-17] GaAs,[18,19] and SiC.[20,21] Our studies on Si/SiO_2 substrates employ a host of diagnostic techniques to characterize gas phase species, surface properties, and plasma-surface interactions. The results of these studies illustrate the influence of oxygen on breakdown and recombination processes in SF_6/O_2 plasmas and provide information for further refinement of models describing the gas phase chemistry in these systems.

8.2 Results

A. Etch Rate and Surface Characterization. Figure 8.1a shows the etch rates of Si and SiO_2 and the corresponding etch selectivity as a function of O_2 addition. At P = 50 and 100 W, the Si etch rate decreases with increasing O_2 addition. Si etch rates are notably higher at 100 W, and a slight increase in etch rate is observed for Q_{O_2}= 0-1 sccm. The etch rate of SiO_2, on the other hand, is less than 30 nm/min under all conditions and appears to be insensitive to changes in O_2 flow rate. As a result, the etch selectivity closely follows trends in the Si etch rate, reaching a maximum value of about 55 at Q_{O_2}= 1 sccm. Figure 8.1b shows the etch rates of Si and SiO_2 and the etch selectivity as a function of P at Q_{O_2}= 10 sccm. The Si etch rate increases monotonically with P, whereas

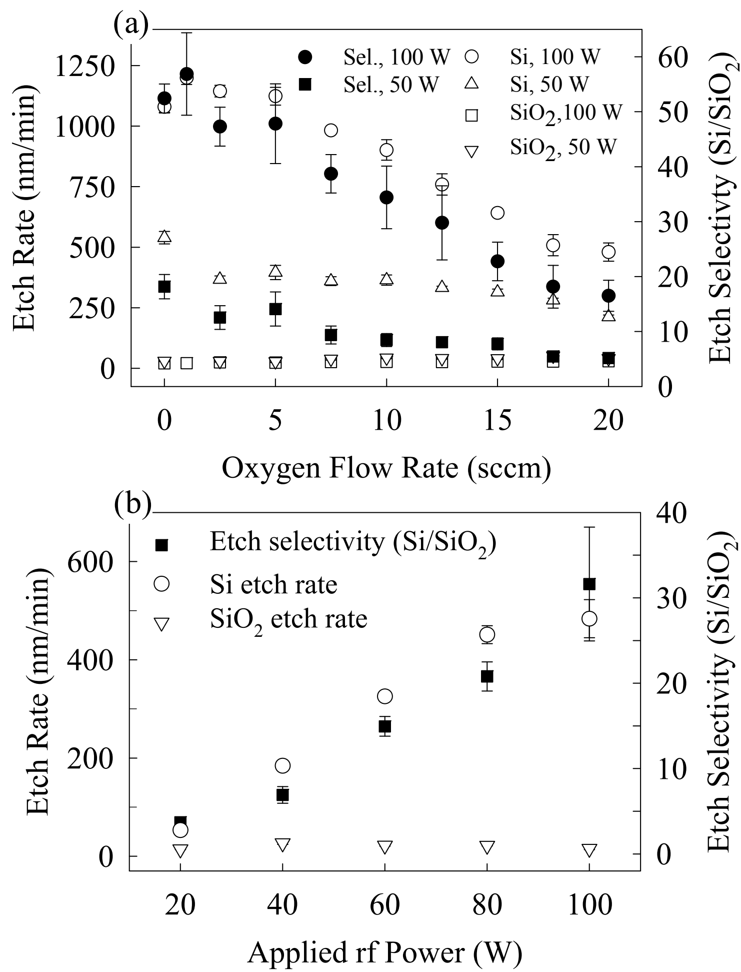

Figure 8.1 Si and SiO_2 etch rates and Si/SiO_2 etch selectivity as a function of (a) O_2 flow rate with 10 sccm SF_6, P = 50 and 100 W and (b) applied rf power for Q_{O_2}= 10 sccm.

the SiO_2 etch rate is insensitive to changes in P. As with the O_2-dependence, this leads to a trend in etch selectivity that mirrors the trend in Si etch rate.

Figure 8.2 shows SEM images for Si and SiO_2 substrates after a 5 min etch in a 50 W plasma with Q_{O_2} = 10 sccm using a range of mask sizes. In each case, mask pattern transfer is evident in the reproduction of the grid pattern of the copper mask. This is true for both the 400 mesh, which has 37 μm holes, and the 2000 mesh with smaller holes of 7.5 μm. Etch rate measurements from Figure 8.1 suggest that the etch pits are deeper on the Si samples than on SiO_2, with respective etch depths of roughly 1.1 and 0.2 μm. These samples were primarily used to obtain values for the etch rate under different conditions, but the observed pattern transfer demonstrates that the copper mask is in sufficient physical contact with the substrate to allow comparison between etched and masked surfaces. The effects of differing etch rates and processes can also be seen in the high resolution SEM images of the exposed Si and SiO_2 substrates shown in Figure 8.3. The etched Si surface is significantly rougher and has more extensive pitting than the SiO_2 surface. It is clear that the etch process is not uniform, and the observed change in morphology may be influenced by micromasking[22] by contaminant particles or by material sputtered from the reactor components.

To provide additional context for SF_6/O_2 data acquired in our reactor, Si and SiO_2 etch rates were also measured for some alternative F-containing etch discharge systems under similar processing conditions. The resulting values, along with the corresponding etch selectivities, are given in Table 8.1. Data in the table show that the SF_6/O_2 system gives a lower Si etch rate than NF_3/O_2. The O_2 dependence of the etch selectivity in the NF_3/O_2 system (not shown) is similar to the trend in Figure 8.1a; however, unlike the

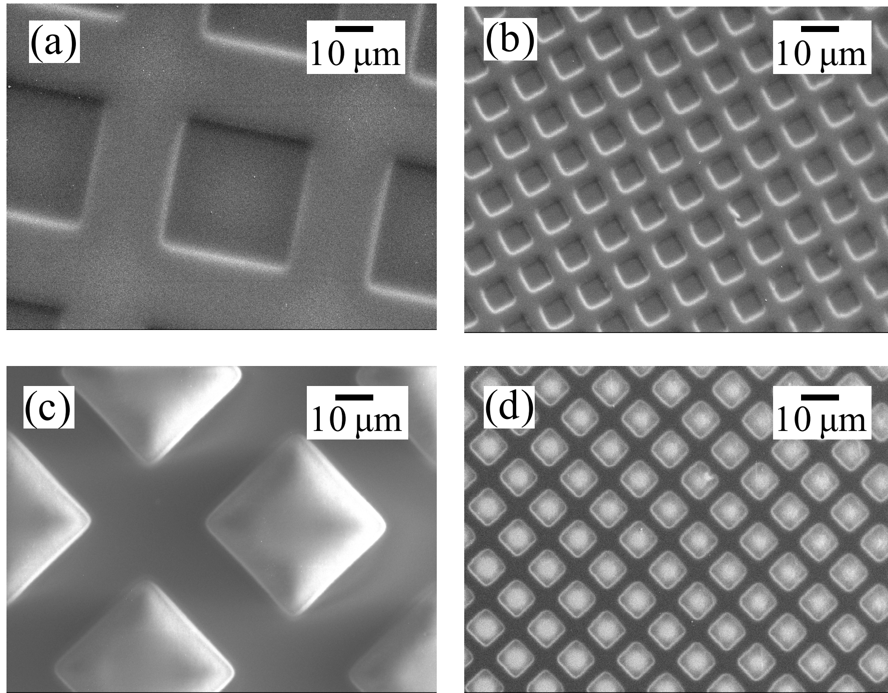

Figure 8.2 SEM images of Si wafers (top row), and SiO_2 wafers (bottom row) etched 5 min with Q_{O_2}= 10 sccm and P = 50 W. The substrates in (a) and (c) were masked with 400 mesh Cu grid, and those in (b) and (d) were masked with 2000 mesh Cu grid. Scale bar in each image is 10 μm.

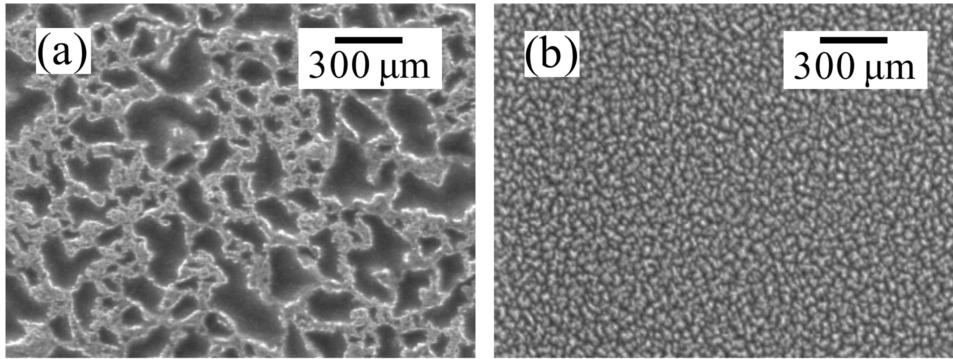

Figure 8.3 SEM images of exposed surfaces of (a) Si and (b) SiO_2 substrates after etching in SF_6/O_2 plasma with Q_{O_2}= 10 sccm and P = 50W. Scale bar in each image is 100 nm.

Table 8.1 Comparison of etch behavior and thermochemistry for F-based discharge systems[a]

System	F Removal Energy (eV)[a]	Si Etch Rate (nm/min)[b]	Selectivity Factor (Si vs. SiO_2)
NF_3/O_2	2.5	580 ± 30	9.8 ± 7
SF_6/O_2	4.0	360 ± 20	8.4 ± 1.2
CF_4/O_2	5.7	25 ± 2	0.6 ± 0.2
C_2F_6/O_2	5.5	17 ± 2	0.9 ± 0.3

[a]Bond energies are calculated from ΔH_f values in Ref. 23 and correspond to the enthalpy of the reaction to remove the first F atom from the parent molecule (e.g., $NF_3 \rightarrow NF_2$ + F). Data acquired for plasmas at P = 50 W, and 10 sccm each of oxygen and the fluorinated etchant.

SF_6/O_2 system, the selectivity in the NF_3/O_2 system arises from increases in the SiO_2 etch rate rather than from decreases in the Si etch rate. In contrast to the SF_6 and NF_3 discharges, both fluorocarbon systems give relatively low Si etch rates and etch SiO_2 faster than Si. Etch rates in these systems increased with *P*, but the selectivity was largely unchanged.

The chemical compositions of Si and SiO_2 substrates were measured by XPS as a function of O_2 addition for 100 W SF_6/O_2 plasmas, Figure 8. 4, to further characterize samples processed in these systems. For both substrates, a significant amount of Al is observed, most probably from sputtering of the Al electrodes during etch processing. Sulfur is also detected under all conditions, but only in trace amounts (<1%). For Si, Figure 8.4a, the most notable trends are the increase in F content and decrease in Si content of the surface with O_2 addition. For the SiO_2 substrates, Figure 8.4b, no significant dependence of elemental composition on O_2 addition to the plasma is apparent, and the O-to-Si ratio is ~2 under all conditions.

B. Gas Phase Characterization and Gas-Surface Interactions. Figure 8.5a shows the normalized F* and O* emission intensities obtained by OES as a function of O_2 addition with P = 50 and 100 W. As noted above, the intensities of F* and O* are normalized to the Ar* signal to compensate for the effect of changes in the electron energy distribution on emission peak intensities. Similar trends are observed in F* intensity for both 50 and 100 W, with emission intensity increasing with O_2 addition up to Q_{O_2}~7.5 sccm and then leveling off; the absolute values for each trend differ, however, with higher *P* corresponding to higher emission intensity. The O* intensity increases linearly with O_2 addition, and appears to be unaffected by changes in *P*. This is

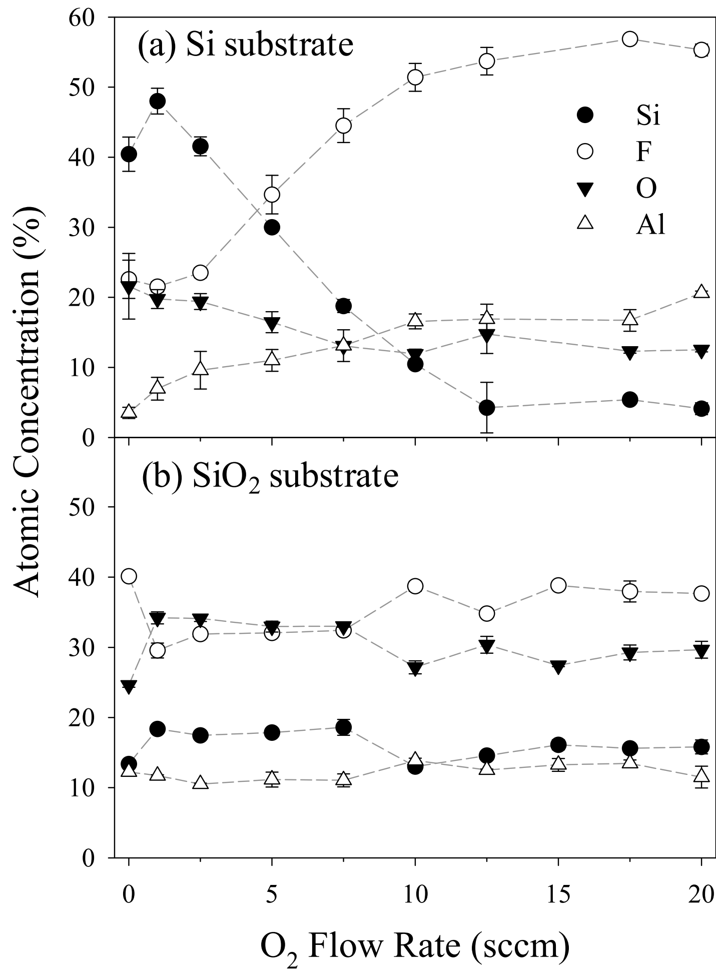

Figure 8.4 Atomic surface composition of Si, F, O, and Al as measured by ex situ XPS for (a) Si and (b) SiO_2 substrates as a function of O_2 addition at 10 sccm SF_6 and P = 100 W.

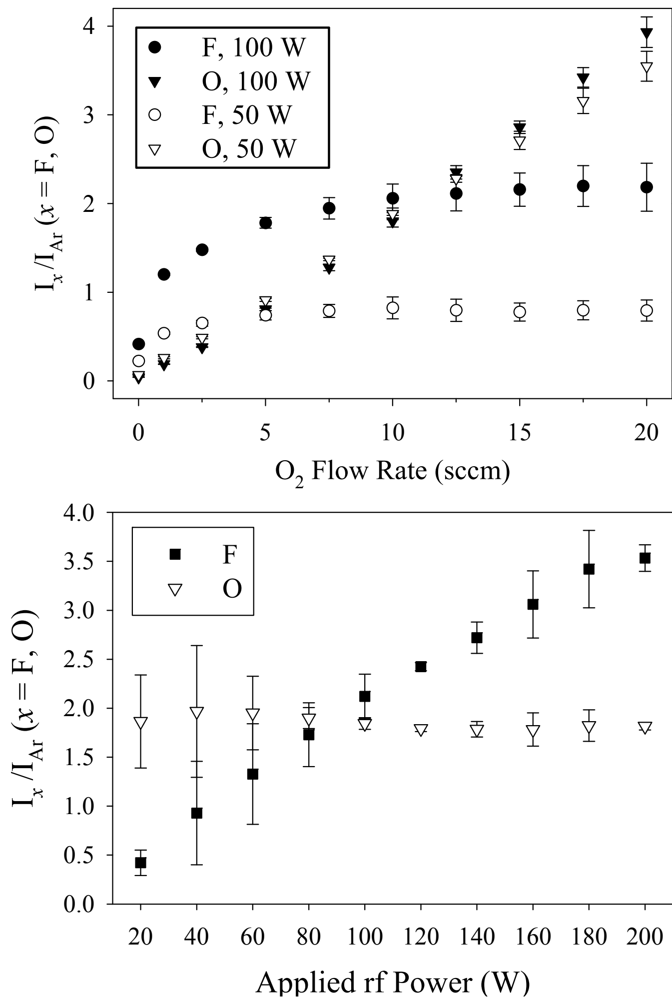

Figure 8.5 Normalized OES intensities of F* (circles) and O* (triangles) in (a) as a function of O_2 addition at 10 sccm SF_6 and P = 50 and 100 W and (b) as a function of P with Q_{O_2} = 10 sccm.

confirmed by the OES intensities of F* and O* as a function of *P* at 10 sccm O_2, Figure 8.5b. The O* intensity remains constant and the F* intensity increases linearly with *P*.

Additional characterization of gas phase species was achieved with mass spectrometry. Representative mass spectra are shown in Figure 8.6 for a 50 W discharge of pure SF_6 and for 10 sccm each of SF_6 and O_2. Aside from the dominant SF_x^+ (x = 1-5) peaks, there are also a number of oxide peaks, $SO_xF_y^+$, that emerge upon addition of O_2. Also present are peaks corresponding to SO^+ and SO_2^+ at *m/z* = 48 and 64, respectively, which result from reactions of the parent species, SF_6 and O_2. The signal at *m/z* = 18 suggests the presence of H_2O in the reactor system during data collection and is roughly the same both before and after O_2 addition. Also noteworthy are the peaks at *m/z* = 28 and 44, which are likely due to CO and CO_2, respectively; these may result from the volatilization of carbon contaminants in the reactor with addition of O_2 to the discharge. For the SF_6/O_2 plasma at P = 100 W, although the overall signals for the SF_x and SO_xF_y species produced increase, there does not appear to be an appreciable change in the relative amounts of these species.

In light of the many species observed in the mass spectra, we were interested in finding a relatively simple molecule that might provide information about the chemistry that takes place in these discharge systems. The work of Grant et al.[24] indicates that in SF_6/O_2 mixtures, the breakdown of SO_2 requires a relatively large amount of energy and that SO_2 therefore represents a stable end product of breakdown and recombination processes in the gas phase. In addition, it has been suggested that, in SF_6/SO_2 discharges, SO_2 contributes to passivation chemistry through surface reactions.[7] For these reasons, SO_2 was targeted for further study using LIF methods. Figure 8.7 shows a representative

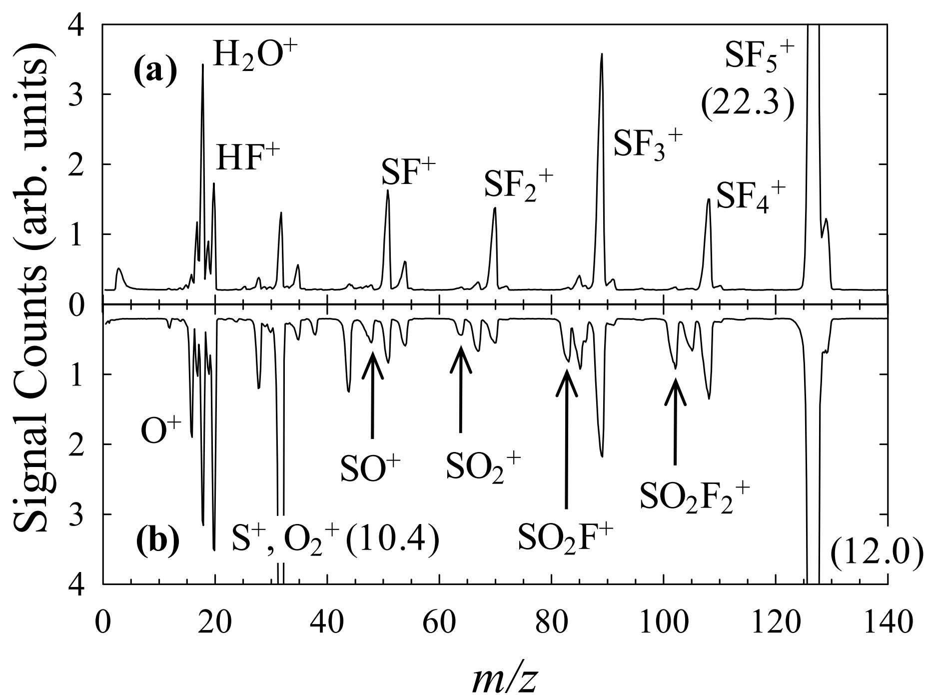

Figure 8.6 Mass spectra of neutral species in (a) for 10 sccm SF_6 at P = 50 W with no O_2 addition and in (b) for 10 sccm SF_6/10 sccm O_2 at P = 50 W (inverted for clarity). For peaks that extend beyond the figure boundaries, maximum intensities are given in parentheses.

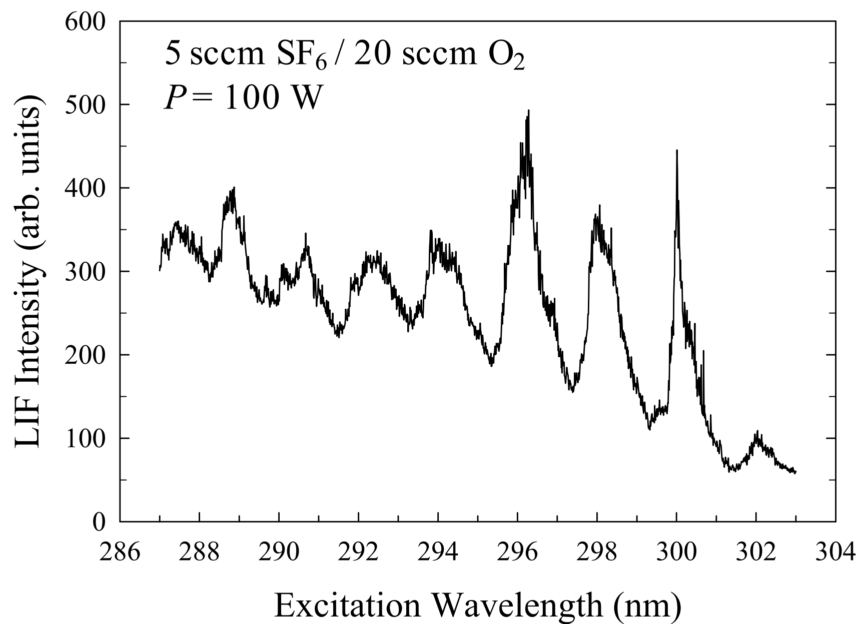

Figure 8.7 Fluorescence excitation spectrum of SO_2 for 5 sccm SF_6/20 sccm O_2 at P = 100 W.

LIF excitation spectrum obtained at P = 100 W with SF_6 and O_2 flow rates of 5 and 20 sccm, respectively. Similar spectral data are obtained in a flow of neutral SO_2 gas, and we attribute the fluorescence signal in Figure 8.7 to SO_2. Although the complete assignment of complex rovibronic features in this spectrum has been studied by other groups,[25-28] such analysis is beyond the scope of the current work, and we propose only that the observed fluorescence originates from excitation of the Ã←X̃ transition. This assignment is supported by the observation of LIF signal that persists for several tens of μs, characteristic of the long-lived SO_2(Ã) state.[29,30] Based on the spectral data in Figure 8.7, the laser was tuned to the intense fluorescence feature at λ = 296.25 nm for the measurement of relative number density and surface scattering of SO_2.

Figure 8.8a shows the relative SO_2 LIF intensities in SF_6/O_2 plasmas as a function of O_2 flow rate for P = 100 and 200 W. These data represent a compilation of LIF data that were collected at different times. To compensate for changes in laser power and other issues that may have affected the measured intensities, corrections were made based on six data points collected at identical P and Q_{O_2}. Weighted averages and standard deviations were calculated for these points, whereas the errors for the remaining points come from the simple mean and standard deviation using several data sets. At 100 W, the SO_2 signal in Figure 8.8a increases over Q_{O_2}= 0-1 sccm but then plateaus at higher Q_{O_2}. This is dramatically different from the trend at 200 W, where the SO_2 signal is greater than at 100 W at all Q_{O_2} and increases nearly linearly with O_2 addition. The sharp contrast in the dependence of these data on O_2 addition is further explored in Figure 8.8b, where the SO_2 LIF signal is plotted as a function of P for a plasma with Q_{O_2}= 10 sccm. As in Figure 8.8a, these data represent a compilation of data collected at different times.

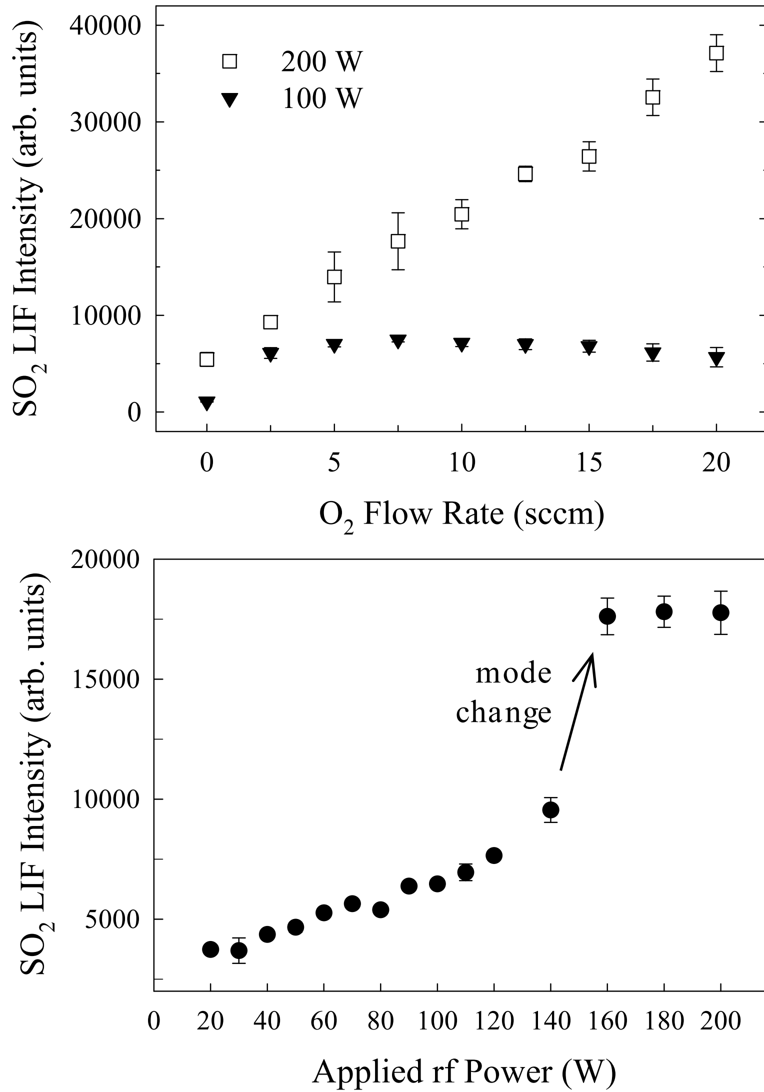

Figure 8.8 Relative LIF intensity of SO_2 (a) as a function of O_2 addition at 10 sccm SF_6 and P = 100 and 200 W and (b) as a function of P with Q_{O_2} = 10 sccm; arrow denotes conditions where a change in coupling mode is observed.

Here, the data exhibit a steady increase with P up to 140 W. Above 140 W, the glow of the discharge became more intense and the SO_2 signal increases sharply, reaching a plateau for P = 160-200 W. This type of mode transition has been observed in our systems previously[31] and has been studied in detail by several groups.[32,33] At rf powers below the transition point, discharges exhibit lower electron densities and are thought to have a large degree of capacitive coupling. At powers above the transition point, higher electron densities and photoemission are observed, and the discharge is dominated by inductive coupling. The effect of this mode change on the data in Figure 8.8a is discussed in more detail below.

To gain some insight on the fate of gas phase SO_2 in these systems, the surface scattering of SO_2 on Si and SiO_2 surfaces during plasma etching was measured using the IRIS technique. As described above in the experimental section and in previous work,[34-37] the ICCD images we collect are converted to cross sectional data and fit with a numerical simulation to provide surface scattering coefficients. IRIS data were collected under a variety of conditions and the resulting $S(SO_2)$ values obtained from simulation of cross sectional data are listed in Table 8.2. The P dependence of $S(SO_2)$ was characterized for Si and SiO_2 for a discharge with Q_{O_2}= 10 sccm, and the data suggest that, for both Si and SiO_2, SO_2 scatters with near-unity probability under all conditions. Similar results are obtained from measurement of $S(SO_2)$ as a function of O_2 content in a 200 W plasma, with nearly all values approaching S = 1 within experimental error. It is possible that these scatter coefficients are affected to some degree by competition between different gas phase species in SF_6/O_2 discharges, and in the interest of exploring SO_2 reactivity in these systems further, $S(SO_2)$ was measured in a discharge of pure SO_2

Table 8.2 $S(SO_2)$ for using SF_6/O_2 plasmas, SO_2 plasmas, and non-ionized SO_2 gas.

10 sccm SF_6/10 sccm O_2			**20 sccm SO_2**		
***P*(W)**	**Si**	**SiO_2**	***P*(W)**	**Si**	**SiO_2**
100	0.93 ± 0.30	1.10 ± 0.30	0	1.06 ± 0.04	1.04 ± 0.04
120	0.93 ± 0.30	0.96 ± 0.30	50	0.98 ± 0.04	1.05 ± 0.06
140	0.90 ± 0.14	1.18 ± 0.20	100	1.07 ± 0.06	1.13 ± 0.10
170	0.92 ± 0.07	1.15 ± 0.30	150	1.08 ± 0.05	1.05 ± 0.13
200	0.94 ± 0.07	0.93 ± 0.15	200	1.10 ± 0.10	1.10 ± 0.11
10 sccm SF_6 *P* = 100 W			**SO_2 with no rf power**		
O_2 Flow (sccm)	**Si**	**SiO_2**	**SO_2 Flow (sccm)**	**Si**	**SiO_2**
5	1.20 ± 0.20	0.90 ± 0.20	5	1.10 ± 0.15	1.35 ± 0.07
7.5	1.22 ± 0.15	1.10 ± 0.15	10	1.14 ± 0.10	1.15 ± 0.04
10	0.94 ± 0.07	0.93 ± 0.15	15	1.08 ± 0.06	1.11 ± 0.05
12.5	0.96 ± 0.15	0.93 ± 0.15	20	1.06 ± 0.04	1.04 ± 0.04
15	1.13 ± 0.20	1.00 ± 0.20			
17.5	1.02 ± 0.20	0.97 ± 0.20			
20	0.92 ± 0.20	0.90 ± 0.30			

gas as a function of P. The results of these measurements, also listed in Table 8.2, indicate once again that SO_2 scatters with near-unity probability on both Si and SiO_2 substrates. Statistically significant deviations from $S = 1$ do start to arise, however, for a neutral flow of SO_2 where no discharge is generated. Here, we again measure scatter coefficients of essentially unity, although some slightly elevated values are also obtained on both substrates. Collectively, the IRIS data suggest that the net surface loss of SO_2 is essentially zero and that SO_2 does not undergo surface reactions during processing.

8.3. Discussion

As noted in the Introduction, SF_6/O_2 plasmas have been used to etch a range of different types of materials; thus, the etch behavior in these systems was initially evaluated based on their selectivity. The etch results presented for SF_6/O_2 processing of Si and SiO_2 indicate a reasonable amount of chemical selectivity between the two surfaces. The etch selectivity of SF_6/O_2 plasmas has been observed before,[6] and although SiO_2 is not believed to be the primary component of sidewall passivation layers in this system, Si/SiO_2 selectivity might be useful for etch processing in cases where photolithography is not practical and SiO_2 is instead used as a mask, as is the case for some solar cell manufacturing processes.[38] Table 8.1 compares the degree of etch selectivity observed in SF_6/O_2 to other fluorine-based etching systems. Although we did not perform extensive experiments with these other systems, it is useful to compare different etch chemistries achieved with a particular plasma reactor system rather than comparing results to systems described in the literature that may have significantly different geometries and/or plasma parameters. The observed etch rates in this series are

somewhat counterintuitive, as one might expect the etch rate to increase with the number of fluorine atoms (the primary etching species) per monomer unit. Instead, NF_3 yields a higher etch rate with three F atoms per precursor molecule than either CF_4, which has four, or C_2F_6 and SF_6, with six each. The thermochemical properties of these etchant gases prove to be more revealing, as the energies required to remove the first fluorine atom from each parent molecule (as calculated from formation enthalpies in Ref. 23) appear to scale more closely with the observed etch rates. Clearly, this is not the only determining factor; in the fluorocarbon systems, the formation of fluorocarbon films also plays a role.[39] In all systems, the etch rates and selectivity often depend on experimental parameters and substrate properties, as seen in published studies.[13-15,17]

The chemical consequences of O_2 additions to our SF_6 discharges are similar to those of Gomez et al.,[40] who also studied SF_6/O_2 systems under non-cryogenic conditions. In both cases, the etch rate of Si in SF_6/O_2 plasmas is negatively correlated to O_2 addition. Decreases in the Si etch rate cause a concurrent drop in the etch selectivity, Figure 8.1, which approaches a value of one (i.e., non-selective etching) for high O_2 content. This trend highlights the contributions of oxygen to Si passivation during etching. Indeed, these oxygen-rich mixtures can be placed in what has been described as an "overpassivation" regime in which the etch passiviation layer forms fast enough that the etch rate is limited even in the presence of ion bombardment.

It has been shown that the SiO_xF_y passivation layer that forms under cryogenic etching conditions is mostly lost as the substrate returns to room temperature,[41] likely due to the formation of volatile SiF_4 species.[42] Contrary to this notion, the results of XPS analysis, Figure 8.4, suggest that under the etching conditions used in this study, a stable

F-containing layer is formed and remains on the surface after processing; such behavior may be advantageous for repeating etch cycles without the regeneration of the passivation layer. Furthermore, it may be possible to remove residual fluorine through post-etch substrate heating.

Although it is considered to be primarily an etching species, it is possible that atomic F also participates in the formation of the SiO_xF_y passivation layer. Here, OES was used to characterize atomic F, as well as atomic O, in the gas phase. As might be expected, the emission signal from atomic O increases with O_2 flow rate. More interestingly, the F emission signal is observed to increase with O_2 flow rate and then plateau above Q_{O_2} ~7.5 sccm. This trend is not unlike the trend in substrate F-content shown in Figure 8.4a for Si processing, supporting the idea that atomic F contributes, either directly or indirectly, to the passivation process. More importantly, these results raise the question of how these contributions might be related to the addition of O_2.

To explore this idea further, mass spectrometry was used to gain a more global perspective on how O_2 addition affects the evolution of gas phase species in these systems. Among the important changes that occur with O_2 addition, Figure 8.6, is the emergence of peaks corresponding to SO, SO_2, and SO_xF_y species. Notably, the presence of mass peaks corresponding to SO_xF_y species highlights the significance of processes like Reaction 8.1 below:

$$SF_2 + O \rightarrow SOF + F \qquad (8.1)$$

Atomic F liberated by these processes is then free to participate in etching. By a similar mechanism, addition of oxygen to SO_xF_y species can lead to the formation of SO_2:

$$SOF + O \rightarrow SO_2 + F \qquad (8.2)$$

As noted above, SO_2 has a relatively high dissociation energy compared to the SF_x and SO_xF_y species generated in these systems.[24] Thus, SO_2 represents a stable end product of breakdown and recombination reactions, and, as suggested by others, SO_2 may act as a sink for sulfur by preventing the reformation of SF_x[7,43] and thereby promoting the liberation of atomic F.

In this scheme, the relative densities of F and SO_2 would be expected to scale similarly, and in the present work, the relative densities of these species were explored with OES and LIF, respectively. LIF data, Figure 8.8, suggest that the SO_2 density increases with power in a near-linear fashion (excluding the effects of the mode change) and, at P = 100 W, exhibit a plateau behavior as a function of O_2 flow rate. The same general features characterize the trends in F* signal in Figure 8.5. Thus, the hypothesis that F* and SO_2 density scale in a similar fashion is valid, and the data collectively point to the importance of two types of reactions:

$$SF_x + e^- \leftrightarrow SF_{x-1} + F + e^- \quad (8.3)$$

$$SO_xF_y + zO \rightarrow SO_{x+z}F_{y-z} + zF \quad (8.4)$$

Processes like these have been studied previously and provide valuable context for the present results. Although rate constants for these reactions under the conditions studied here are not readily available, we can use some rate constant information from the literature to provide a measure of relative reaction efficiencies. For example, Plumb and Ryan[44] modeled the chemistry in SF_6/O_2 plasmas during Si etching at 1 Torr and find the rate constants for Reactions 8.1 and 8.2 to be fairly similar at 1.1×10^{-10} cm^3 s^{-1} and 7.9×10^{-11} cm^3 s^{-1}, respectively. In contrast, the rate constant for electron impact dissociation of SF_x species, Reaction 8.3, has been reported by Kline to be $\sim 3 \times 10^{-8}$ cm^3 s^{-1},[45] for 5 ≥

$x \geq 2$ in discharges at <300 mTorr. The reaction rate constant for Reaction 8.4 depends somewhat on the SO_xF_y species, but is similar to that for Reactions 8.1 and 8.2, according to Ryan and Plumb.[44]

At higher powers, electron impact processes like Reaction 8.3 become increasingly dominant, and SF_6 is broken down to yield SO_2.[46] This is evident in increases in F* signal, Figure 8.5b, and SO_2, Figure 8.8b. Some important changes take place, however, as O_2 is added to the discharge. Note that in our systems, we add oxygen, but keep the flow of SF_6 constant; thus the addition of oxygen causes the electron density in the discharge to decrease (as a result of increasing the overall electronegativity of the system),[46] inhibiting electron impact dissociation of SF_x species by Reaction 8.3. Simultaneously, the added presence of oxygen increases the likelihood of forming SO_xF_y species through processes like Reaction 8.4. The work of Tsai and Shao[47] on SF_6 abatement in industrial processes highlights this effect, suggesting that increased amounts of O_2 favor the formation of SO_2F_2 over SO_2. We see evidence for this effect in the presence of $SO_xF_y^+$ peaks in Figure 8.6, and indeed, the SO_2F_2 peak is the highest among this class of species when O_2 is added to the system. In Figure 8.5a, the plateau in F* signal with O_2 addition is consistent with a decrease in electron density, which could reduce the rate of Reaction 8.3.

The trends in Figure 8.8a provide additional support for this argument but require more careful consideration because of the observed change in coupling mode. At 100 W, the plateau in SO_2 LIF signal is a result of the mechanism described above, with lower electron density limiting the complete breakdown of SF_6 and, therefore, the formation of SO_2. At 200 W, the applied power is above the mode transition, Figure 8.8b, and we

therefore expect higher electron densities and enhancement of the rate of Reaction 8.3. It is also possible that the mode change alters the volume fraction of the glow discharge region, enhancing the significance of certain reactions and further affecting the plasma chemistry.[43] These changes are clearly significant enough to overcome the effects of oxygen addition; the SO_2 signal increases even up to the highest O_2 flow rate of 20 sccm, indicating continued breakdown of SF_6 in the discharge.

Dussart and coworkers describe a similar reaction scheme for the evolution of gas phase species in these discharge systems based on mass spectra and OES data.[7] In addition, they suggest that surface reactions of SO_2 may provide an additional source for the formation of SO_xF_y species in discharge mixtures of SF_6 and SO_2. Our interest in the possibility of such processes in SF_6/O_2 systems led us to investigate the surface reaction of SO_2 using the IRIS technique. The IRIS results in Table 8.2 suggest that SO_2 does not undergo surface reaction to a significant extent, and the SO_2 scatter coefficients do not change appreciably for a discharge of pure SO_2 or for a flow of neutral SO_2 gas. Thus, it seems clear that SO_2 does not contribute appreciably to the production of gas phase SO_xF_y species via surface reaction in these systems.

With a clearer understanding of how gas phase species are generated in SF_6/O_2 plasmas, it becomes possible to speculate on the origin of the F-incorporation observed with XPS in Figure 8.4, which appears to be correlated to Q_{O_2} in the plasma. One possibility is that small additions of O_2 (e.g., Q_{O_2}= 2.5 sccm) provide a sink for atomic S without appreciably lowering the electron density in the plasma. This prevents reformation of SF_x species and promotes liberation of atomic F, which can then get incorporated into the surface of the substrate being etched. Further addition of O_2

substantially decreases electron density in the system, thereby limiting breakdown of SF_x and concomitant production of F atoms. Hence, at Q_{O_2}> ~5 sccm, the amount of F on the surface plateaus, Figures 8.4 and 8.5a.

In addition to the information they reveal about generation of gas-phase SO_xF_y species, the near-unity surface scattering coefficients in Table 8.2 also suggest that SO_2 does not lead to surface incorporation of S, which is largely consistent with the trace levels of S measured by XPS. This is advantageous under most practical conditions, as S-incorporation is not desirable in the dry etching of Si substrates, where sulfur incorporation on Cu interconnects can be especially detrimental. However, it is worth mentioning that in certain applications, it may actually be desirable to incorporate sulfur on a surface, for example in the preparation of biosensitive semiconductor or polymer surfaces. Griesser and coworkers[48] have investigated the plasma processing of polymer materials in SO_2 discharges. They observed age-dependent changes in the amount of sulfur on the surfaces of these materials due to reptation of the polar SO_x groups away from the polymer-air interface towards the material bulk. Sulfur incorporation might also be desired for the passivation of organic materials in multilayer etch resist constructs.[8,9] Future studies of the interaction of SO_2 with these and other materials may provide valuable information about the controlled implantation of sulfur-containing functional groups and the retention of these functional groups over time for use in a variety of applications.

8.4 Summary

This work explored the mechanisms for SF_6/O_2 plasma etching of Si and SiO_2 substrates using gas-phase diagnostics, surface analysis, and measurement of SO_2 surface interactions. In general, etch selectivity was comparable to that obtained in NF_3/O_2 plasmas and significantly higher than in fluorocarbon/O_2 plasmas. Gas phase data suggest that SO_2 is a sink for sulfur atoms such that it promotes the liberation of F atoms in the plasma, and thereby affects the etch behavior of the system. IRIS results for SO_2 clearly show that SO_2 does not react appreciably on the substrate surfaces under any conditions, leading to the conclusion that SO_2 is not likely to contribute to the production of gas phase SO_xF_y species via surface reaction in these systems. Notably, although significant incorporation of F is observed on Si, we do not see any strong evidence for formation of an SiO_xF_y passivation layer on our surfaces during etch processing. These studies may facilitate the refinement of etch models for SF_6/O_2 plasma processing.

8.5 References

[1]M. Shih, W. J. Lee, C. H. Tsai, P. J. Tsai, and C. Y. Chen, J. Air Waste Manage. Assoc. **52,** 1274 (2002).
[2]R. Kurte, C. Beyer, H. M. Heise, and D. Klockow, Anal. Bioanal. Chem. **373,** 639 (2002).
[3]C. H. Tsai and J. M. Shao, J. Hazard. Mater. **157,** 201 (2008).
[4]M. J. de Boer, G. E. Gardeniers, H. V. Jansen, E. Smulders, M.-J. Gilde, G. Roelofs, J. N. Sasserath, and M. Elwenspoek, J. MEMS **11,** 385 (2002).
[5]S. Tachi, K. Tsujimoto, and S. Okudaira, Appl. Phys. Lett. **52,** 616 (1988).
[6]R. d'Aggostino and D. L. Flamm, J. Appl. Phys. **52,** 162 (1981).
[7]C. Y. Duluard, R. Dussart, T. Tillocher, L. E. Pichon, P. Lefaucheux, M. Puech, and P. Ranson, Plasma Sources Sci. Technol. **17,** 045008 (2008).
[8]M. Pons, J. Pelletier, and O. Joubert, J. Appl. Phys. **75,** 4709 (1994).
[9]A. M. Goethals, F. Van Roey, T. Sugihara, and L. Van den hove, J. Vac. Sci. Technol., B **16,** 3322 (1998).
[10]C. Monget and O. Joubert, J. Vac. Sci. Technol., B **17,** 1406 (1999).
[11]A. P. Mahorowala, K. Babich, Q. Lin, D. R. Medeiros, K. Petrillo, J. Simons, M. Angelopoulos, R. Sooriyakumaran, D. Hofer, G. W. Reynolds, and J. W. Taylor, J. Vac. Sci. Technol., A **18,** 1411 (2000).
[12]P. Bhatnagar, S. Pnada, N. L. Edelman, S. D. Allen, R. Wise, and A. Mahorowala, Appl. Phys. Lett. **88,** 231501 (2006).
[13]D. E. Ibbotson, J. A. Mucha, D. L. Flamm, and J. M. Cook, Appl. Phys. Lett. **46,** 794 (1985).
[14]K. P. Lee, K. B. Jung, R. K. Singh, S. J. Pearton, C. Hobbs, and P. Tobin, J. Vac. Sci. Technol., A **18,** 1169 (2000).
[15]K. Takahashi, K. Ono, and Y. Setsuhara, J. Vac. Sci. Technol., A **23,** 1691 (2005).
[16]J. C. Martz, D. W. Hess, and W. E. Anderson, J. Appl. Phys. **67,** 3609 (1990).
[17]K. S. Min, B. J. Park, S. W. Kim, S. K. Kang, G. Y. Yeom, S. H. Heo, H. S. Hwang, and C. Y. Kang, J. Kor. Phys. Soc. **53,** 1675 (2008).
[18]R. Venkatasubramanian, M. L. Timmons, and T. S. Colpitts, Appl. Phys. Lett. **59,** 2153 (1991).
[19]G. Monier, L. Bideux, O. Desplats, C. Fontaine, C. Rober-Goumet, and B. Gruzza, Appl. Surf. Sci. **256,** 56 (2009).
[20]D. Gao, M. B. J. Wijesundara, C. Carraro, R. T. Howe, and R. Maboudian, J. Vac. Sci. Technol., B **22,** 513 (2004).
[21]M. S. So, S.-G. Lim, and T. N. Jackson, J. Vac. Sci. Technol., B **17,** 2055 (1999).
[22]H. Jansen, M. de Boer, R. Legtenberg, and M. Elwenspoek, J. Micromech. Microeng. **5,** 115 (1995).
[23]S. G. Lias, J. E. Bartmess, J. F. Liebman, J. L. Holmes, R. D. Levin, and W. G. Mallard, J. Phys. Chem. Ref. Data **17,** 1 (1988).
[24]D. J. Grant, M. H. Matus, J. R. Switzer, and D. A. Dixon, J. Phys. Chem. A **112,** 3145 (2008).
[25]J. M. Ajello, G. K. James, I. Kanik, and B. O. Franklin, J.Geophys. Res.-Space Physics **97,** 10473 (1992).
[26]L. E. Brus and J. R. McDonald, J. Chem. Phys. **61,** 97 (1974).

[27]A. Dastageer, E. Hegazi, A. Hamdan, and F. AlAdel, Chem. Phys. Lett. **275,** 283 (1997).
[28]H. Watanabe, S. Tsuchiya, and S. Koda, Farad. Disc. **75,** 365 (1983).
[29]R. Kullmer and W. Demtroder, J. Chem. Phys. **84,** 3672 (1986).
[30]H. Watanabe, Y. Hyodo, S. Tsuchiya, and S. Koda, J. Phys. Chem. **86,** 685 (1982).
[31]P. R. McCurdy, J. M. Truitt, and E. R. Fisher, J. Vac. Sci. Technol. A **17,** 2475 (1999).
[32]K. N. Ostrikov, S. Xu, and M. Y. Yu, J. Appl. Phys. **88,** 2268 (2000).
[33]U. Kortshagen, N. D. Gibson, and J. E. Lawler, J. Phys. D: Appl. Phys. **29,** 1224 (1996).
[34]C. I. Butoi, M. L. Steen, J. R. D. Peers, and E. R. Fisher, J. Phys. Chem. B **105,** 5957 (2001).
[35]P. R. McCurdy, K. H. A. Bogart, N. F. Dalleska, and E. R. Fisher, Rev. Sci. Instrum. **68,** 1684 (1997).
[36]P. R. McCurdy, C. I. Butoi, K. L. Williams, and E. R. Fisher, J. Phys. Chem. B **103,** 6919 (1999).
[37]K. L. Williams and E. R. Fisher, J. Vac. Sci. Technol. A **21,** 1024 (2003).
[38]A. J. Lennon, A. W. Y. Ho-Baillie, and S. R. Wenham, Solar Energy Mater. Solar Cells **93,** 1865 (2009).
[39]G. S. Oehrlein, Y. Zhang, D. Vender, and M. Haverlag, J. Vac. Sci. Technol., A **12,** 323 (1994).
[40]S. Gomez, R. J. Belen, M. Kiehlbauch, and E. S. Aydil, Journal of Vacuum Science and Technology A **22,** 606 (2004).
[41]R. Dussart, X. Mellhaoui, T. Tillocher, P. Lefaucheux, M. Boufnichel, and P. Ranson, Microelectron. Eng. **84,** 1128 (2007).
[42]X. Mellhaoui, R. Dussart, T. Tillocher, P. Lefaucheux, P. Ranson, M. Boufnichel, and L. J. Overzet, J. Appl. Phys. **98,** 104901 (2005).
[43]R. J. Van Brunt and J. T. Herron, Phys. Scr. **T53,** 9 (1994).
[44]K. R. Ryan and I. C. Plumb, Plasma Chem. Plasma Process. **10,** 207 (1990).
[45]L. E. Kline, IEEE Trans. Plasma Sci. **14,** 145 (1986).
[46]M. Shih, W.-J. Lee, C.-H. Tasai, P.-J. Tsai, and C.-Y. Chen, J. Air Waste Manage. Assoc. **52,** 1274 (2002).
[47]C.-H. Tsai and J.-M. Shao, J. Hazard. Mater. **157,** 201 (2008).
[48]K. S. Siow, L. Britcher, S. Kumar, and H. J. Griesser, Plasma Process. Polym. **6,** 583 (2009).

CHAPTER 9

RESEARCH SUMMARY AND PERSPECTIVES

This chapter describes research progress in the areas of a-CN_x PECVD and Si etching in SF_6/O_2 plasmas. The utility of completed studies in learning about the molecular level chemistry of these systems is emphasized, as are the broader implications of the research results. Also included is a consideration of additional areas of study that may be of value as this research moves forward.

9.1 Research Summary

Plasma processing remains a proven technology both for the deposition of novel materials and for dry etching. New applications and advances in process control continue to expand the frontiers of the technology, and in a general sense, the research in this dissertation seeks the continued expansion of these frontiers through the clarification of molecular level chemistry in two specific sets of discharge systems. The first set of discharge systems emphasizes the use of single source precursors for the deposition of a-CN_x materials and was chosen to provide insight into the fundamental chemistry taking place during deposition. The second set of discharges uses feed gas mixtures of SF_6 and O_2 to explore the origins of chemical selectivity during Si etching. Both systems offer potential for advancing their respective applications, and the value of work completed to date is illustrated below on the basis of several research highlights.

Characterization of gas phase species in CH_3CN plasmas indicates that CN radicals serve as reservoirs of N in the gas phase, and compositional analysis of films from the same systems reveal significant amounts of nitrogen content. The convergence of these results points to CN as a likely source of N-content in PECVD a-CN_x. Moreover, IRIS measurements reveal high CN surface reactivity coefficients (R(CN)) of ~ 94%, providing a direct link between gas phase and film studies and strongly supporting the idea that CN radicals are incorporated into a-CN_x films. These results have important implications in the CVD synthesis of a-CN_x as widely different conclusions have been reported in the literature regarding the fate of CN during deposition.[1-3]

The IRIS measurements discussed above place CN securely among the more reactive species studied in our lab.[4] From the perspective of a chemist, it is also important to obtain a more complete understanding of how these high reactivities come about. Laser-induced fluorescence measurements were used to characterize the gas phase properties of CN in greater detail, and the results indicate that a substantial amount of energy is contained within the molecules' internal degrees of freedom.

Additional – and very important – insight comes from the work of Michelsen et al., who reported state-specific measurements of D_2 reactions on single-crystal Cu.[5] These studies conclusively link the internal energies of gas phase diatomic species to their surface reactivities; by extension, it is evident that the high internal energies of CN in a-CN_x deposition systems are largely responsible for their incorporation at the film surface. This information helps to bridge the gap in our understanding of CN surface interactions during PECVD, and in doing so, facilitates the comparison of PECVD to alternative methods for a-CN_x deposition, such as laser ablation,[1] in which CN energetics are suggested to affect film formation. Moreover, we find that the correlation between energetics and reactivity holds for a number of plasma species studied in our lab; this may have far-reaching repercussions for a number of CVD, etch, and surface functionalization technologies as it suggests a non-specific model for predicting the surface behavior of activated gas phase species. This is discussed further below.

Deposition studies were extended to BrCN discharges as well, yielding films that delaminate upon exposure to atmosphere when the film thicknesses is greater than ~500 nm. These observations parallel studies on sputter-coated a-CN_x films, which suggest that H_2O vapor diffuses through voids in the film and reacts at the film-substrate

interface.[6,7] In light of these data, our investigation of a-CN_x deposition in BrCN-containing discharges focused on the origin of the films' porosity as a component of the delamination behavior. One hypothesis was that addition of hydrocarbons to BrCN discharges might promote cross-linking and densification of the films, drawing on studies of the deposition of diamond-like carbon (DLC)[8] and carbon-containing boron nitride (BN:C).[9] However, the addition of hydrocarbons (in the form of CH_4) to BrCN did not prevent film delamination, and attentions were turned to a second hypothesis, which focused on the role of Br. A simple model of the breakdown chemistry was developed to allow variation of the effective Br-content in the discharge, and the results show that even small amounts of Br have an effect on the growth rate and optical properties of the films. Moreover, preliminary observations suggest that film delamination does not occur with intermediate levels of Br-content; this result was discussed in the context of the electronegativity of Br, which may affect ion bombardment conditions during deposition.

The observation of delamination in these systems points to the unique contribution of CN radicals during deposition and once again establishes commonalities between PECVD and an alternative method (in this case sputter deposition) for depositing a-CN_x. Furthermore, preliminary results suggest that continued exploration of these systems will yield valuable chemical information about film adhesion as an application-relevant property of these materials.

This dissertation also presents work on SF_6/O_2 discharges that illustrate the utility of studying plasma-surface interactions during Si etch processes. Free F is expected to be the primary etching species in these systems, and work done by others suggests that O promotes the formation of an etch-resistant SiO_xF_y passivation layer during processing.[10]

The presence of SO_2 is acknowledged as well, and our studies place emphasis on understanding the role of SO_2 during processing. IRIS measurements suggest that SO_2 does not promote surface production of SO_xF_y species, as has been suggested;[11] rather it appears to act as a sink for atomic S and supports the liberation of F. These results represent a modest, though not insignificant, contribution to the field of etch chemistry as they facilitate further refinement of models for etching of Si, which continues to play an important role in semiconductor fabrication processes.

9.2 Future Work

As this research progresses, a number of aspects of a-CN_x PECVD chemistry appear to warrant further investigation. For example, deposition studies in CH_3CN discharges highlight the dependence of the growth rate on the initial and steady-state substrate temperatures and suggest that early a-CN_x film growth is characterized by an induction or nucleation period. Further studies on the evolution of film thickness under different substrate heating conditions should shed additional light on these effects.

As mentioned above, our correlation of IRIS data and radical energetics in a variety of discharge systems allude to the potential for developing a general model for predicting radical-surface interactions. Given the similarly high surface reaction probabilities observed for CN, CH, and SiH, a detailed comparison of the formation mechanisms and energetics of these molecules may provide a better grasp of factors that promote surface reaction. These principles can then be extended to explain the behavior of less reactive radical species, such as NH and OH.

There is also much room for the expansion of studies on BrCN-containing discharges. Preliminary results indicate that investigation of the role of Br-content may be one promising avenue for understanding the effects of plasma chemistry on film adhesion, but additional studies are needed to correlate the films' composition and microstructure to their delamination behavior. In addition, characterization of electrostatic properties of these plasma discharges, perhaps using Langmuir probe studies, would be of great value, as very few reports exist on the effect of electronegative species, such as Br, on sheath properties, plasma potential, and ion bombardment in PECVD systems. Lastly, SFG spectroscopy was suggested as a possible means of probing chemical processes at the film-substrate interface during film delamination.

9.3 References

[1]A. A. Voevodin, J. G. Jones, J. S. Zabinski, Z. Czigany, and L. Hultman, J. Appl. Phys. **92,** 4980 (2002).

[2]S. Veprek, J. Weidmann, and F. Glatz, J. Vac. Sci. Technol., A **13,** 2914 (1995).

[3]M. Zhang, Y. Nakayama, T. Miyazaki, and M. Kume, J. Appl. Phys. **85,** 2904 (1999).

[4]J. M. Stillahn, K. J. Trevino, and E. R. Fisher, Annu. Rev. Anal. Chem. **1,** 261 (2008).

[5]H. A. Michelsen, C. T. Rettner, and D. J. Auerbach, J. Chem. Phys. **98,** 8294 (1993).

[6]J. Moller, D. Reiche, M. Bobeth, and W. Pompe, Surf. Coat. Technol. **150,** 8 (2002).

[7]S. Peponas, M. Benlahsen, and M. Guedda, J. Appl. Phys. **106,** 013525 (2009).

[8]A. von Keudell, T. Schwarz-Selinger, and W. Jacob, J. Appl. Phys. **89,** 2979 (2001).

[9]K.-B. Kim and S.-H. Kim, J. Vac. Sci. Technol., A **18,** 900 (2000).

[10]R. Dussart, X. Mellhaoui, T. Tillocher, P. Lefaucheux, M. Boufnichel, and P. Ranson, Microelectron. Eng. **84,** 1128 (2007).

[11]C. Y. Duluard, R. Dussart, T. Tillocher, L. E. Pichon, P. Lefaucheux, M. Puech, and P. Ranson, Plasma Sources Sci. Technol. **17,** 045008 (2008).

APPENDIX A: Modeling and Analysis of Spectroscopic Ellipsometry Data

Determination of a-CN_x film thickness from VASE data was performed by optimizing the fit between the experimental and simulated ellipsometric data. The general model used to describe the film cross-section is made up of four regions. The region is a 1 mm thick layer of Si with optical constants corresponding to those reported by Jellison. Above this, a semiconducting layer was included to model the thin layers of disordered Si that may exist on the surface of a Si substrate; the thickness of this layer varied from 0-15 nm. The third region of the general model corresponds to the deposited a-CN_x film and was modeled with one or more Cauchy layers. The Cauchy dispersion model, which is commonly used to model ellipsometric data for amorphous materials, parameterizes the wavelength dependence of the refractive index, n:

$$n(\lambda) = A + \frac{B}{\lambda^2} + \frac{C}{\lambda^4} \qquad \text{(A.1)}$$

Where, A, B, and C are constants. In some cases, multiple Cauchy layers were included in the model to optimize the fit. In addition, the thickness of the individual layers describing the a-CN_x films varied depending on growth rate and deposition time. The final component of the general model describes the roughness of the film sample and consists of an effective medium approximation (EMA) layer consisting of a 50/50 mixture of the underlying Cauchy layer and voids (air).

Our optical transmission and absorption data indicate that the a-CN_x films generally exhibit a strong absorption at $\lambda < 450$ nm. At these wavelengths, the reliability of the Cauchy model is limited; thus, the ellipsometric data were initially fit over the range of wavelengths where the material is highly transparent. Using these data, the optical constants for n and k were then fit in a point-by-point manner over the remaining

wavelengths to encompass all of the experimental data. The above process consistently produced reasonably good fits with mean standard errors (*MSE*) ≤ 10.

The optical band gaps, E_g, of the a-CN_x films were determined through additional analysis of the ellipsometric data. Using the data analysis software, the Cauchy layer describing the a-CN_x film was used as a reference material in a Tauc-Lorentz oscillator layer. The Tauc-Lorentz model describes a material as a collection of absorption peaks, or oscillators, and is better-suited for extracting information from ellipsometric data over wavelengths where the material absorbs. The generated Tauc-Lorentz data were fit to the experimental data, and *k* values were used to obtain optical absorption coefficients, α, at each wavelength according to the dispersion relation of *k*:

$$\alpha = \frac{4\pi k}{\lambda} \quad \text{(A.2)}$$

The Tauc band gap, E_{Tauc}, is then determined from the Tauc relation:

$$E\alpha(E) = A(E - E_{Tauc}) \quad \text{(A.3)}$$

E_{Tauc} is found by extrapolating the linear portion of a plot of $\sqrt{\alpha E}$ as a function of E to find the x-intercept. In cases where the Tauc plot did not exhibit a clear region of linearity, the slope was determined from a linear fit to several points near where $\sqrt{\alpha E}$ starts to increase. The reproducibility of this method for quantifying E_{Tauc} is reflected in the relatively small standard deviations in Table 7.1.

APPENDIX B. Correction of IRIS Data for Rotational Temperature Effects

Correction of the reactivity coefficients given by the numerical simulation is based on the comparison of the density of a molecule of interest in the molecular beam, $N_{evJ,B}$, and after scattering from a substrate, $N_{evJ,S}$, where N_{evJ} is the population corresponding to a particular electronic, vibrational, and rotational configuration. This population is given by:

$$N_{evJ} = N_{ev} \frac{(2J+1)exp\{-BJ(J+1)/k_B T\}}{Z_{rot}} \qquad \text{(B.1)}$$

J is the rotational quantum number, B is the rotational constant, k_B is Boltzmann constant, T is the temperature of the molecules, and Z_{rot} is the rotational partition function. Comparison of the population of scattered molecules in this configuration to those with the same configuration in the molecular beam gives the observed scatter coefficient:

$$S_{obs} = \frac{N_{evJ,S}}{N_{evJ,B}} = \frac{N_{ev,S}}{N_{ev,B}} \cdot \frac{(2J+1)exp\{-BJ(J+1)/k_B T_S\}}{(2J+1)exp\{-BJ(J+1)/k_B T_B\}} \cdot \frac{Z_{rot,B}}{Z_{rot,S}}$$

$$= \frac{N_{ev,S}}{N_{ev,B}} \cdot exp\left\{\frac{-BJ(J+1)}{k_B}\left(\frac{1}{T_S} - \frac{1}{T_B}\right)\right\} \cdot \frac{Z_{rot,B}}{Z_{rot,S}} \qquad \text{(B.2)}$$

The previous version of the model used for correcting the observed scatter coefficients for the effects of rotational temperature assumed that $Z_{rot,B} = Z_{rot,S}$ so that this term was removed from the above equation. However, the rotational partition function, which serves to normalize the population distribution, is temperature-dependent:

$$Z_{rot} = \sum_J (2J+1) exp\left\{\frac{-hcB}{k_B T} J(J+1)\right\} \qquad \text{(B.3)}$$

Here, c is the speed of light and h is the Planck constant. Because the molecules' temperature is often different in the incident and scattered beams (due to thermal equilibration of incident molecules with the substrate), the quotient of the two partition functions does not reduce to 1. However, under conditions where many of a molecule's rotational levels are populated (as for small rotational constants or at high temperatures), the rotational partition function can be approximated as:

$$Z_{rot} \approx \frac{k_B T}{hcB} \tag{B.4}$$

The quotient of the two partition functions thus simplifies as T_B/T_S. If one assumes $S = 1$ (i.e., $N_{ev,S} = N_{ev,B}$), then the necessary correction for the rotational temperature effect is given by:

$$correction = \; exp\left\{\frac{-BJ(J+1)}{k_B}\left(\frac{1}{T_S} - \frac{1}{T_B}\right)\right\} \cdot \frac{T_B}{T_S} \tag{B.5}$$

The actual scatter coefficient, S_{act}, is therefore $S_{act} = S_{obs}/[correction]$.